University Of Oxford

Mathematical, Physical and Life Science Division,
Department Of Physics,
Atomic And Laser Physics

2015

D.Phil. Thesis

Opacity and Saturable Absorption in Solid-Density Plasmas Generated by an X-Ray Free-Electron-Laser

David S. Rackstraw

Supervisor: Prof. J.S. Wark

Opacity and Saturable Absorption in Solid-Density Plasmas Generated by an X-Ray Free-Electron-Laser

David Rackstraw
Mansfield College

Thesis submitted for the Degree of Doctor of Philosophy
Trinity Term 2015

Abstract

The arrival of 4th generation light-sources has opened up new regimes in x-ray–matter interactions. A billion times spectrally brighter than the preceding x-ray sources, free-electron-lasers (FELs) can deposit large amounts of energy into a system in less than 100 fs. Since the absorption of x-rays is reasonably well understood and the pulse length is so short, the plasma conditions created are well characterized. The work presented in this thesis relates to a series of experiments where solid aluminium foils were heated with the focussed FEL radiation. The way that the opacity of the FEL heated foil would affect the observed emission spectrum is investigated. The extent to which the opacity influences the emission spectra is found to have intensity and photon energy dependencies. The transmission of the x-ray pulse used to generate a solid-density aluminium plasma is studied in both simulation work using the collisional-radiative code SCFLY and experiment. The phenomenon of saturable absorption is seen to occur, caused by the system being ionized to such an extent that none of the ions present can absorb the x-ray photons through K-shell photoionization. The use of the FEL beam in a split and delay scheme was also explored. Simulations of the time dependent changes in transmission and what may be observed were performed.

Acknowledgements

There are three people I would like to thank for their great help in getting this work to where it is now. Firstly, I would like to thank my supervisor Justin Wark. He has helped to me to greatly improve the standards of both my written and presentation work, in addition to giving me opportunities to work at truly world leading facilities. Next I would like to thank Sam Vinko and Orlando Ciricosta for frequent discussions on the work over coffee and lunch as well as putting up with my simplistic questions. For their contributions in this work I would like to thank the other authors of publications [1] and [2]. Finally I would like to thank all the colleagues, housemates, friends and family who have helped and supported me over the past few years.

The author is grateful to the EPSRC for support under grant number EP/H035877/1. Portions of this research were carried out on the SXR Instrument at the Linac Coherent Light Source (LCLS), a division of SLAC National Accelerator Laboratory and an Office of Science user facility operated by Stanford University for the U.S. Department of Energy. The SXR Instrument is funded by a consortium whose membership includes the LCLS, Stanford University through the Stanford Institute for Materials Energy Sciences (SIMES), Lawrence Berkeley National Laboratory (LBNL), University of Hamburg through the BMBF priority program FSP 301, and the Center for Free Electron Laser Science (CFEL).

Contents

CHAPTER 1

Introduction

This thesis represents the work performed by the author on the interactions between solid-density plasmas and the high intensity x-ray pulses from free-electron-lasers that were used to generate them. This introductory chapter contains a brief description of how these high intensity x-ray pulses are generated in free-electron-lasers along with a description of some of the first experiments performed at such facilities. The structure of the remainder of the thesis is also outlined along with the contributions by the author to the work presented within this thesis.

1.1 X-ray Free-Electron-Lasers

X-ray Free-Electron-Lasers (X-ray FELs) have given rise to a spectacular increase in peak spectral brightness of x-ray sources by over 9 orders of

magnitude [3]. Such high brightnesses have opened up new regimes in x-ray–matter interactions. The generation of such intense radiation is built upon the technology used in synchrotron light-sources around the world. When an electron accelerates it will radiate energy in the form of electromagnetic radiation.

X-rays can be generated by passing an electron beam through an undulator, which is a periodic structure of dipole magnets. The oscillatory motion of the electron in the magnetic field generates synchrotron radiation in a directional cone.

The radiation generated in an undulator has a wavelength of

$$\lambda = \frac{\left(1 + K^2/2\right)}{2\gamma^2}\lambda_u \tag{1.1}$$

where K is the undulator parameter, γ is the electron energy in units of rest mass ($\gamma = \left(1 - \frac{v^2}{c^2}\right)^{-1/2}$) and λ_u is the undulator period. The undulator parameter is defined as $K = 0.934\lambda_u[\text{cm}]B_0[\text{T}]$ where B_0 is the peak magnetic field. The undulator parameter is a measure of how much the electron beam is deflected in the transverse direction as it passes over the undulator. The photon energy is dependent on the gamma factor squared, this is due to the undulator period seen by the electron bunch being length contracted (by a factor gamma) and when the radiation generated by the electron is transformed to the laboratory frame it is Doppler shifted by a second gamma factor. Since the photon energy of the radiation produced is dependent on the energy of the electron bunch it is possible to tune the radiation to an arbitrary photon energy by changing the electron energy.

In ordinary synchrotron sources each electron will emit independently and with a different phase leading to incoherent radiation. The key to free-

electron-laser operation is that the x-ray light generated can interact with the electron bunch. In the presence of the undulator field the (highly energetic) electron bunch will oscillate in the transverse direction. The radiation produced by the electron bunch is such that the magnetic field of the synchrotron radiation is perpendicular to the electron transverse motion. Due to the $\mathbf{v} \times \mathbf{B}$ term of the Lorentz force, the interaction between the transverse motion of the electron and the magnetic field of the currently present radiation will lead to a longitudinal force on the electron, which leads to microbunching of the electrons separated by the wavelength of the radiation. The microbunching leads to the electrons emitting synchrotron radiation in phase with the current radiation which in turn leads to greater microbunching and the generation of a high intensity coherent light pulse. Over this region the intensity of the radiation will increase exponentially.

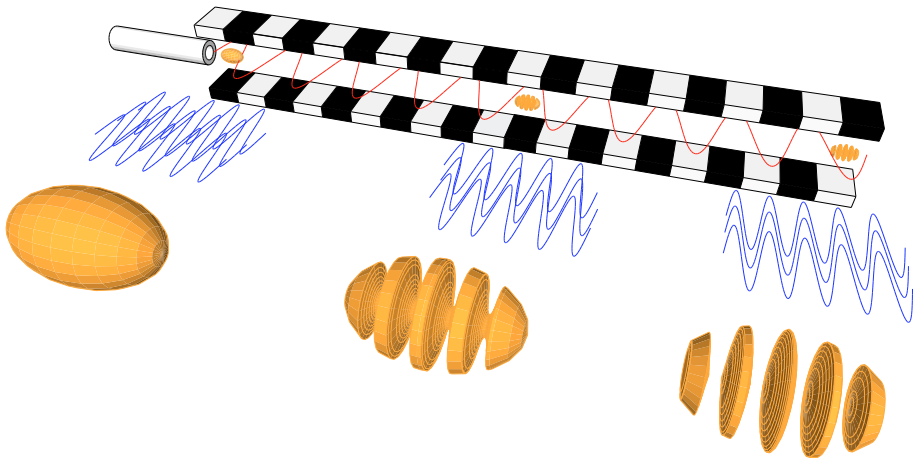

Figure 1.1: Schematic of the FEL process. As the electron bunch progresses through the undulator it forms microbunches, which generate coherent radiation.

Obviously since the energy for the radiation comes from the electron bunch the exponential increase can't continue indefinitely. In fact saturation

of the radiation will occur at an earlier stage. The electron bunch does not quite travel at the speed of light and so will slip in position relative to the light pulse. After a certain amount of phase difference the electron bunch will no longer give energy to the radiation, but in fact start taking energy from the radiation pulse. Saturation of the FEL pulse will occur after around twenty gain lengths [4], a number which was experimentally realised at LCLS [5], with typically around 10^{12} photons in a single pulse.

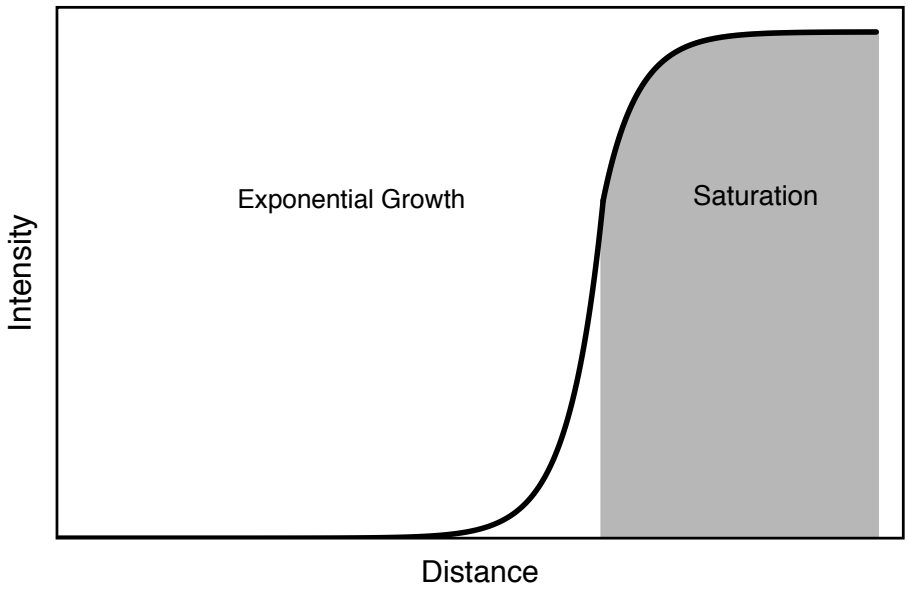

Figure 1.2: Initially the intensity of the radiation in an FEL will increase exponentially, at greater distances the radiation will saturate.

FELs are designed such that the amplification up to saturation occurs over a single pass of the undulator. There has been much success recently in using the self-amplified spontaneous emission (SASE) method of operation [6, 7]. This process relies on random shot noise to generate the initial spontaneous emission which is amplified through its interaction with the electron bunch up to saturation. This produces a pulse that has a spiky profile both temporally and spectrally. An individual temporal spike has

a sub-femtosecond duration. In this unseeded mode the radiation has a bandwidth of 0.2–1.0% [5]. Seeding of the radiation, either through use of a separate source (more common in the XUV regime where high-harmonic sources can produce relevant radiation), or through monochromating the initial radiation produced in the first stage of the FEL before amplifying this (so-called self-seeding which is currently a possibility at the LCLS [8]) can be used to reduce the bandwidth of the emergent FEL radiation. At LCLS using the self-seeded mode the bandwidth is reduced by a factor of 40–50 when compared with the normal SASE radiation. However, the operation of the self-seeded mode at LCLS leads to a dramatic reduction in the number of photons when compared to the SASE operation, and so in the work described later in this thesis, where the concern is primarily with having large numbers of photons rather than very narrow bandwidth, the FEL is used in the SASE mode of operation.

Practical realisation of XFELs has only occurred recently with a handful of facilities currently operating. The Free-electron-LASer in Hamburg (FLASH) [9], located in Germany, was the first such device to produce radiation in the extreme ultraviolet (XUV) range (with photon energies in the fundamental ranging between 26 and 180 eV [10]). The Linac Coherent Light Source (LCLS) [5] based in Stanford, USA was the first to produce hard x-ray radiation with the photon energy available at the experimental endstations varying between 280 eV and 10 keV (although specific endstations have their own allowable range within this, due to the optics used in beam transport). Further facilities in Trieste, Italy (FERMI) [11] and Kouto, Japan (SACLA) [12], in the XUV and hard x-ray regimes respectively, have also come online in recent years. More facilities are currently under construction including the European XFEL in Hamburg [13] and SwissFEL in

Villigen [14].

Figure 1.3 is an aerial view of LCLS, where the final kilometre of the old LINAC has been converted to be the electron source for an FEL. As a measure of scale the road that crosses over LCLS is the I-280 (an eight lane highway). It uses an undulator which is 132m long, sufficient for the light produced to be in the saturated gain regime.

Figure 1.3: Aerial view of LCLS in Stanford, USA

1.2 High intensity x-ray–matter interactions: First experiments

The short pulse duration and high intensity pulses afforded by XFELs have opened up new regimes in x-ray–matter interaction. The short pulse duration, typically tens of femtoseconds though potentially down to sub femtosecond, allow for the study of matter on timescales shorter than that of atomic motion. Whilst much work has been performed using XUV sources, the work in this thesis is primarily concerned with the processes that occur with the x-ray photon energies accessible with LCLS. As such some of the first experiments performed at LCLS are outlined in this section. One of the first experiments performed at LCLS concerned the interaction between the laser and isolated neon atoms [15].

X-ray photons will typically interact with electrons deep in the atom. The primary interaction is through photoionization, where an electron absorbs a photon with sufficient energy for it to escape the atom. The electrons that are ejected are preferentially those that are most bound to the atom, but with the energy required to ionize them less than the energy of the photon. The inner-most shell of electron orbits is denoted the K-shell, with those shells further out named alphabetically from there (i.e. the next shell is the L-shell). The minimum photon energy to ionize an electron from the K-shell is known as the K-edge energy.

In the experiment of Young *et al.* [15] the intensities of the x-ray radiation were such that many photons could be absorbed by a single atom over the duration of the x-ray pulse. It was found that when the FEL was tuned significantly above the K-edge energy of Neon (870 eV) the absorption process lead predominantly, at least for the lower charge states, to ions of even charge state being produced. Initially the absorption of the x-ray photon was accompanied by the ejection of an electron from the K-shell. The resulting K-shell hole was filled by Auger decay, with an electron from the L-shell falling into the K-shell and another electron in the L-shell being ejected, leaving two holes in the L-shell. With the possibility of absorbing multiple photons in a single pulse, and each photon, typically, leading to the ejection of two electrons, ions with even charge states dominate. When the FEL was tuned below the neutral K-edge energy copious ions with both even and odd charge states were produced, due to the dominant absorption process being L-shell photoionization and so L-shell electrons are sequentially stripped from the atom.

The results of the experiment were in good agreement with both the atomic-kinetics simulations performed by Young and co-workers [15] and

also subsequently the work by Ciricosta *et al.* using the SCFLY collisional radiative code [16]. The high intensities lend themselves to studying non-linear phenomena in the x-ray regime [17].

In the experiment by Rudek *et al.* [18] the ionization of Xenon atoms by the FEL was studied. Whilst their results for the charge state distribution of atoms pumped with a photon energy of 2.0 keV agreed well with their simulations, the results of pumping at a photon energy of 1.5 keV did not. Their simulations used a simple model where they only considered direct photoionization. This was sufficient to reproduce the maximium charge state achieved in the 2.0 keV case and reproduced the overall charge state distribution well. In the case of exciting with 1.5 keV photons this model would only allow ionization up to a maximum charge state of 26+. However, in the experiment charge states up to 36+ were observed. By looking at the energy of transitions between bound levels it was found that the 1.5 keV photons could be used to excite resonant transitions. This in turn would lead to a state with core holes leading to further ionization through Auger decay. This work highlighted the importance of including transitions between bound levels in calculating the system evolution.

Further experiments were performed studying the interaction of the FEL with molecules [19, 20, 21] and clusters [22, 23, 24]. The charge states observed in the cluster experiments were seen to depend on the size of the cluster, with the delocalization of the electrons in the x-ray induced nanoplasma in larger clusters increasing the Auger lifetime, reducing the efficiency of absorption of the x-ray pulses [22].

Following on from the effects of x-ray radiation on isolated atoms and molecules additional effects, such as collisional and opacity effects, will have increasing influence on the system as the density and size of samples is

increased. A logical regime to examine is that of solid-density samples, since these can be readily produced and are well characterised.

The realisation of isochoric heating, where the density of the system remains constant while the temperature is increased, has long been a goal in plasma physics. By having well defined density the properties of such matter can be examined and used to not only benchmark computer codes but is also of immense physical interest. Such plasmas are found in astrophysical objects, like stars [25], and have relevance in inertial confinement fusion research [26].

One of the purported means of isochorically heating is through the use of short pulse optical lasers [27, 28, 29]. If a solid density sample is heated it will naturally want to expand due to hydrodynamic motion, the timescale of which is on the order of picoseconds. So in order to isochorically heat the energy would have to be deposited within this timescale. Short pulse optical layers will deposit their energy in the skin depth of the sample, on the order of a few nanometres. Hence the laser will only directly heat the surface of the target. This will generate hot electrons which travel through the sample to a depth according to their mean free path. This means there are potentially large gradients in the temperature of the sample and so the conditions of the regions which are emitting are not well defined.

By reducing the thickness of the sample the difference between the front and the back will be reduced. In the initial interaction between the laser and the surface of the sample the front surface will rapidly expand reducing the density. To reduce this effect samples of the material under inspection are buried in other materials. In the case of aluminium samples materials such as carbon [28] and magnesium oxide [27] are used. The use of these additional layer restricts the expansion of the material under study and

mean that a thin foil can be used giving comparatively uniform conditions for the emitting region.

The plasmas generated in these methods are often analysed through examination of the K-shell emission. The emission will take place over a number of picoseconds [30] and spatial variations in the temperature can be quite large [31]. Since the method of energy deposition is not well understood, the emission spectra are the key diagnostic in determining the temperature of the system. However, these are reliant on computer codes to predict the emission from a sample of a given temperature and density.

In contrast, the absorption mechanism in x-ray FELs is well understood and predictable, leading to well characterized plasmas. Also, since the source of K-shell emission in the FEL case is that x-ray photons knocking out core electrons, rather than collisions from a thermal bath of hot electrons the emission from the plasma in the FEL case is limited temporally to the time of the FEL pulse and by the K-shell hole lifetime. This gives a characteristic timescale of femtoseconds, so there is no possibility of the emission being altered due to hydrodynamic expansion. Also since x-rays have a frequency much higher than the plasma frequency of the cold metal the photons are able to penetrate directly into the sample.

The Oxford group has been at the forefront of investigating these interactions in the solid-density regime. In the work of Vinko *et al.* [32] solid-density aluminium foil samples were exposed to the LCLS x-ray beam. As the photon energy of the FEL was increased emission from more charge states was observed. The emission spectrum of the aluminium sample when pumped at different FEL photon energies is shown in figure 1.4. In contrast to the isolated Neon atoms, where even charge states were more prevalent, the emission from the aluminium sample did not show an odd-even asymme-

try. This indicated that the charge state distribution was not determined by the x-ray pulse alone. Since the density of the sample is high, electron-ion collisions rates are high.

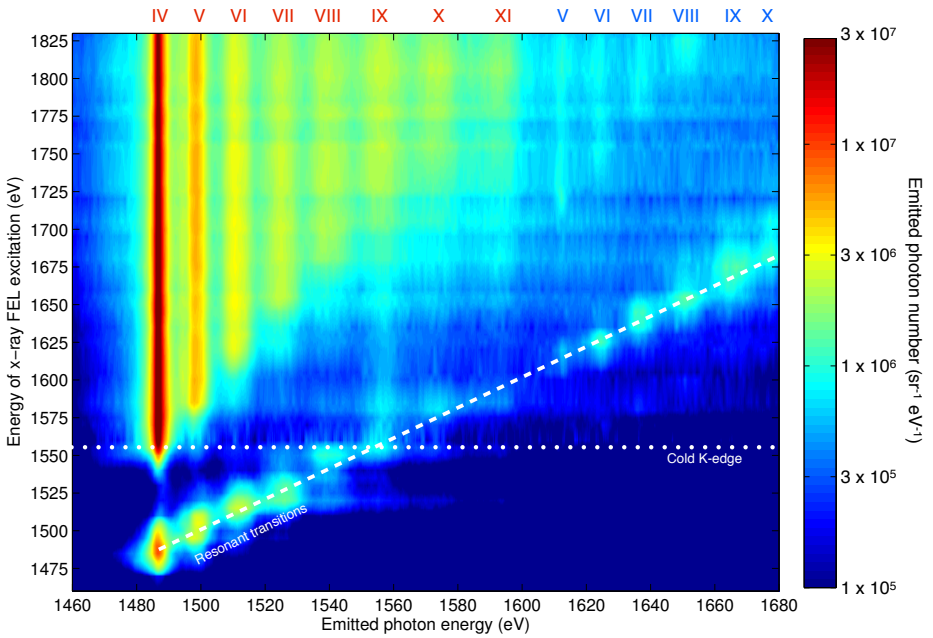

Figure 1.4: Emission from 1 µm aluminium sample as it is pumped with FEL radiation at different photon energies. The Roman numerals indicate the charge state from which the emission is observed, with blue indicating emission from double core holes and the red indicating single core holes. The K-edge for neutral cold aluminium (3+) is shown along with the line indicating those transitions which are resonant with the FEL radiation. This image is the combined results of Vinko *et al.* [32] and Cho *et al.* [33]

In order for an ion to emit a Kα photon it needs to have a vacancy in the K-shell which can be filled by an electron from the L-shell. As the number of electrons in the L-shell of an ion is decreased the energy of a Kα photon emitted from that ion increases, due to increased binding of the K-shell electrons. From the experimental results of Vinko *et al.* the K-edge energy of a charge state can be derived. At this energy it is possible to directly eject an electron from the K-shell to the continuum and so is the

minimum FEL photon energy at which the charge state will start to emit. These results are complicated through collisional processes, where an ion which has a K-shell hole due to photoionization can be collisionally ionized, removing an additional L-shell electron, such that it can emit a Kα photon from a charge state with a K-edge energy greater than the photon energy of the FEL [34]. However, there are sharp jumps in the amount of emission from a charge state as the photon energy is increased, so the K-edge energies of an individual charge state can be determined.

These measurements lead to the work of Ciricosta *et al.* [35], where it was found that the K-edge measurements were more consistent, in this case, with a model for the ionization potential depression by Ecker and Kröll [36] than the model of Stewart and Pyatt [37] (the standard model used in the community for 50 years).

As can be seen in figure 1.4 the FEL can excite transitions that are resonant with the energy of the FEL, such that Kα emission is observed below the K-edge of neutral cold aluminium. It is this emission which has been studied by the author and is described in chapter 3.

One of the main driving forces behind the advancement of XFELs has been that of biological structure determination [38, 39, 40, 41, 42]. The high intensities achievable in XFELs result in a paradigm shift in the way that x-ray crystallography is performed. Whilst in a typical synchrotron experiment the same (large) crystal is used for a long time and the key quantity in determining the damage it has undergone is the accumulated x-ray dose, in XFEL experiments many small samples are subjected to the x-ray beam where the dosage is such that the sample is destroyed. However, as the pulse lengths of the FEL pulse are very short the sample is able to diffract prior to the system blowing up, preserving the diffraction pattern.

In the case of crystals the increasing disorder in the electronic structure over the duration of the pulse reduces the intensity of the Bragg peaks, effectively meaning the observed peaks are only generated by the undamaged crystal early in the pulse [43].

Many proteins that would be interesting to study do not readily crystallize and so by reducing the size of crystal required many more proteins can be studied. Since the FEL 'diffract before destruction' crystallography method inherently far exceeds the damage thresholds for protein crystals methods for reducing the destruction, such as keeping sample at cryogenic temperatures, are no longer required. This means that the proteins which are analysed are closer to the natural state in which they would be found. In fact, in a recent experiment by Sawaya *et al.* live bacteria, within which a protein naturally crystallizes, were injected into the FEL beam and the structure of the protein determined [44].

One of the main fundamental problems in structure determination is that of the phase problem, since only information on the intensity, which is dependent only on the modulus squared of the electric field, is measured the information contained in the phase of the electric field is lost. The multiwavelength anomalous diffraction (MAD) method is a way of gaining this information. Near to an atomic absorption edge the atomic form factor will vary as a function of photon energy. This provides a means of determining the position of the anomalous scatterers and from this the phase of the remaining structure can be determined. In the high intensity conditions caused by FELs the samples will rapidly ionize, altering the position of the absorption edge and changing the anomalous scattering factor. This situation is discussed in more detail in section 4.8.

The short pulse length and large photon flux afforded by FELs have

allowed for increased temporal resolution of dynamical processes. The large number of photons in a single bunch allow for diffraction measurements to be made despite low scattering cross section, and the femtosecond length bunches mean that structural evolution on the timescale of picoseconds can be observed. The coupling of additional drivers, such as optical lasers, to systems under examination with FELs allows for the measurement of the response of the system.

The structure of photosystem II, a protein central to the oxygen fixation process in photosynthesis, was one of the first to be examined with FELs [45]. During photosynthesis this protein will absorb four photons over the Kok cycle. By examining the systems after different numbers of flashes from optical lasers changes in the structure can be observed through x-ray diffraction as well as x-ray emission spectroscopy giving information on the state of certain atoms within the complex [46]. Although at the current resolution changes in the structure between the different stages were not observed.

An experiment was also performed to observe a catalysed chemical reaction occurring on a surface. The reaction between oxygen and carbon monoxide will occur on a ruthenium surface when driven by an optical laser, and occurs within a few picoseconds [47]. In the experiment of Öström *et al.* x-ray absorption spectroscopy around the oxygen K-edge was used to identify which states the oxygen atoms were in after different times after the exciting laser pulse. Through this method a short lived transition state was identified. These kinds of time dependent measurements allow for understanding of chemical processes.

The use of a pump-probe situation with the x-ray FEL as both the pump and the probe is discussed in chapter 5.

1.3 Structure of thesis

Chapter 1 is an introductory discussion on x-ray free-electron-lasers and how these novel high-intensity x-ray sources can be used in studies of x-ray–matter interactions and plasma physics.

Chapter 2 contains a detailed description of the collisional-radiative code SCFLY, which is one the main tools used throughout the thesis to understand the experimental results and predict future results. The various atomic and plasma processes that are included within the code are outlined.

The next three chapters form the bulk of the thesis and research work involved.

Chapter 3 is mostly focussed on simulated results of opacity effects in an aluminium plasma heated with an FEL. By using an FEL tuned to a transition between the K-shell and the L-shell it is possible to generate copious Kα radiation even when pumping below the K-edge. However, due to the method by which this radiation is produced the effect of opacity on the emergent radiation is complicated, and it is this which is discussed in chapter 3. The results of this chapter formed part of a publication in *Physical Review Letters* in 2012 [33] with the full results of the chapter published in *High Energy Density Physics* in 2014 [1], with the author here being the lead author of that publication.

Chapter 4 consists of the description of another experiment on FEL heated aluminium where saturable absorption was observed. When the high intensity x-ray pulse interacts with the aluminium foil, the foil is ionized to such an extent that it is no longer possible for it to absorb x-rays through photoionization of a K-shell electron, leading to a reduction in the absorption rate and an increased transmission. The results of this chapter were published in *Physical Review Letters* in 2015 [2], with the author here as

first author of that work.

Chapter 5 is a description of simulation work on what could possibly be observed with a split and delay FEL setup measuring transmission. Following on from the work of the previous chapter where the transmission was experimentally seen to change as function of photon energy, chapter 5 is a discussion on what might be observed if a separate probe beam is propagated through the sample at various delays from the strong pump pulse. From this measurement the possibility of deriving the full time evolution of the sample is discussed.

Chapter 6 is a summary of the work presented and discussion of possible future work.

1.4 Author contributions

Due to the complex nature of FEL experiments the experimental results presented in this thesis were by necessity gathered through working as part of large collaborations, and it is important to clarify the role of the author in the work presented in this thesis.

The SCFLY code used throughout the thesis was written by H.-K. Chung and R.W. Lee, with some modifications made by O. Ciricosta.

All of the SCFLY simulations presented in this thesis were performed by the author. The codes written to generate the results in chapters 3 and 5 were written by the author.

The experiment which is referred to in chapter 3 was performed prior to the commencement of the author's DPhil, and so the author was not involved in the collection of the experimental data. Those responsible for the data collection and analysis are detailed in the author list of [32]. However the author did perform further analysis of the individual shot data shown in

section 3.5, and performed all of the theoretical analysis.

The author was part of the experimental team for the results in chapter 4. The full list of people involved in the experiment is in the author list of the *Physical Review Letters* publication [2]. The experiment was led by Orlando Ciricosta, who also performed much of the analysis of the spectroscopic data. However, the author performed all of the analysis of the diode data as described in section 4.2, along with its simulations which is the main data used in the major first-author publication resulting from the experiment.

CHAPTER 2

SCFLY

Throughout this work one of the primary tools has been the collisional-radiative code SCFLY. This chapter contains a description of the workings of this code and how this is useful in the diagnosis of hot dense plasmas.

2.1 Overview

When a high-intensity x-ray pulse from an FEL interacts with a sample, the sample will undergo a very rapid evolution. The absorption of x-ray photons is dominated by atomic transitions, particularly those of photoionization of core electrons. At the high-intensities of FELs many x-ray matter interaction events will occur in a short period of time. The excited configurations generated can decay through radiative and non-radiative processes, leading to a mixture of many possible configurations existing at a given time within

the sample. In SCFLY the populations of configurations are determined in a time-dependent manner through evaluating the rate of transitions between different configurations.

SCFLY uses the concept of super-configurations [48], where groups of atomic configurations (of similar energy) are collected into a single supershell. In SCFLY atomic levels are grouped according to the principle quantum number n. As an example the super-configuration $(1s)^2(2s2p)^6$ contains the configurations $(1s)^2(2s)^2(2p)^4$, $(1s)^2(2s)^1(2p)^5$ and $(1s)^2(2p)^6$. Since the supershells, in this case, are defined by the principle quantum number, throughout the remainder of this work the super-configurations will be denoted by the occupation of the K-, L- and further shells (i.e. $(1s)^2(2s2p)^6$ is denoted K^2L^6).

The number of possible configurations, and therefore transitions, increases with the number of electrons within an atom. The use of super-configurations allows for the number of transitions to be tractable for moderate Z elements. In SCFLY the maximum principle quantum number is limited to 10, however in practice in near-solid samples the highest of these levels will be removed due to ionization potential depression.

The configurations used in SCFLY is extended from those used in the widely available code FLYCHK [49] to include multiply excited configurations from inner-shells of the ground configuration. As an example SCFLY includes configurations that have a fully depleted K-shell, a series of species which have been observed emitting experimentally in samples heated by XFELs [32].

Broadly speaking SCFLY in the time-dependent mode solves the n_{eq}

coupled rate equations for each atomic level

$$\frac{N_i(t+dt) - N_i(t)}{dt} = \sum_{j \neq i}^{n_{eq}} R_{ji}(t) N_j(t) - \sum_{j \neq i}^{n_{eq}} R_{ij}(t) N_i(t) \tag{2.1}$$

where R_{ij} is the transition rate from a state i to a state j and N_i is the population of state i.

Another advantage SCFLY has over the FLYCHK code is that it calculates the temperature self-consistently using the energy of the transitions, including absorption of the laser, and the populations of ions and electrons [16]. Thus the time evolution of processes which are temperature dependent can be used to generate the evolution of the system given just the initial conditions and an input radiation field.

2.2 Atomic processes

Since SCFLY is a collisional-radiative model it uses the rates of the different transitional processes to determine the populations in a time dependent manner. To do this the code has to be provided with the relevant atomic data. Outlined below are the various types of atomic processes that occur and how the rates for each of them are calculated.

2.2.1 Radiative processes

In non-LTE situations the interactions with radiation fields are of great importance. The radiation generated by electrons transitioning in a sample can be categorized into three types; bound–bound, where an electron moves from one bound state to another, bound–free, where a free electron radiatively recombines with an ion, and free–free, where a free electron loses kinetic energy in a collision with electrons and ions (known as Bremsstrahlung ra-

diation). Radiation can be absorbed by electrons through the inverse of these processes.

Bound–bound transitions occur when an electron transitions from one bound state to another, accompanied by the release or absorption of a photon. The energy of the photon has a peak intensity at the energy difference between the two bound levels. The spontaneous emission rate from a level j to a level i is denoted A_{ji}. The stimulated emission and absorption processes are dependent on the radiation field as well as the coefficients B_{ji} and B_{ij} respectively. These two are related to each other by $g_i B_{ij} = g_j B_{ji}$, where g is the statistical weight of the respective levels.

Bound–free transitions occur between the bound levels and the continuum. The energy of photons emitted in radiative recombination is equal to the sum of the energy of the free electron and the binding energy of the shell that the electron falls into. Correspondingly there is a minimum amount of energy that can be released from a radiative recombination event, that being the binding energy of the relevant shell. The inverse of this process is photoionization. In SCFLY the cross-sections used for photoionization are a fitted expression which have the form

$$\sigma \propto \exp\left[c_1 + \frac{h\nu}{I_p}\left[c_2 + \frac{h\nu}{I_p}\left[c_3 + \frac{h\nu}{I_p} \times c_4\right]\right]\right] \tag{2.2}$$

where $h\nu$ is the photon energy, I_p is nominally the ionization energy and the various values of c are given in the atomic data file used by SCFLY. These fits are used since they match the values for the photoionization rate on the CXRO website [50]. Though the ionization potential depression will cause the ionization energy to shift, the value of I_p used to calculate the cross-sections is fixed (but the minimum photon energy where the transition can

occur is allowed to shift).

2.2.2 Collisions

In cases of high-density collisional processes will have a greater impact on the population distributions of ions. In the assumption of Local Thermodynamic Equilibrium (LTE) the populations of all possible excitation and ionization states are determined by the local temperature and density. The populations are determined by the Saha and Boltzmann equations. The particles will have a Maxwellian velocity distribution. For this framework to hold every process must be in detailed balance i.e. the number of processes from one state to another must be exactly balanced by the number of inverse processes [51]. In the case of radiative transitions this would require the radiation field to have a Planckian distribution and the photons be unable to escape. Since the systems described in this thesis are driven by x-rays from an FEL, the system will not inherently be in LTE. The x-ray photons lead to the generation of core hole states that are statistically unlikely at the temperatures achieved. In this sense the excited state populations cannot be described by an LTE formalism. However, if the collision rate is high some of the populations (such as the charge state distribution) will approximate to LTE levels.

The electrons generated by the x-ray interactions with the system are non-thermal. The electrons generated through photoionization will have an energy equal to the difference between the ionization energy of the electron released and the photon energy of the FEL. Electrons generated through Auger decay will have energies equal to the difference between the energy released by the electron that fills the core hole and the ionization energy of the electron released.

In SCFLY the electrons are assumed to be instantly thermalized, so the collision rates used are those of a thermal distribution characterized by a single temperature. If this assumption were not, at least partially, valid it would cast doubt on current simulation work and much more computationally intensive complex treatment of the electron energy distributions would need to be undertaken.

Work by Orlando Ciricosta using a simple model for the non-thermal Auger electrons in a modified form of SCFLY has shown that the approximation provides an accurate description of the system [52]. Work has also been performed by de la Varga *et al.* [53] using their bigbart code [54] to examine the effect of a non-Maxwellian electron distribution. They tracked the electron population in energy bins treated in the Fokker-Planck approximation [55] with some additional inelastic terms. In their simulations at near solid density with neon atoms they observe that thermalization of the electrons only occurs at the end of the FEL pulse. However, the populations of non-thermal electrons is small compared with the thermal electrons, except for at the very start of the pulse. The work in this thesis is concerned with solid-density aluminium which has a higher density than that simulated by de la Varga *et al.* and so thermalization times would be expected to be even less. Indeed through unpublished work by de la Varga and Velarde it is known that the thermalization of electrons in solid aluminium is rapid [56]. So throughout this thesis the free electrons are assumed to be instantly thermalized and characterized by a single electron temperature.

Collisional processes can lead to excitation of an electron, or the ionization of an electron from a bound level. In SCFLY the rates for collisional ionization used are those of Burgess and Chidichimo [57]. For a Maxwellian

distribution of free electron this has the form

$$\frac{R_{i,i+1}}{n_e} = 2.1715 \times 10^{-8} C\xi \left(\frac{I_H}{T_e}\right)^{3/2} \left(\frac{I_n}{T_e}\right)^{3/2} E_1\left(\frac{I_n}{T_e}\right) w\left(\frac{I_n}{T_e}\right) \tag{2.3}$$

where

$$w\left(\frac{I_n}{T_e}\right) = \left[\log\left(1 + \frac{T_e}{I_n}\right)\right]^{\beta/(1+T_e/I_n)}, \tag{2.4}$$

$$\beta = 0.25\left(\left[\frac{100z+91}{4z+3}\right]^{1/2} - 5\right), \tag{2.5}$$

E_1 is the exponential integral of the first kind, I_H is the Rydberg constant, T_e is the electron temperature, I_n is the ionization energy of the level, ξ is the number of electrons in the shell that is being ionized and C is a constant. The value of the constant used is 2.3, though recent work has suggested this should be increased by a factor of three to five for solid density aluminium [34].

The rate for collisional recombination, with a Maxwellian electron distribution, is related to the ionization rate by detailed balance as

$$R_{i+1,i} = 1.66 \times 10^{-22} n_e \frac{g_i}{g_{i+1}} \frac{e^{\frac{I_n}{T_e}}}{T_e^{3/2}} R_{i,i+1}. \tag{2.6}$$

Collisions can also lead to excitation and de-excitation of electrons in an ion. For a Maxwellian electron distribution the collision rate for a transition with a threshold energy of E_{ij} is given by

$$\frac{R_{ij}}{n_e} = 1.581 \times 10^{-5} \frac{\bar{g}(E_{ij}/T_e)\exp(-E_{ij}/T_e)}{E_{ij}\sqrt{T_e}} f_{ij} \tag{2.7}$$

where $\bar{g}(y) = 0.15 + 0.28e^y E_1(y)$ is the averaged gaunt factor and f_{ij} is the oscillator strength for the transition.

The rate for the inverse process of collisional de-excitation is given by

$$R_{ji} = R_{ij}\frac{g_i}{g_j}\exp\left[\frac{E_{ij}}{T_e}\right] \tag{2.8}$$

from detailed balance.

As the work later in this thesis is concerned with plasmas of a finite size, care must be taken to ensure that the electrons do not travel far before undergoing a collision. Electrons with a higher energy will travel further before colliding. For an electron with an energy of E the collisional ionization cross-section is given by

$$\sigma_{ii+1}(E) = \pi a_0^2 C\xi\left[\frac{I_H}{I_n}\right]^2\left[\frac{I_n}{E}\right]\ln\left[\frac{E}{I_n}\right]W\left[\frac{E}{I_n}\right] \tag{2.9}$$

where $W\left[\frac{E}{I_n}\right] = \left[\ln\left(\frac{E}{I_n}\right)\right]^{\frac{\beta I_n}{E}}$ if $E > I_n$ and zero otherwise [57].

For $I_n = 73\,\text{eV}$ (the cold L-edge energy), $E = 1400\,\text{eV}$ (the typical energy of an Auger electron), z=3 (the charge on the ion) and ξ=8 (the number of electrons in the L-shell of a 3+ ion) gives σ=1.188×10^{-17} cm^2. If the ion density is $n = 6\times10^{22}\text{cm}^{-3}$ (solid-density) the mean free path of the electron is around 14 nm, and given the speed of the electron this gives a timescale of less than a femtosecond. This distance is much less than the size of the plasmas in this work and so the use of a zero-dimensional code is justified.

2.2.3 Non-radiative processes

Also included in SCFLY are the processes of autoionization and electron capture. When an electron is removed from an inner shell, the vacancy can be filled by an electron in a higher shell falling into the vacancy and the excess energy removed by the ejection of another electron, this is the Auger

process. Autoionization can also occur if two or more valence electrons are excited. The rates for these processes are in the data file used by SCFLY.

From this rate the rate for the inverse process (electron capture) can be computed.

2.3 Plasma effects

2.3.1 Ionization potential depression

The energy required to remove an electron from an atom is known as the ionization potential. In a finite density plasma the energy required to ionize an electron from an ion will not only be influenced by the electrons in that ion but also by the free electrons and neighbouring ions. By having these perturbers present the maximum energy which an electron can have and still be considered bound is reduced, the lowering of this energy means that the ionization potential is reduced. In a simplistic view it can be thought of that when ions are brought closer together the number of outer electron which can be singly assigned to an ion is reduced. Since there is a lowering of the energy required to remove an electron the charge state distribution will be altered.

In SCFLY two possible models for the Ionization Potential Depression (IPD) are available. Firstly the model of Stewart and Pyatt [37], which has been the standard model used in the community, gives the IPD as

$$\Delta I_{\mathrm{SP}} = \frac{k_B T}{2\left(z^* + 1\right)} \left\{ \left(\frac{3\left(z^* + 1\right) z e^2}{\lambda_D k_B T} + 1 \right)^{2/3} - 1 \right\} \tag{2.10}$$

where λ_D is the plasma Debye length including both ions and electrons, z is the charge of the ion after the ionization has taken place (i.e. $z = 1$ for a neutral atom), z^* is defined as $\left\langle z^2 \right\rangle / \left\langle z \right\rangle$.

Through the work of Ciricosta *et al.* [35] it was found that an earlier model of the IPD by Ecker and Kröll [36] gave a better correspondence to their experimental data, at least for solid density aluminium. The model of Ecker and Kröll takes different forms depending on whether the local electron density is more or less than a critical value, $n_{\text{crit}} = \frac{3}{4\pi}\left(\frac{k_B T}{Z^2 e^2}\right)^3$, where Z is the maximum ion charge possible (i.e. $Z = 13$ for aluminium). Below this density the IPD follows that of Debye-Hückel i.e.

$$\Delta I_{\text{EK}}(n_e < n_{\text{crit}}) = \frac{ze^2}{\lambda_D} \tag{2.11}$$

and above this density having the form

$$\Delta I_{\text{EK}}(n_e > n_{\text{crit}}) = C\frac{ze^2}{r_{\text{EK}}} \tag{2.12}$$

where C is a multiplicative factor, z is defined as in the Stewart-Pyatt model and r_{EK} is defined by $4\pi r_{\text{EK}}^3 = 1/[n_e + n_i]$, with n_e and n_i being the density of electrons and ions respectively. The value of C is chosen to be equal to 1, though this does not provide continuity in the IPD it does reproduce the experimental results.

Recent work on the IPD using density functional theory has been shown to successfully reproduce the results that questioned the use of the Stewart-Pyatt model [58]. However the computation time associated with such calculations is unfeasible to be used within a collisional-radiative code, so the more simple models are used. Since the Ecker-Kröll model has been shown to reproduce experimental results for solid-density aluminium it is this model that is used for the IPD throughout this work.

2.3.2 Opacity effects

In a plasma that has spatial extent it is possible for a photon that is emitted to be reabsorbed elsewhere in the plasma before it can escape. To account for this codes such as SCFLY make use of the escape factor formalism. In this the spontaneous decay rates are modified to account for some of the emission being reabsorbed, thus impacting the populations. This is a computationally efficient way to include the effects of radiation trapping.

In SCFLY the escape factor for Voigt line profiles used is that of Apruzese [59, 60]. For Voigt profiles there are two regimes, where the Doppler part dominates and where the Lorentzian part dominates, which is determined by the Voigt factor $a = \frac{\Gamma}{4\pi\Delta\nu_D}$, where Γ and $\Delta\nu_D$ are the Lorentizian and Gaussian widths respectively.

The probability of emission from a single depth within the plasma escaping to an optical depth of τ is approximately given by the following.

If $a < 0.49$

$$P_e(\tau) = \begin{cases} (1 + 1.5\tau)^{-1} & \tau \leq 1 \\ 0.4\tau^{-1} & 1 < \tau \leq \tau_c \\ 0.4\left(\tau_c\tau\right)^{1/2} & \tau > \tau_c \end{cases} \tag{2.13}$$

$$\text{where } \tau_c \equiv \frac{0.83}{a(1 + a^{1/2})} \tag{2.14}$$

and if $a > 0.49$

$$P_e(\tau) = \begin{cases} (1 + \tau)^{-1} & \tau \leq 1 \\ 0.5\tau^{-1/2} & \tau > 1 \end{cases} \tag{2.15}$$

Since emission will occur from all depths within the plasma the total

escape factor is given by evaluating

$$\frac{\int_0^{\tau_0} P_e(\tau)\mathrm{d}\tau}{\int_0^{\tau_0} \mathrm{d}\tau} \tag{2.16}$$

where τ_0 is the optical depth at the line centre for the relevant spatial distance.

Escape factors are a useful means of coupling the radiation field and populations, but are most effective when plasmas are homogeneous and so do not have large gradients in temperature and density. As will be shown later in this thesis, the atomic populations are predominantly determined by the intense FEL radiation, and thus opacity effects are mainly confined to the subsequent radiation transport, rather than the atomic kinetics.

2.4 Spectral module

SCFLY uses super-configurations to evaluate populations, however radiative transitions between these levels would not give the level of detail that is observed in an experiment. Therefore to give a better representation for the simulated emission spectra a more detailed set of atomic levels is used in the spectral module, which post-processes the populations output by the main SCFLY code. The various subshells are populated statistically from the super-configuration populations.

The emissivity for a bound–bound transition between an upper level, u, and a lower level, l, is given by

$$\epsilon_\nu = N_u A_{ul} \left(h\nu_{ul}/4\pi\right) \phi(\nu) \tag{2.17}$$

and is in units of $\mathrm{erg\,cm^{-2}\,s^{-1}\,Hz^{-1}\,srad^{-1}}$.

The opacity for the same transition is given by

$$\kappa_\nu = N_l \left(1 - \frac{N_u g_l}{N_l g_u}\right) \frac{\pi e^2}{mc} f_{lu} \phi(\nu) \tag{2.18}$$

and has units of cm^{-1}. The quantities A_{ul} and f_{lu} are the spontaneous emission rate and oscillator strength of the transition respectively.

The emission and opacity from bound-free transitions are treated as they are in the population determining part of SCFLY, albeit with more transitions.

2.5 Radiation transport

Having generated photon energy dependent emissivities and opacities it is possible to synthesize the emergent radiation.

The standard equation of transfer relating the intensity I_ν, the source function $S_\nu = \epsilon_\nu / \kappa_\nu$ and optical depth τ_ν at a given frequency is

$$\frac{\partial I_\nu}{\partial \tau_\nu} = S_\nu - I_\nu. \tag{2.19}$$

With some manipulation this can be rearranged to give

$$I_\nu = \int_0^L \epsilon_\nu (y)\, e^{-\int_0^y \kappa_\nu(x)\mathrm{d}x} \mathrm{d}y, \tag{2.20}$$

assuming that there is no radiation other than that emitted. The quantity L is the geometric path depth. This can be understood as any emission from a depth y will have to pass through an optical depth of $\tau_\nu(y) = \int_0^y \kappa_\nu (x)\, \mathrm{d}x$ before exiting the plasma.

In the case of a homogeneous plasma the expression simplifies to

$$I_\nu = S_\nu \left(1 - e^{-\tau_\nu(L)}\right) \tag{2.21}$$

In the limit of $\tau_\nu(L) \to \infty$ the emergent radiation is just that of a black body. In the optically thin case, where $\tau_\nu(L) \to 0$, the radiation is given by $I_\nu = \epsilon_\nu L$.

In chapter 3 the situation where the plasma is not homogeneous will be explored, with the emission from one region experiencing differing levels of opacity as it traverses the plasma.

CHAPTER 3

Opacity effects in FEL heated aluminium

With the arrival of 4th generation light-sources and intensities in the x-ray regime of $> 10^{17}\,\mathrm{W\,cm^{-2}}$ becoming a reality, the way has been opened for investigations into non-linear phenomena in this range. In this chapter simulation work on the opacity broadening of spectral lines generated by an x-ray free-electron-laser heated aluminium plasma will be presented.

3.1 Resonant pumping of Kα experiment

The experiment to which the simulations pertain was performed on the SXR beamline of the LCLS in 2010 [33]. An image of the experimental hutch is shown in figure 3.1. The experiment involved directing the focussed radiation of the XFEL onto a 1 µm thick sample of aluminium. The wavelength of the FEL was scanned through a range, and it was found that when it was

resonant with a transition between the K- and L-shells of the atom copious amounts of Kα radiation was produced. When irradiating with a more conventional x-ray source Kα radiation will only be produced when the sample is irradiated with x-rays of a photon energy greater than the K-edge energy. With this amount of energy a single photon can eject an electron from the K-shell into the continuum. The resultant hole in the K-shell can be filled by an L-shell electron decaying radiatively, producing Kα radiation.

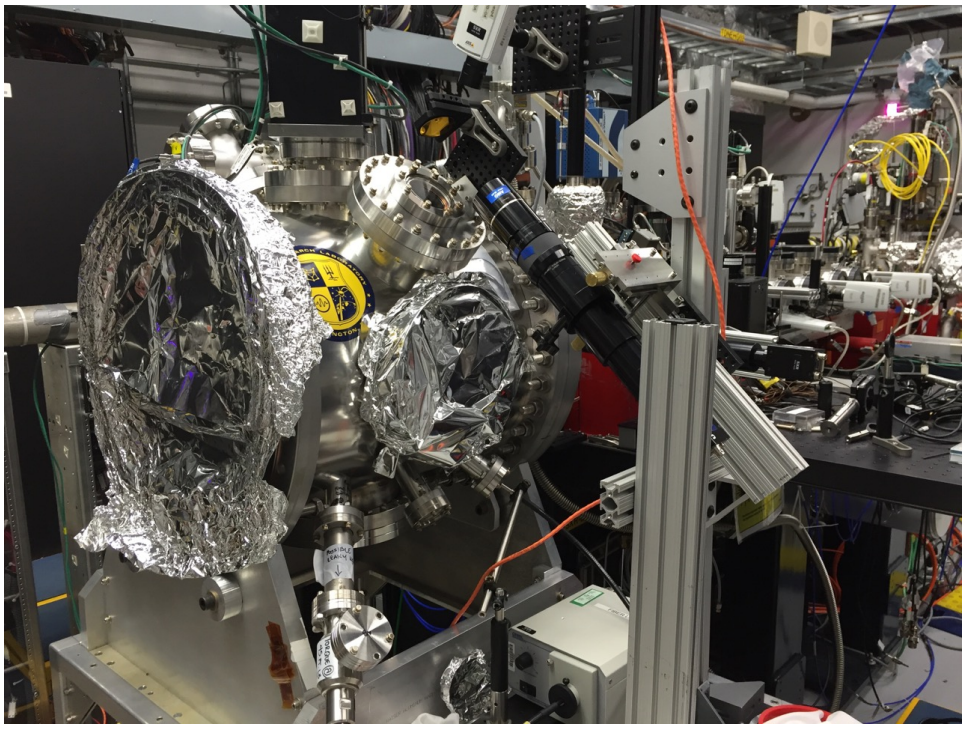

Figure 3.1: A photo of the SXR beamline. Image taken by Sam Vinko.

In contrast, to generate the Kα below the K-edge requires a multi-stage process. As the photon energy of the FEL is insufficient to directly ionize electrons from the K-shell, the FEL radiation will initially be absorbed primarily through photoionization of the L-shell. This process leaves a hole in the L-shell, and the possibility to excite an electron from the K-shell to the L-shell. If the FEL is tuned to the energy of this transition then a photon

may be absorbed. Subsequent to the absorption, the atom will be in a state where it now has a hole in the K-shell. This K-shell hole is filled by an electron falling from the L-shell. This process of decay will either release an L-electron (Auger decay) or a photon (Kα radiation). The electrons released through the photoionization and Auger processes can have energies in the region of 1400 eV. In the solid-density target these will undergo collisions and rapidly thermalize, raising the electron temperature of the system. As the temperature is raised it becomes possible for ionization of the ions to occur due to collisions. At the temperatures achievable in the experiment only L-shell electrons can be stripped off the ions. Through the collisional ionization other atoms may be brought into a state where they can absorb the FEL photons on a resonance. As the cross-section for absorbing the x-ray photons through the excitation process is very high, when the relevant ionization stages are present the x-ray-matter interactions will be dominated by the photo-excitation process. The process for generating Kα radiation, when the FEL photon energy is equal to the energy of the transition, is shown pictorially in figure 3.2.

For the experiment the FEL photon energy was scanned from 1480 eV up to 1580 eV. The photon energies were chosen such they start just below the energy of the Kα radiation and end just above the K-edge of cold aluminium. The x-ray pulses are quasimonochromatic, with a bandwidth of about 0.5%. The aluminium sample was a 1 µm thick foiled oriented at 45° to the beam direction. The pulse length of the LCLS pulse was estimated to be less than 80 fs. The pulse was focussed to a spot of around 3 µm diameter on target. The plasma created was diagnosed through emission spectroscopy, using a flat ammonium dihydrogen phosphate (101) crystal and an in-vacuum x-ray charge-coupled device (CCD).

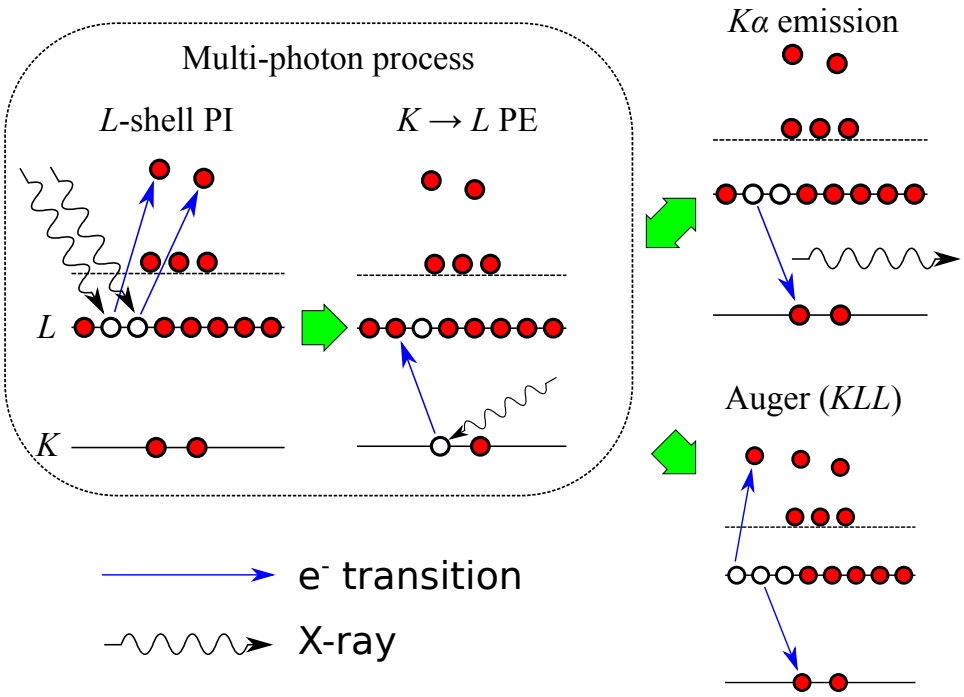

Figure 3.2: Diagrammatic representation of how Kα radiation can be produced from a 5+ aluminium ion, with an FEL tuned to the energy of the K- to L-shell transition.

An accurate knowledge of the fluence distribution of the FEL focal spot is essential in being able to accurately reproduce the experimental results. The focussed FEL radiation will have a range of intensities, each leading to varying levels of emission. Whilst the highest intensity regions will likely give large amounts of emission, it is conceivable that the regions with lower intensities will contribute more to the total emission of the sample due to a greater spatial weighting.

The method of determining the spatial distribution used was the so-called fluence scan (or f-scan) [61, 62, 63]. In this method the FEL beam is focussed onto a target which has a sharp and invariable ablation threshold. Above this threshold the target will be ablated whilst below the threshold it will not. In essence this will give a contour of where the FEL beam fluence is above the threshold. By varying the energy of the FEL pulse, through the use of gas attenuators, the contours for higher fluences can be determined. For example, if the FEL is attenuated by a factor of two, the contour of the ablation will correspond to a fluence in the unattenuated beam of twice the threshold fluence.

Using the contours a distribution can be built up that relates the area of the contour to the fluence of the x-ray beam. This gives a fluence distribution as a function of area (denoted $f(S)$). The normalized fluence distribution is the fluence distribution divided by the peak fluence such that it has a maximum value of one at the peak. The effective area of the beam is obtained by integrating the normalized fluence distribution, or equivalently it is the energy of the pulse divided by the peak fluence. In the case of a Gaussian beam the effective area is equal to the area at which the fluence is $1/e$ of the peak fluence. In the case of a beam that is made of the sum of two Gaussian modes, i.e. $f(S) = f_1 \exp(-S/A_1) + f_2 \exp(-S/A_2)$ (where

$f_1 + f_2 = 1$), the effective area is given by $A_{eff} = f_1 A_1 + f_2 A_2$. This form of distribution is a model that can be exploited for cases where there is a broad background in addition to the main peak.

Since this only gives a relation between the fluence and the area in the remainder of the work presented here the distribution is assumed to be radially symmetric. In the experiment being described here the f-scan measurements lead to the derived distribution of $f(S) = 0.888\exp(-S/4.96) + 0.112\exp(-S/41.2)$, where S is the area in microns squared. The measured contours and the derived distribution using two Gaussian modes is shown in figure 3.3.

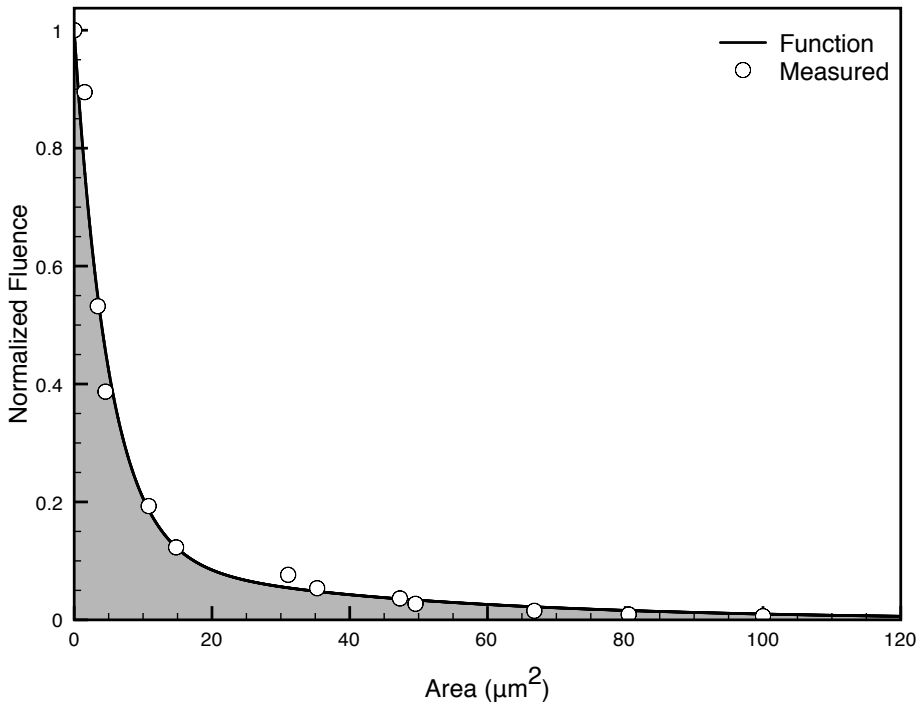

Figure 3.3: The FEL fluence as a function of area. The measured points are the area of ablated regions of the target when experiencing the FEL beam attenuated by various amounts.

When the FEL is tuned to the photon energy of the cold Kα at 1487 eV,

the absorption initially proceeds through photoionization of an L-shell electron. This state, with a hole in the L-shell, persists for around 40 fs (the Auger lifetime) and during this time can absorb another photon by exciting an electron from the K-shell into the hole in the L-shell. The resulting state, with a hole in the K-shell, will decay radiatively in about 3% of cases, the fluorescence yield [64], with the remainder decaying by the Auger process. As the method described to produce Kα radiation requires multiple x-ray photons, the probability of generating Kα will be intensity dependent. At the centre of the focal spot multiple ions will be able to produce Kα radiation, whereas in the wings of the focal spot ions may only absorb one photon during the pulse. Therefore in the peripheral regions it will be possible that there are many ions with L-shell holes, that can not only absorb the radiation from the FEL, but also the Kα radiation from emitted by ions in the centre of the focal spot. Due to this reabsorption optical depth effects will influence the observed spectrum. These opacity effects are a complicated function of both spatial and temporal distributions, and it is this that is the subject of the simulations later in this chapter.

3.2 Simulation setup

The simulation work was performed using the SCFLY collisional-radiative code [65, 16], which is an extension of the commonly used FLYCHK code [49]. Whereas FLYCHK is mainly used in matching simulated spectra with experimental spectra for a single temperature and density, SCFLY contains a means of calculating a self-consistent temperature and can do this in a time dependent manner, given an input radiation field. Other differences include that there are a greater number of possible configurations in SCFLY, including configurations with an empty K-shell, that are not included in FLYCHK.

Using the SCFLY code time-dependent populations, emissivities, opacities and temperatures can be generated, given an external radiation field. The temperature is determined by working out how much energy is absorbed from the radiation field, and then assuming instant thermalization of all the free-electrons generated (whether they are generated in photoionization, collisional ionization or Auger decay). Since the FEL does have a finite bandwidth, when considering the absorption and transmission of the FEL through the sample, the frequency dependent opacities must be used. These allow the spectrum of the FEL to alter as it traverses the target. The SCFLY code is a zero-dimensional code, however the energy deposited in a thin layer can be calculated using Beer's law. Throughout the remainder of the work it is assumed that the ion populations are determined only by the external radiation field, and not by emission from the plasma itself, though this assumption will be justified in the next section. By making this assumption it is possible to model the full, spatially non-uniform pulse as a series of separate SCFLY simulations.

The full FEL-target interaction is modelled by dividing the 1 µm target into a series of ten layers, each 100 nm thick (such that they are small compared with the absorption depth at the FEL wavelength). Each of the layers is then divided into a grid of 100 nm by 100 nm squares, giving a three-dimensional array of cells. Each of the cells is associated with an SCFLY simulation, given by the radial distance from the centre of the focus (determining the intensity at the surface) and the depth within the target. As the FEL traverses the target the absorption will change, so the input intensity for each layer is equal to the transmitted intensity from the previous level, calculated using a frequency dependent Beer's law. The photon energies of 1487 eV and 1580 eV were chosen such that they matched the experiments

of Cho *et al.* [33] and Vinko *et al.* [32]. The temporal profile chosen initially was a Gaussian shape with a full width half maximum (FWHM) of 80 fs, and the spatial profile was chosen to match the profile given by imprints taken during the experiment. The geometric setup used for the simulation is shown in figure 3.4. The target is oriented such that the FEL beam arrives at a 45° angle to the target normal.

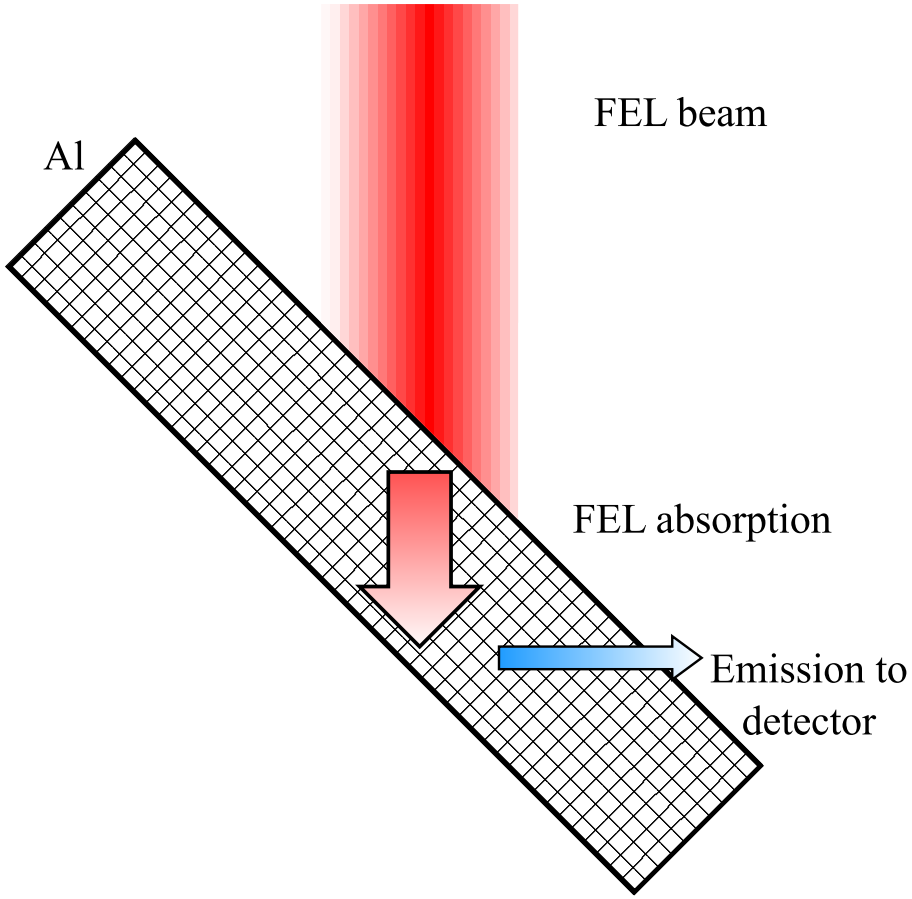

Figure 3.4: Geometry considered for the simulations. Each cell is simulated for an FEL intensity based on the radial profile of the beam, and attenuation due to the preceding layers. The emission is attenuated along the line of sight to the detector.

The SCFLY simulations give the emissivities and opacities of each of the cells. The emissivities are used to calculate the spectrum emitted from each

cell. To calculate the experimentally observed spectrum, the emission from each cell is multiplied by a factor of the form $e^{-\sum_i \kappa_i a_i}$, where i indicates the cell the emission passes through from the centre of the emitting cell to the detector, κ_i is the opacity of each cell passed through, and a_i is the distance travelled within the cell. Summing the emission from all the cells gives the emission rate at a given time. The procedure is repeated for each timestep and integrating the resulting rates gives a total emission to be compared with the experimental spectrum. Each ray is assumed to pass instantaneously from the sample, as the time for escape is less than the time between timesteps.

3.3 Self-emission

The scheme outlined previously is reliant on the assumption that the dynamics within a cell are purely determined by the incident local FEL radiation, and neglects the possibility that emission from other regions of the target will significantly alter the plasma conditions. Often in zero-dimensional codes the effects of self-absorption of the emission is treated through the use of escape factors [66]. These allow for a computationally efficient means to evaluate the effect on the evolution of the plasma of any radiation produced. Escape factors are implemented by modifying the decay rates of radiative transitions to account for the radiation that is produced but reabsorbed before it can escape. The escape factor used in SCFLY is that as described by Apruzese [59, 60]. Escape factors are of greatest use in situations with high symmetry and absence of gradients in the plasma conditions. In SCFLY the escape factor formalism can be used in a single simulation where opacity effects are important, and relies on providing the pertinent spatial dimension, which has been shown to be the mean chord for calculation of atomic

populations and the physical line-of-sight length for spectra synthesis [67]. However, in the situation here the FEL radiation intensity is many orders of magnitude greater than the self-emission of the plasma. Due to this it is asserted that the evolution of the populations within the system is dominated by the interactions between the FEL radiation and the sample, and the spectra observed are largely unaffected by the interactions of the self-emission within the plasma. Consequently, the effect of trapping the self-emission on the atomic populations is neglected in the later simulations shown here. This leads in to the major assumption of this work: that emission from the plasma of one cell will not effect the populations of a neighbouring cells, and the observed spectrum can be calculated by summing the emission from each cell, taking into account the absorption along the line-of-sight to the detector (but not allowing the absorption to modify the plasma conditions in the cells traversed), i.e. opacity affects the line widths via radiation transfer, but not the populations.

In order to justify this assumption, it needs to be shown that the evolution of the system is sufficiently dominated by the FEL radiation that the effect of self-emission on populations that are spatially separated can be neglected. When pumping above the K-edge it is possible to justify this with an order of magnitude calculation. At a photon energy of 1560 eV the absorption length, when cold, is 0.9 µm. Thus, following Beer's law, around 67% of the photons that impinge on the target would be absorbed. As the K-shell fluorescence yield of aluminium is 3.6% [64], the number of photons emitted is around 2.4% of the number of photons originally passing through the sample, and 3.6% of the number that are originally absorbed. The photons that are emitted are emitted into 4π steradians and are thus further diluted at distances far from the central FEL focal spot.

The simple estimate just described will not be valid when pumping resonant with the Kα. At low intensities it would be expected that very little reemission will occur due to few L-shell holes being created, whereas at higher intensities there will be many more L-shell holes created and much greater possibility to absorb and subsequently reemit. As an effort to judge the validity of the assumption, the following simulations were set up. A simulation at the maximum intensity, with a depth of 1.5 µm, pumped at a photon energy resonant with the Kα energy (1487 eV) was performed and the emission spectrum generated. The emission spectrum is added to the input FEL radiation and another simulation is performed with this new external radiation field. The spectra produced in these two situations are are shown in figure 3.5 as lines (a) and (b). The fractional difference between the two spectra is also shown. From this it is very clear that there is little difference between the two spectra produced.

As the plasma is not actually spatial uniform, it may be expected that emission from a region of high FEL intensity will have more influence over the conditions in regions with a lower FEL intensity. So further simulations were performed using half the FEL intensity, the sum of the emission from the full FEL intensity simulation and half the FEL intensity, and the sum of half of the emission from the full FEL intensity simulation and half the FEL intensity. The emission spectra from these three situations are also shown in figure 3.5, labelled as (c), (d) and (e) respectively. Once again it can be seen that the difference in the emission spectra due to adding the self-emission of the plasma into the input radiation field is very small. Because of this neglecting the effects of the plasma self-emission on the state populations of neighbouring cells appears to be a valid assumption in this case of having an FEL that will determine the populations.

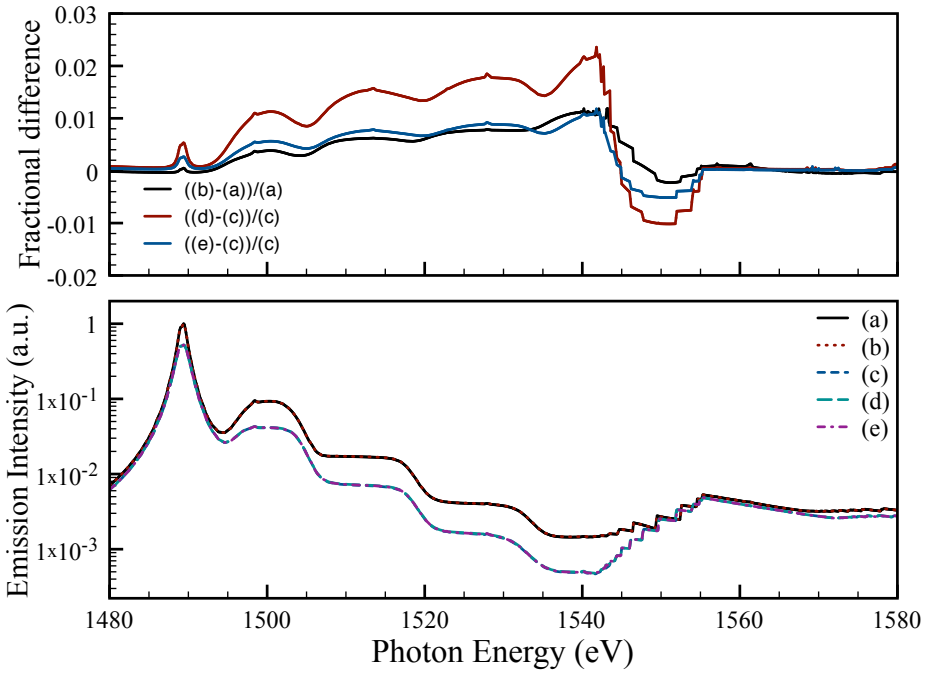

Figure 3.5: Bottom shows emission from a variety of situations. **(a)** Irradiated with full FEL intensity, **(b)** Irradiated with sum of full FEL intensity and emission from (a), **(c)** Irradiated with half FEL intensity, **(d)** Irradiated with sum of half FEL intensity and emission from (a), and **(e)** Irradiated with sum of half FEL intensity and half of the emission from (a). The top shows fractional differences between emission from certain pairs of simulations

These checks have dealt with the effect of reabsorption of the K-shell emission. The L-shell emission be an additional cause for concern. In cold aluminium the L-shell emission (which is bound-free emission) has an absorption depth of about 30 nm, which is about 30 times smaller than the sample size. This emission could cause redistribution of the L-shell holes however given the short range of the radiation and the low fluorescence yield of L-shell holes (0.075%[64]) this effect will be small.

3.4 Intensity dependent opacity broadening

Having justified the main assumption in the simulations, in this section simulated spectra from pumping at FEL photon energies of 1487 eV and 1580 eV will be presented. The setup used is that as in section 3.2. The simulations that are compared with experimental data are convolved with a 1.3 eV Gaussian to represent the experimental broadening effect and finite resolution of the x-ray spectrometer employed. The simulated spectra match both the above (figure 3.7) and below edge (figure 3.6) experimental data well. From the experimental data it was found that the main Kα peak had a different width when being pumped with 1487 eV photons compared with 1580 eV.

Without the imposed experimental broadening the simulated Kα peak is well fitted by a Lorentzian lineshape. By comparing the width of the Kα with and without considering the reabsorption as the emission transits the target to the detector, the extent of opacity broadening can be quantified. Although the main focus of this work is on the main Kα peak, it is worth noting that the other Kα peaks are also opacity broadened, but as they are weaker than the main peak and not present in all the simulations the effect is less easy to quantify. The width of the opacity broadened profiles was

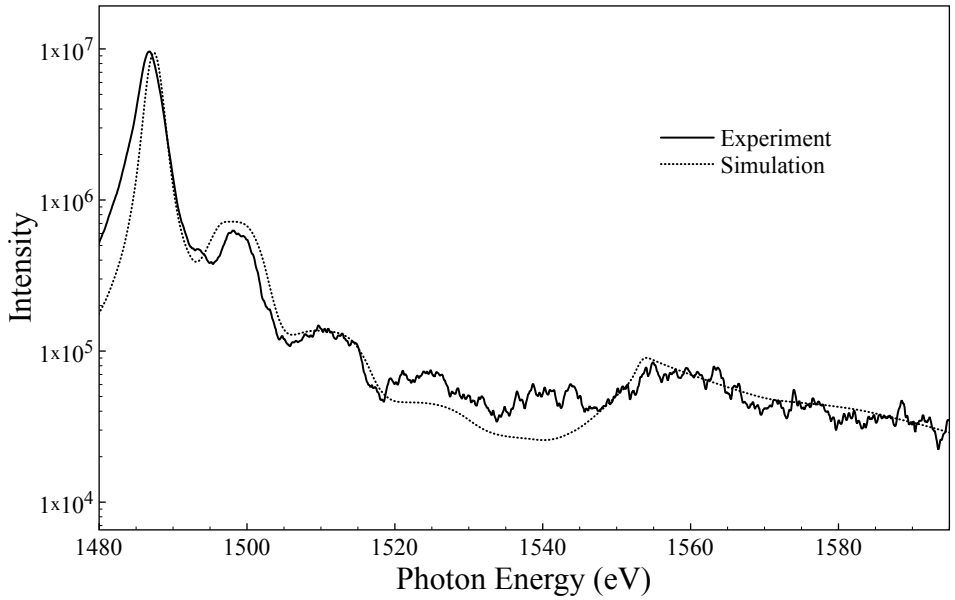

Figure 3.6: Simulated and experimental spectrum when pumping with the FEL tuned to 1487 eV, resonant with the Kα.

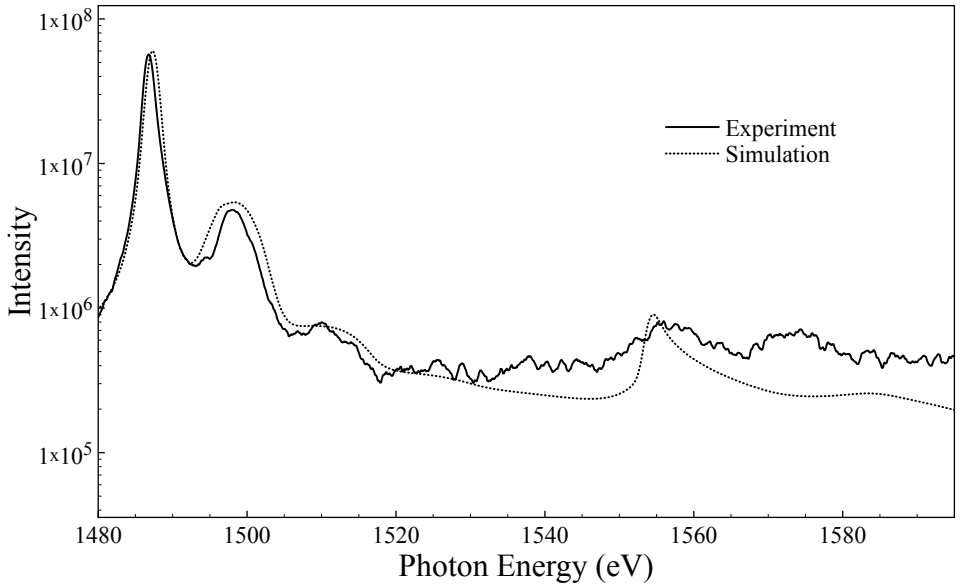

Figure 3.7: Simulated and experimental spectrum when pumping with the FEL tuned to 1580 eV, above the K-edge of cold aluminium.

seen to vary with the FEL intensity (figure 3.8). The variation in width is particularly prevalent below the K-edge, when pumping resonant with the Kα transition. At very low intensities the width of the opacity broadened line is very similar to the width of the line produced when neglecting the opacity. As the intensity is increased the width of the Kα increases, and then levels out. The species of critical importance in broadening of the main Kα peak is those with a full K-shell and a single hole in the L-shell, as these are the species that will resonantly absorb the radiation by a bound–bound transition. As the absorption length is related to the population density of this species, the spatial distribution of the ions with single L-shell holes is shown in figure 3.9. The figure shows the distribution at a series of times within the FEL pulse for two different peak intensities.

When pumping resonantly with the Kα, generating emission requires ions with single L-shell holes to absorb the FEL photons. The L-shell holes are generated by photoionization, however this has a long absorption length at 1487 eV of around 10 µm. The 1487 eV photons are resonant with the transition between the K- and the L-shell, when there is a single hole in the L-shell. When these species are dominant the absorption length for 1487 eV photons decreases dramatically to around 100 nm, increasing significantly how many photons are absorbed from the FEL and from the Kα emission.

At low intensities the Kα peak is narrow due to there being very few atoms generated which can absorb the radiation, so very little reabsorption occurs, leading to little opacity broadening. As the intensity is increased the number of ions which have a single L-shell hole increases, increasing the likelihood of absorbing the Kα radiation, broadening the peak. At the highest intensities the ions in the focal spot can be heated such that they have multiple L-shell holes, so are no longer resonant with the Kα radiation.

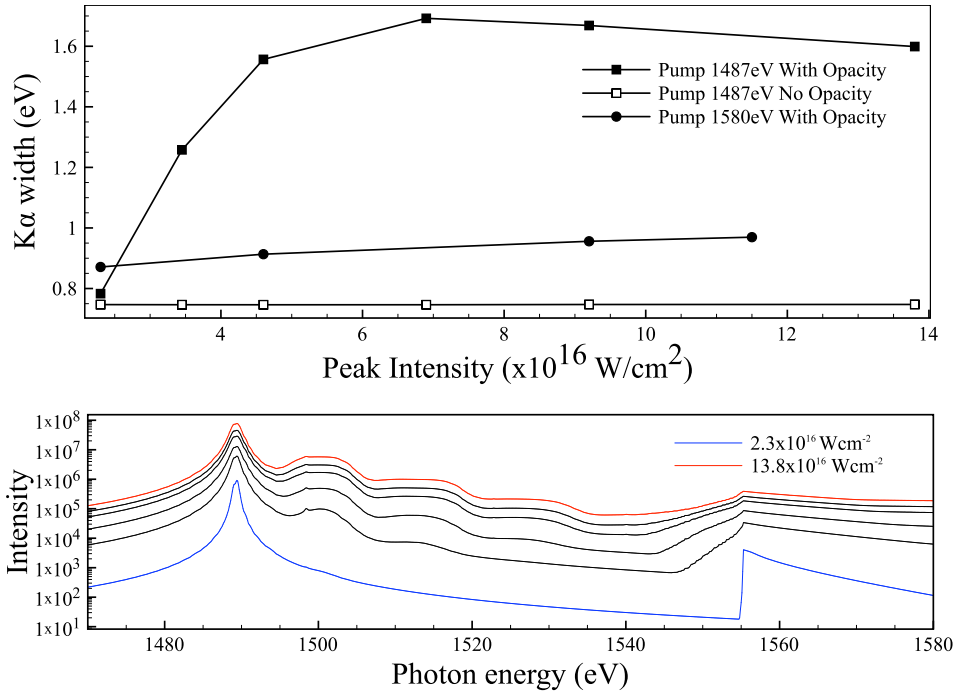

Figure 3.8: Simulated width of the Kα peak as a function of intensity with and without considering opacity when pumping with the FEL tuned to 1487 eV and 1580 eV. Also shown are the spectra produced for different intensities at a photon energy of 1487 eV.

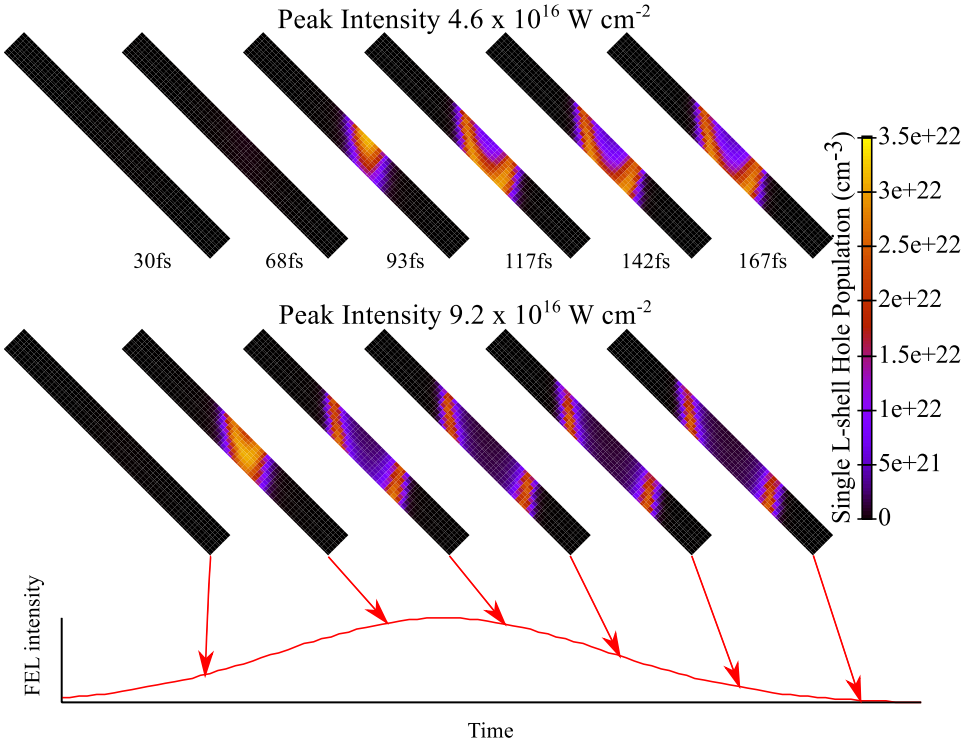

Figure 3.9: Simulated spatial distribution of ions with single L-shell holes in the central slice of the sample, when pumping at two intensities at different times in the pulse. The FEL is tuned to 1487 eV in this case.

The spatial distribution of the ions with many holes in the L-shell is such that a lot of radiation will pass through, but due to no longer being resonant, there will not be much reabsorption. This leads to there being a limit to the amount of opacity broadening that will occur.

In figure 3.10 the optical depth is shown for radiation of different photon energies when emitted from the centre of the target as a function of time. It can be seen from this that the optical depth of the Kα emission from each of the charge states increases rapidly when they are the dominant charge state of the system and then decreases again as the system evolves to a higher charge state.

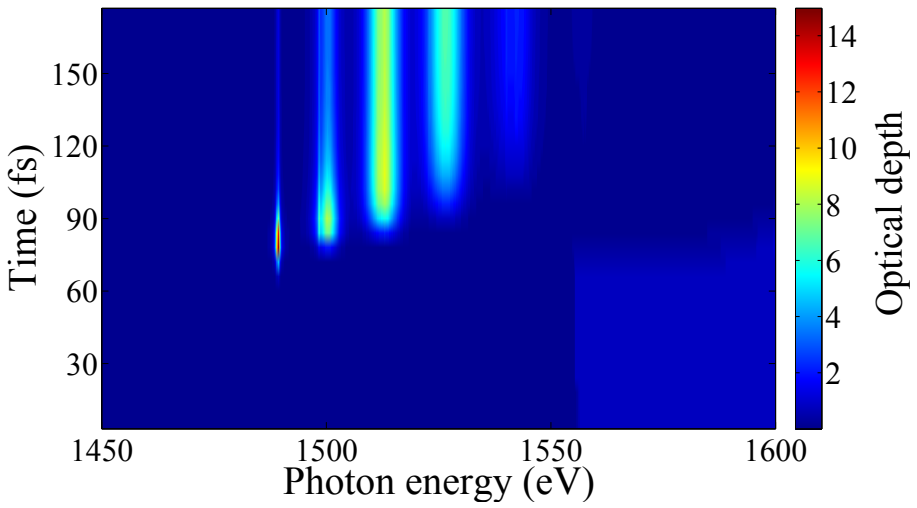

Figure 3.10: The simulated temporal evolution of the optical depth for a photon with a given energy emitted at the centre of the sample, when pumped with FEL radiation tuned to 1487 eV.

In the simulations that were performed with the FEL above the K-edge (1580 eV) the width of the Kα also shows a trend of increasing width with intensity (figure 3.8), however the broadening is not to the same extent as the below edge case, and there also isn't the same levelling of the width observed in the below edge simulations. When pumping above the K-edge it is possible

for Kα to be generated without the prerequisite for there to be ions with L-shell holes present. However as ions with L-shell holes will be generated due to collisional ionization by photoelectrons and Auger electrons (both when pumping with the FEL photon energy above and below the K-edge energy), there will be an intensity dependence to the opacity broadening in both cases.

As the FEL pulse traverses the target it is absorbed and so the intensity experienced by regions deeper in the sample will be less. However, as the rate of absorption will vary depending on what ion species are present the transmitted intensity has to be calculated self-consistently within the calculation. The intensity of the 1487 eV FEL pulse at a series of depths within the sample is shown in figure 3.11. From this figure certain features of the plasma evolution can be determined. At early times there is very little absorption due to the only absorption process that is available being L-shell photoionization which, at this photon energy, has a long absorption length. Around the peak of the pulse there are many ions with single L-shell holes which can resonantly absorb the FEL photons, leading to rapid attenuation through the sample. At later times the system has evolved such that ions with multiple L-shell holes are the dominant species, and can no longer resonantly absorb the FEL radiation. This leads the reduced absorption at the end of the pulse in figure 3.11.

Whilst emission from a homogeneous optically thick plasma will reach the black body limit, in the case of a non-homogenous plasma the phenomenon of self-reversal of emission lines can occur [68, 69, 70, 71]. So called because the line shape displays a dip at the line centre. In a standard laboratory plasma this will occur as radiation is generated and propagated through a hot region, before passing through a cooler region where less

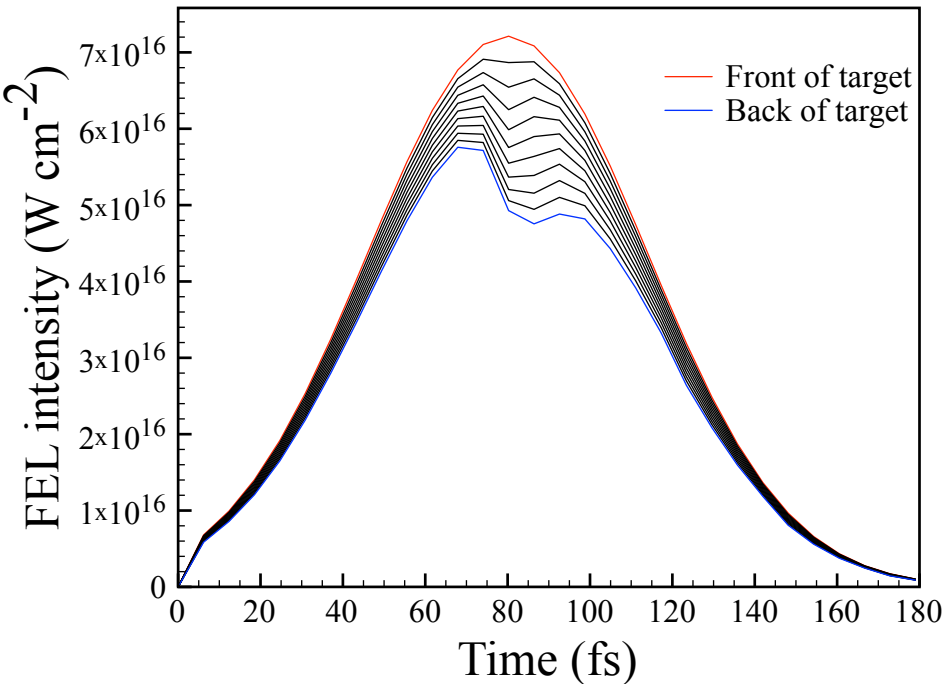

Figure 3.11: The simulated evolution of the temporal profile of the FEL pulse, tuned to 1487 eV, as it traverses the 1µm sample in 100 nm steps.

emission will occur but more absorption will occur due to many of the ions being in the ground state of the pertinent charge state. In addition, due to Doppler broadening, the line-shape of the emission from the hot region may be wider than the absorption line-shape of the colder region, enhancing the self-reversal that occurs. It is interesting to note that, although large optical depths are involved in the experiment, there does not appear to be any reversal occurring. This phenomenon can be understood by referring to figure 3.12. In part (a) the schematic for the situation of a standard thermally driven laboratory plasma is shown. The radiation from a bound–bound transition (in this case Helium-α) passes from the hot region through a cooler region. In the hot region there are many atoms in the excited state, whereas in the cooler region many atoms are in the ground state and so able to absorb the radiation leading to the self-reversal of the emission line. The situation is very different in the FEL excited case, as shown in figure 3.12 (b and c). In situation (b) the FEL is tuned to be in resonance with the He-α radiation, for the plasma to emit radiation of this wavelength it must be ionized such that there is a significant population of ions in the He-like ground state. These ions can then absorb the FEL radiation to subsequently emit He-α radiation. For this radiation to be reabsorbed it must encounter an ion in the He-like ground state, the population of these states will be located in regions very similar in conditions to those from where the radiation originated. Generation of the He-α radiation in the final case, where the FEL photon energy is tuned above the K-edge energy of the Li-like ion proceeds through the mechanism in part (c) of figure 3.12. In this case an electron from the K-shell of a Li-like ion in the ground state (this has one electron in the L-shell) is ejected through photoionization. The resulting ion is He-like in the excited state and can emit He-α radiation. For this radiation to be

reabsorbed it will have to encounter an ion in the He-like ground state (i.e. with no electrons in the L-shell), however these will be located in regions hotter than those where the radiation is emitted from, as these are dominated by Li-like ions, and subsequently as the radiation will traverse cooler regions, very little reabsorption will occur. So in complete contrast to the standard laboratory case these plasmas generated by creation of core-holes by the FEL are very unlikely to suffer the same effects of self-reversal.

3.4.1 Geometric considerations

Up until this point the only geometric configuration that has been considered is that as described in section 3.2. In this subsection the effects of the thickness of the target and the position of the detector shall be examined.

Reducing the thickness of the sample shifts the intensity at which the opacity broadening is greatest to a lower intensity. This shift is due to a lower intensity being required to force the rear of the sample to a highly emitting (and absorbing) state. As can be seen in figure 3.9, at the rear of the sample of the lower intensity case, even in the focus, the sample has not gone beyond having single L-shell holes. This reduces the depth from which the emission observed will come from in the sample, reducing the observed optical depth. In regions closer to the front surface of the sample this stage has been passed. So when the samples of reduced thickness are used the opacity broadening will peak at lower intensities, due to it requiring a lower intensity to force the rear of the sample (for which the emission has the largest physical distance to travel through) to go beyond the stage where it emits Kα.

The position of the detector will determine the distance within the sample that the radiation will have to traverse through. Furthermore, the regions

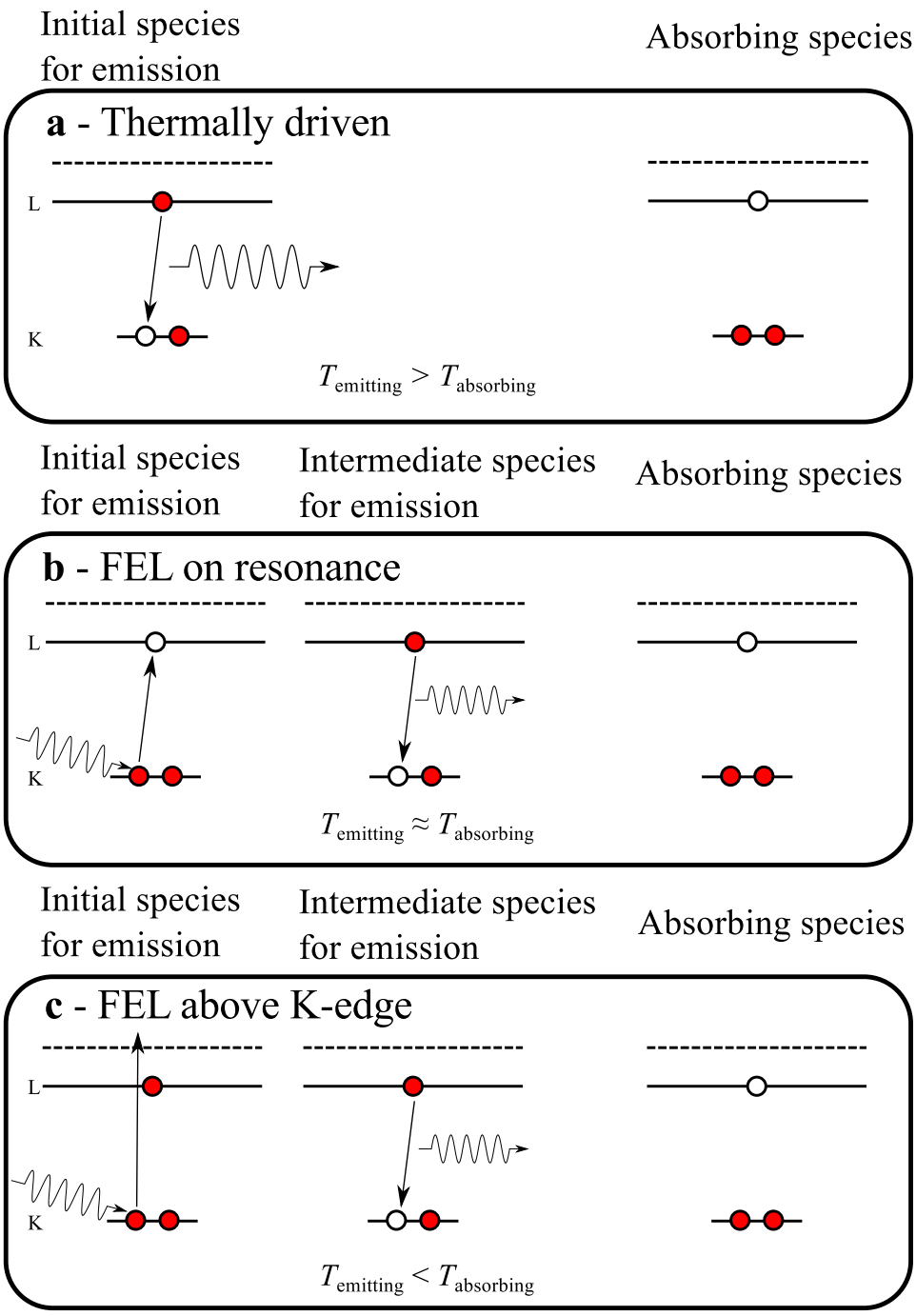

Figure 3.12: The mechanisms by which He-α is produced and absorbed in three regimes, (a) a thermally driven plasma, (b) a plasma driven by an FEL with the photon energy tuned to the He-α energy, (c) a plasma driven by an FEL tuned to a photon energy above the K-edge energy of Li-like ions. Comparisons between the temperatures at which the initial species for emission and the absorbing species are made in each case.

through which the radiation will now travel are different altering the absorption rate along the line of sight for the radiation that is detected. Figure 3.13 shows how the Kα peak is opacity broadened when observing the emission from different angles at different intensities. The emission back along the direction of the FEL has its maximal broadening at a lower intensity than any of the other detector angles considered. As the detector is moved away from this line the intensity of the FEL where the greatest opacity broadening is seen increases. Figure 3.14 shows how the Kα emission through the surface would appear from a few of the detector positions at different times in the pulse. This, in conjunction with figure 3.9, allows for understanding how the intensity at which the greatest broadening occurs changes with viewing angle. As the Kα is generated by exciting ions in the same state as those which are responsible for the reabsorption of the radiation, the emitting regions are nearly coincident with the regions of single L-shell holes. Radiation generated in certain regions, particularly towards the rear of the sample, will have to pass through multiple highly absorbing regions along its path to the detector. At higher intensities the highly absorbing regions get more spread out, leading to less of the emission passing through multiple highly absorbing regions. The shape of the highly absorbing regions will then determine the intensity at which the broadening is greatest for a given viewing angle.

3.4.2 Pulse duration effects

Given that the radiation generated by XFELs is produced through the self-amplified spontaneous emission (SASE) process, the temporal profile of each shot is not predetermined, and is random in nature. The profile is made up of sharp spikes, although the temporal profile of the electron bunch can give

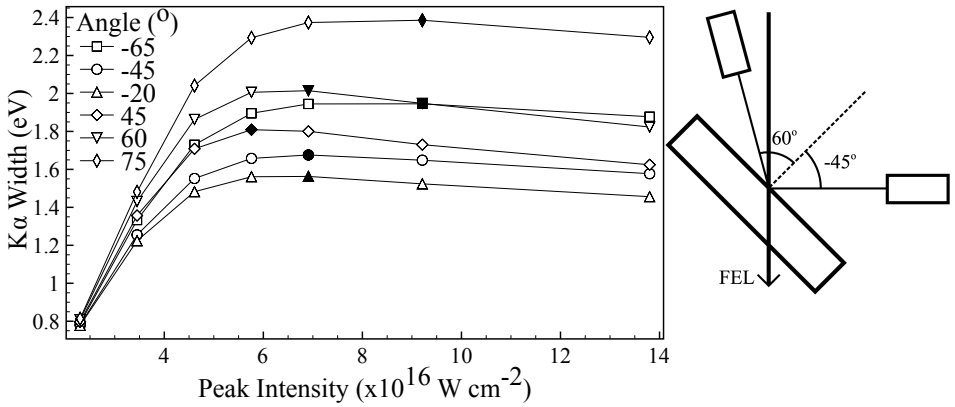

Figure 3.13: The simulated effect of changing the angle from which the sample is viewed on the opacity broadening of the Kα peak. Here angles are taken with respect to the normal of the sample, with the FEL beam direction being +45°. Example detector positions of +60° and -45° are shown in the diagram on the right. In the figure on the left, the solid symbols represent the intensity at which the broadening is greatest for a given viewing angle.

bounds as to the overall length of a pulse. Measurements of the temporal structure of FEL pulses remains an active field of research [72, 73, 74], but for these experiments still represents a source of uncertainty.

Due to this uncertainty all of the previous simulations were performed with a Gaussian temporal profile with a FWHM of 80 fs, i.e. a duration equal to the electron bunch length. However as some studies have shown the duration of the x-ray pulse length to be significantly shorter than the electron bunch length [73], additional simulations using a FWHM of 40 fs were performed and the results compared with the 80 fs cases.

Additional simulations were performed using a rapidly varying intensity within a Gaussian envelope. These simulations consisted of a series of pulses with duration of a few femtoseconds, with the peak intensity adjusted such that the fluence was the same as the smooth Gaussian pulses. The results of these simulations were almost identical to those of the smooth equivalents and so, given that a series of simulations using spiky pulses would require

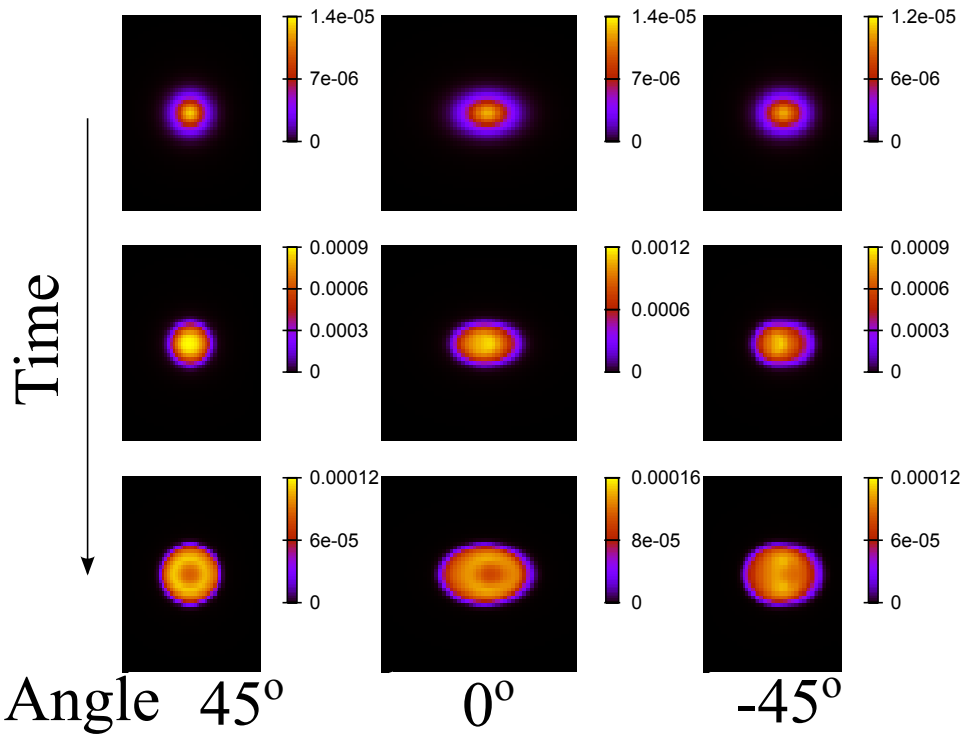

Figure 3.14: The simulated temporal evolution of the Kα radiation emerging from the surface as viewed from 45°(i.e. back along the FEL direction), 0°(the surface normal) and -45°(the original detector position), with the photon energy of the FEL tuned to 1487 eV.

significantly more computational resources without any gain in information, the work is focussed on the smooth pulses. The reason that these rapid variations can effectively be ignored is that the timescale of the evolution of the charge state distribution is on the order of tens of femtoseconds, so the variations of the intensity on the femtosecond and sub-femtosecond timescales will be averaged out [75]. The timescale of the evolution of the charge state distribution is around that of the total length of the FEL pulse.

When comparing pulses of different durations, it is important to discern whether any differences that arise are due to the intensity being changed, or whether it is the amount of energy incident (or equivalently the fluence) on the sample that alters the resultant spectrum observed. To this end, shown in figure 3.15 are comparisons between the emission from simulations with pulse lengths of 40 fs and 80 fs. The left column shows cases where the peak intensity of the two simulations are equal (and consequently the 40 fs pulse has half of the total energy of the 80 fs pulse), whilst the right column shows cases with equal fluence (i.e. the two pulses have equal total energy). From this figure it is clear that when the FEL is tuned to the Kα photon energy the intensity is the key determining factor on the resultant emission spectrum. When examining the extent of opacity broadening of the Kα in both cases it is again the intensity that is the determining factor, as can be seen in figure 3.16. The maximum amount of broadening occurs at the same intensity in both cases.

It is possible to understand why it is that intensity is the key quantity in this situation. As the FEL radiation is resonant with the Kα the ions that will absorb the FEL radiation are those with single L-shell holes. The majority of the absorption of the FEL pulse occurs when this population is at a maximum. During this time a lot of high energy electrons will be

generated through Auger decay of ions excited by the FEL, increasing the temperature and shifting the charge state distribution through collisional ionization. The number of ions that are able to emit Kα radiation is directly related to how many photons are absorbed at this time. So, the quantity of importance is how many photons reach the target over the duration of this process, i.e. the intensity. This is in contrast to what happens when the FEL photon energy is tuned above the K-edge. In the above edge case the spectra produced with identical fluences of FEL radiation are very similar, due to the emission not being reliant on a resonant process with a transient species [52].

3.5 Comparison with experiment

In this section comparisons of the simulations performed with experimental results will be made. In the experiment, as described by Cho *et al.* [33], in addition to pumping the sample with the FEL photon energy tuned to resonance with the Kα photon energy, the FEL was tuned to photon energies that were off-resonance. For each shot of the FEL there is an associated photon energy and pulse energy, and the experimental spectra were recorded on a single-shot basis. The x-ray photon energy is not directly measured, though it is well-correlated with the energy of the electron beam and from this the photon energy deduced. The pulse energy is measured through the use of a gas monitor detector (GMD) upstream of the final x-ray focussing optics. This number is converted to a pulse energy on target using a beamline transmission of approximately 30–34% [76]. The Lorentzian widths of Voigt fits to the first Kα peak are shown as a function of pulse energy on target in figure 3.17. The Gaussian part of the Voigt fits was taken to be 1.3 eV as in the work of Cho *et al.* [33].

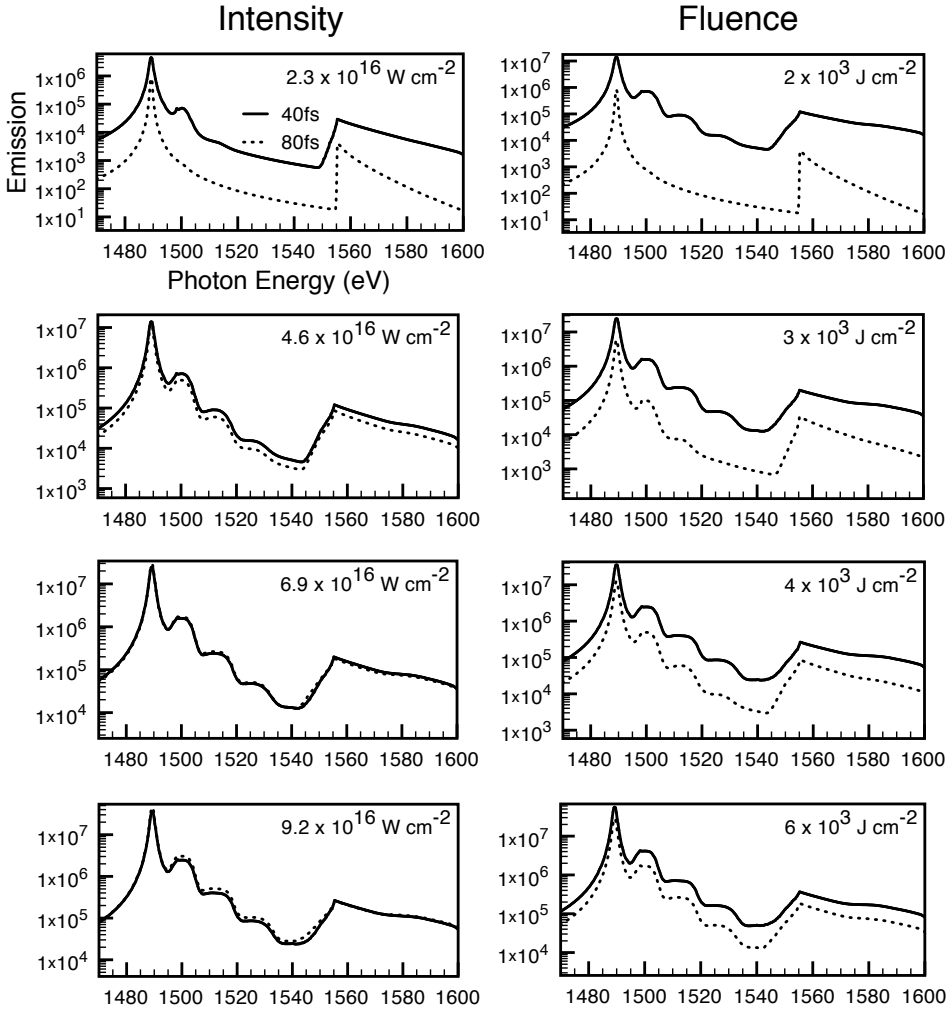

Figure 3.15: Simulated emission spectra in cases of equal peak intensity (left) or fluence (right), with pulse lengths of 40 fs (solid) and 80 fs (dashed). The FEL photon energy is 1487 eV.

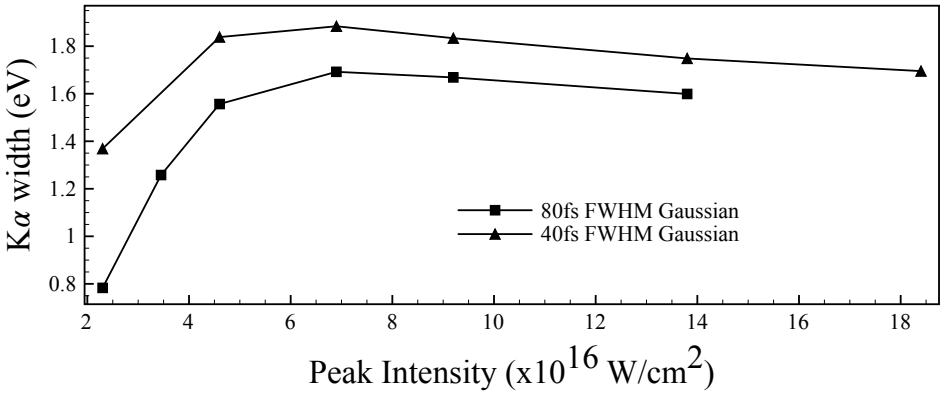

Figure 3.16: The simulated width of the main Kα as a function of intensity for pulse lengths of 40 fs and 80 fs when pumping with the FEL tuned to 1487 eV.

From this experimental data, a few observations can be made. Firstly, by pumping the system with FEL radiation at a photon energy below the K-edge of cold aluminium at 1560 eV, the line-widths of the main Kα peak are significantly greater than those when pumping with photon energies above the K-edge. In the below edge case the line-widths are around 2–4 eV, whereas they are about 0.7 eV for the above edge case. Secondly, when the pumping is resonant with the Kα (a photon energy of 1490 eV) the width of the Kα does not appear to change much with the pulse energy. Although when pumping slightly off-resonance (at a photon energy of 1495 eV) there does appear to be a linear trend of increasing line-width with pulse energy, and given that the photon energy of LCLS is not likely to be known to much better than 0.5%, it cannot be ruled out that there is some trend on resonance. However, as can also be seen in figure 3.17, when the photon energy is increased to be even further off-resonance (a photon energy of 1505 eV) there is a statistically significant increase in the line-width as a function of pulse energy, and the line-widths are significantly greater than those when pumping on resonance. It can also be seen that there is a

considerable spread in the line-widths in all the cases of pumping below the cold K-edge.

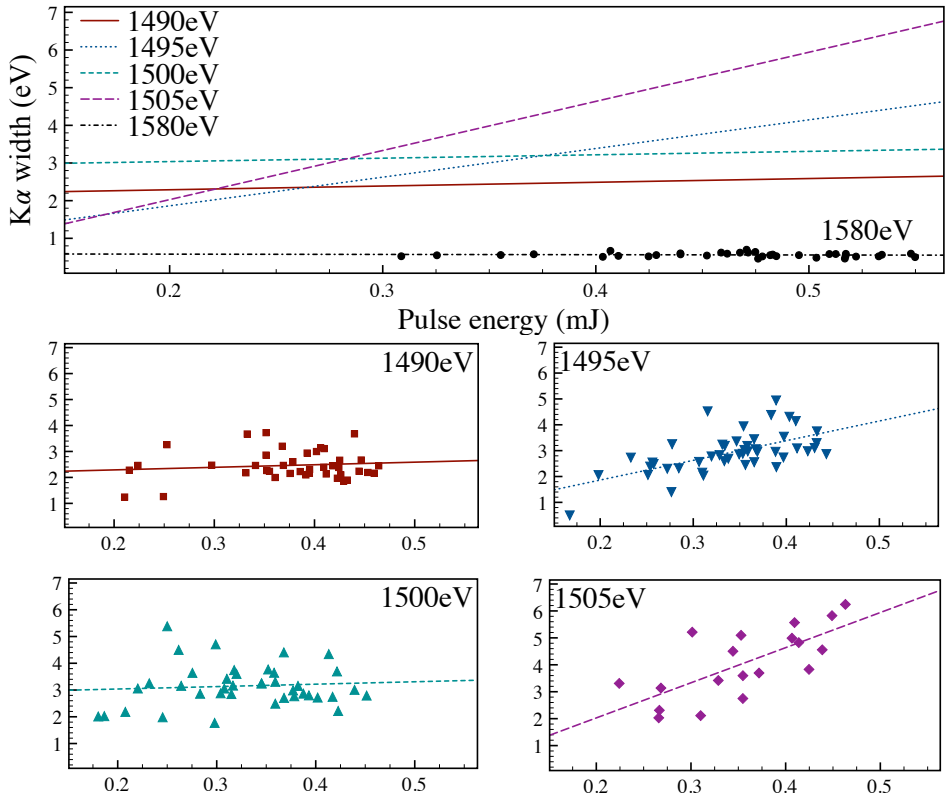

Figure 3.17: The Lorentzian part of the widths of Voigt fits to the first Kα peak of experimental single shots at the indicated photon energies, with linear fits to the data. The Gaussian part of the Voigt fit is taken to be 1.3 eV. The pulse energies are calculated to be those on target given the beamline transmission.

To compare with these other situations further simulations were performed with photon energies of 1495 eV, 1500 eV and 1507 eV. For all of these simulations a pulse length of 40 fs was used. The width of the Kα peak as a function of intensity is shown for each of these along with the on-resonance, 1487 eV, and above edge, 1580 eV, cases in figure 3.18.

By studying figures 3.17 and 3.18, some good qualitative agreement can

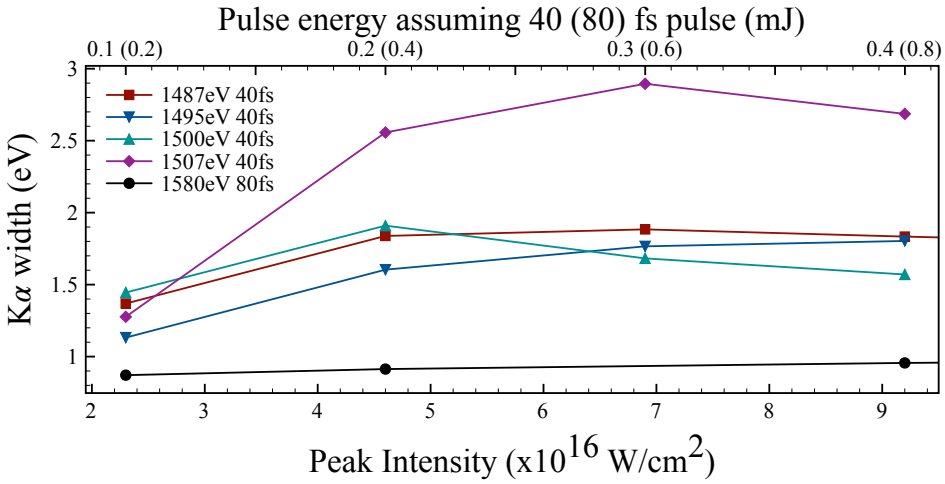

Figure 3.18: The simulated width of the first Kα peak as a function of peak FEL intensity (or equivalently pulse energy), when pumping with the FEL tuned to various photon energies.

be seen. Firstly, when pumping above the cold K-edge, both show little variation in the width of the Kα line. This is much as would be expected, as when pumping above the edge the main mechanism of absorption is K-shell photoionization, a process which is an order of magnitude more probable than L-shell photoionization. The production of K-shell holes, thus precedes the generation of the L-shell holes, leading to a smaller optical depth for the Kα emission at the time of greatest emission. Secondly, when pumping resonant with Kα photon energy, the line-widths are much greater due to the opacity broadening. The line-width when pumping at 1487 eV peaks at around 1.8 eV. This is lower than the 2.2 eV observed in the experiment, though there is quite a spread in the experimental values.

Perhaps the most interesting result is that in both the experiment and the simulations, when pumping about 15–20 eV above the resonance the line-width is noticeably increased. In the experimental case, at 1505 eV, the line width shows a clear trend of increasing with pulse energy, with typical values being around 4–5 eV at the highest intensities. In the simulations the

same trend is observed, though the large line-widths are not reproduced. In figure 3.18 it can be seen when pumping at 1507 eV the line-width peaks at close to 3 eV, in contrast to the 1.8 eV found when pumping on-resonance.

An explanation of this increased width is due to there being an increased build up of L-shell holes prior to the emission of Kα in the off-resonance case. The photons in this case are still below the energy of the K-edge, and so initially the main absorption mechanism is L-shell photoionization. As they are not resonant with the main Kα the process of generating K-shell holes is much less likely than in the resonant case, when there are single L-shell holes. However, as the photon energy is greater these photons are closer to the Kα transition of the charge state above, i.e. those with two holes in the L-shell. As higher charge states are now the main absorbers, they are also the main emitters, which is reflected in the emission spectra as seen in figure 1.4 where when pumping with a photon energy of 1507 eV there is clearly more emission from the next charge state up than the 'cold' Kα. In this situation it is possible to emit photons at the cold Kα energy, for example, if an ion with two L-shell holes is excited by the FEL, so that it has one K-shell hole and one L-shell hole and then collisionally recombines with a free electron filling the L-shell hole. However, due to the large number of ions with single L-shell holes, the optical depth will be large. To illustrate this, figure 3.19 shows how the ions with single L-shell holes are spatially distributed, when pumping with the FEL tuned to 1487 eV and 1507 eV, at the respective times of greatest emission of cold Kα. Both are pulses of 0.4 mJ with durations of 40 fs. The snapshot for the 1487 eV case is taken at 43 fs and the 1507 eV case is taken at 56 fs. It can be seen that the regions with the highest density of ions with single L-shell holes are much thicker in the non-resonant case than in the resonant case. Which leads to the

emission experiencing a greater optical depth before escape, and hence is broadened more. It is also worth noting that the time of greatest emission of the cold Kα is different, with the non-resonant case peaking later. This delay is due to the need for ions to have two, rather than one, L-shell holes before they can start significantly absorbing the FEL radiation through a resonant channel.

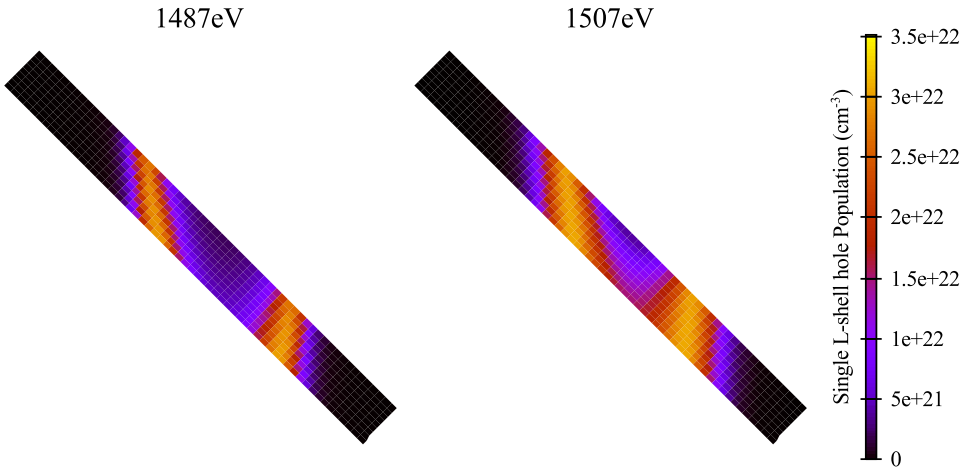

Figure 3.19: A temporal snapshot of the spatial distribution of density of ions with single L-shell holes for a 40 fs pulse (centred at $t = 40$ fs) containing 0.4 mJ of energy, with FEL photon energies of 1487 eV (left) and 1507 eV (right). These snapshots are taken at the time of greatest Kα emission, which is 43 fs when pumping with 1487 eV and 56 fs when pumping with 1507 eV.

3.6 Remarks

Through this chapter simulations have been presented of the opacity broadening of the main Kα emission peak from aluminium samples irradiated with intense FEL radiation at a variety of photon energies. The resultant simulations show good qualitative agreement with experimental data. It has been shown that the Kα line is broadened more by opacity when pumping with the FEL photon energy tuned to below the K-edge than when it is

tuned above the K-edge. The degree to which the broadening of the radiation occurs when pumped below the K-edge is dependent on the intensity, more so than the fluence. The positioning of the detector was found to effect the extent of the broadening due to the spatial distribution of the absorbing species, those ions with single L-shell holes, determining the absorption rate along the line of sight to the detector. As it is the population of ions with single L-shell holes which determine the amount of reabsorption it was found, through extending the treatment to photon energies that were not resonant with the cold Kα, that the opacity broadening is even greater when pumping at photon energies 15–20 eV above the resonant photon energy. This was found to be due to there being a greater build up of ions with single L-shell holes by the time of peak emission. Whilst the simulations are generally in agreement with the experimental results, when pumping below the K-edge the simulated line-widths are somewhat smaller than those found experimentally. A possible explanation for this would be that in all of the simulations presented a Gaussian temporal profile has been assumed, though as previously mentioned in section 3.4.2, the actual temporal profile may differ from this. Though given its random nature quantifying the exact effect is difficult and time-consuming with possibly little benefit.

CHAPTER 4

Saturable absorption of Hot Dense Aluminium

The content of this chapter will deal with results of measuring the transmission of an aluminium foil when exposed to intense FEL radiation. The experiment to which these results relate was performed after the experiment described in the previous chapter. Though the setup was broadly similar, the specifics of the setup were slightly different.

4.1 Experimental setup

The experiment was performed on the SXR beamline at the LCLS. The photon energy was tuned between 1540 eV, just below the K-edge of cold aluminium, and 1870 eV. For this experiment the electron bunch had a length

of 100 fs, which gives an approximate upper bound to the duration of the x-ray pulse. The photon energy of the x-ray pulse has a bandwidth of around 0.3%. As the x-ray pulse is generated through the SASE process, the number of photons in each pulse fluctuates by about 15% from shot to shot. However this can be accounted for as the energy of each pulse is measured using a gas monitor detector (GMD), which is positioned upstream of the focussing optics of the beamline. The energy of each pulse was approximately 2 mJ prior to transmission through the focussing mirrors. The x-ray beam was focused using Kirkpatrick-Baez mirrors. The distribution of intensities at the focal spot was diagnosed by analyzing the craters ablatively formed in a suitable material that strongly absorbs the LCLS radiation [62, 63]. The focal spot was found to have an effective area of 7 μm^2. The distribution of the intensities was well approximated by a super-Gaussian. The primary diagnostic for the work discussed here was a photodiode placed some way downstream of the target. The analysis of the signal from the diode will be discussed in the next section. A diagram of the setup is shown in figure 4.1.

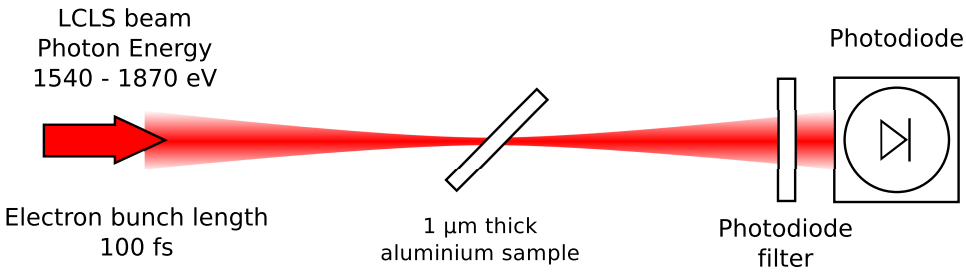

Figure 4.1: The LCLS beam is focussed onto an aluminium sample and the transmission recorded with a diode after the signal has been attenuated through a filter.

The irradiated sample was a 1 µm thick aluminium foil, which was oriented at 45°to the FEL beam. The foil was supported by a nickel mesh that covered around 10% of the rear surface area of the target. The foil

was moved to a fresh region for each shot, due to the damage caused to the sample by the FEL. However, the distance moved was not related to the spacing between the lines of the mesh and as such it would be expected that the true transmission would not be shown in around 10% of cases due to the x-ray beam hitting the supporting mesh.

4.2 Diode analysis

The primary diagnostic for the work described here was a photodiode placed behind the target. An example of the signal generated by the photodiode is shown in figure 4.2. From this it is clear that the raw signal has an offset for the zero signal level. The signal itself is also quite noisy. To calibrate the signal a number of runs were taken where the target was removed, these would give the signal for 100% transmission. During these runs the pulse energy was altered by using a gas attenuator located upstream of the GMD. The signal from the diode was integrated to give a value that was compared with the energy measurement of the pulse energy by the GMD. To remove the zero offset two approaches were tried. The first approach was to evaluate the offset on a shot to shot basis, as the first section of the trace represents zero signal, averaging this part of the trace should give the zero offset for that shot. The second approach was to use a single value for the zero offset, so assuming that the offset does not change shot to shot. The second approach, where a constant offset is assumed, gave less spread in the distribution when compared to the respective GMD values. Because of this result the constant offset was applied to all of the experimental signal results.

In order to prevent saturation of the diode, attenuating filters were placed in front of it. The energy content of a single pulse of the LCLS was such that the pulse needed to be attenuated by about 10^4. Specifi-

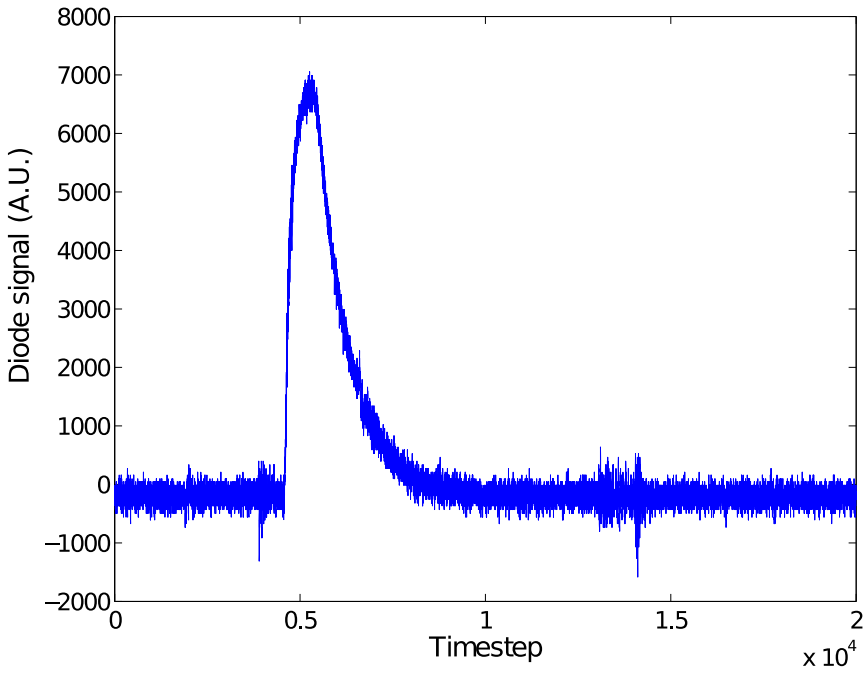

Figure 4.2: An example of the signal generated by the photodiode. Note there is a large amount of noise around the zero signal level and there is an offset to the zero level.

cally, the three filters used were a 72.5 µm carbon filter and two aluminium filters with thicknesses of 12.5 µm and 16.5 µm. These filters were used in the photon energy ranges 1540–1680 eV, 1670–1800 eV and 1800–1870 eV, respectively. Due to the high level of attenuation care must be taken in interpreting the photon-energy-dependent structure in the experimental data. Over the range of the photon energies used for the carbon filter, the amount of attenuation provided by the filter changes by an order of magnitude. This is further complicated in the case of the aluminium filters by the presence of EXAFS (x-ray absorption fine structure), where the absorption displays modulations. Whilst in terms of opacity these modulations are only a few percent, as the filters used are many absorption lengths thick, the transmission of the filter is modified by factors of 2 or so. In the analysis here the mass absorption coefficient of Barkyoumb and Smith [77] has been used to calculate the transmission of the aluminium filters. A comparison between the transmission of the aluminium filter using the EXAFS absorption rate and using the attenuation length found on the CXRO website are shown in figure 4.3.

A possible concern when calculating the transmission of the filters is the presence of harmonics in the x-ray beam, with the most common being the 3rd harmonic. These would cause issue as they would experience much less attenuation through the filters than the main pulse and thus alter the diode signal. However, as the mirrors transporting the x-ray beam to the end station have a sharp cutoff in transmission above photon energies of around 2.2 keV [78], they do not need to be worried about in this case.

The result of the calibration runs is shown in figure 4.4. The pulse energy on diode is the product of the GMD measurement of the pulse energy, the transmission of the filter in front of the diode and the beamline transmission

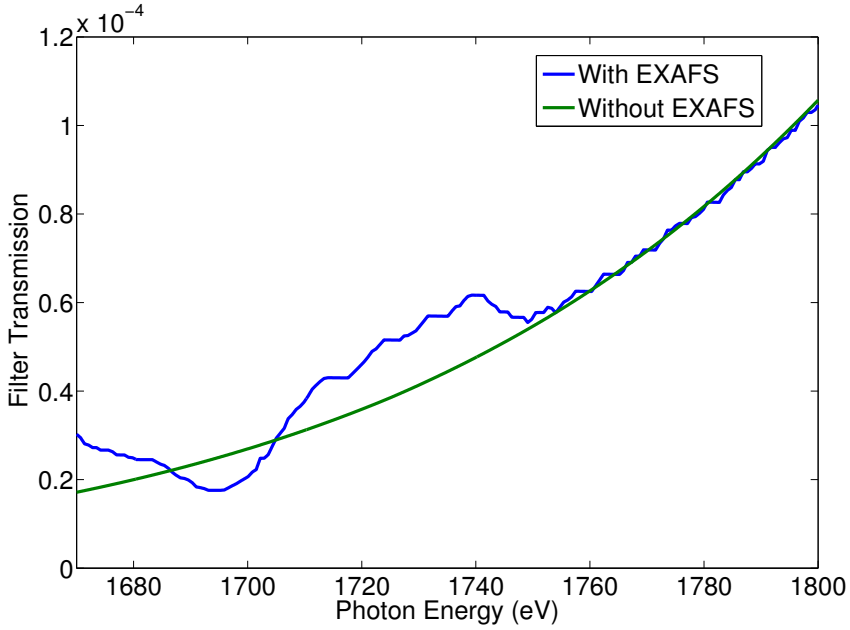

Figure 4.3: The two curves show the transmission of the 12.5 µm aluminium filter based on the absorption coefficients of CXRO [50] (green) and Barkyoumb and Smith [77] (blue), i.e. without and with considering the effects of EXAFS.

from Ref. [76]. The two colours of dots represent the two photon energies at which the calibration runs took place, 1480 eV (green) and 1557 eV (blue). The red line is a fit to the data and is used for converting the diode signal to the pulse energy on the diode in the experiment.

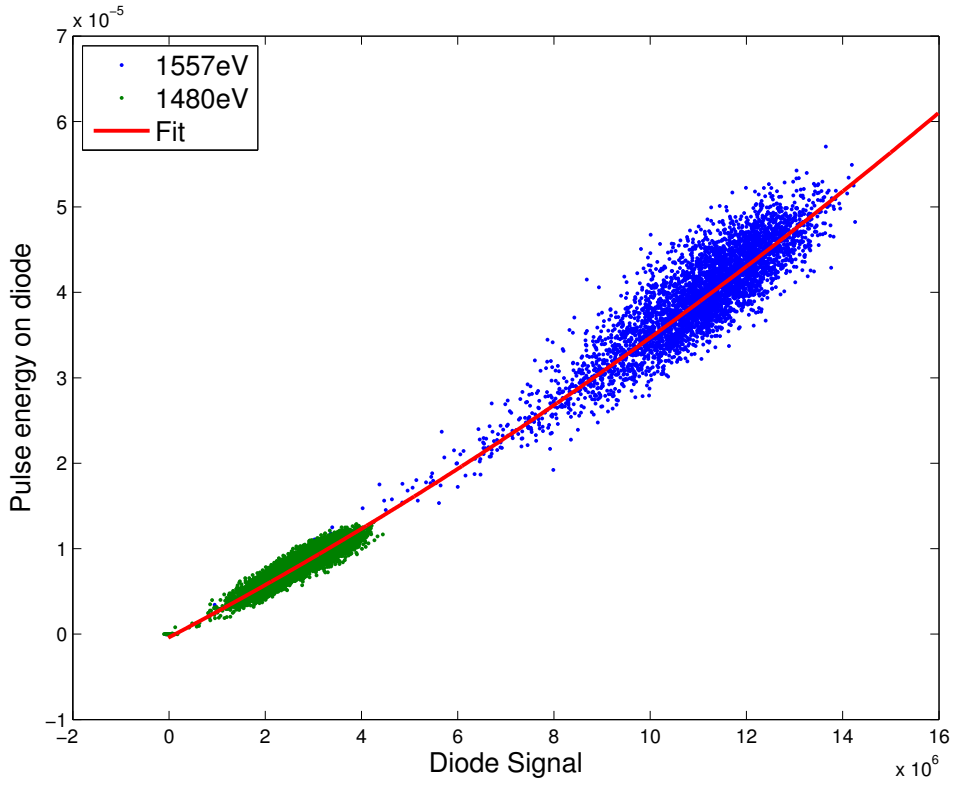

Figure 4.4: Data points from the diode calibration runs at photon energies of 1480 eV and 1557 eV, along with the fit to the data. There are 10,621 and 4,356 data points for each of the photon energies respectively

The calibration runs allowed for converting the diode signal to an equivalent GMD value, and thus give the transmission. Within this there was still a 5% fluctuation of the diode signal relative to that deduced from the GMD reading.

4.3 Modelling setup

To simulate the experiment the collisional-radiative code SCFLY was used. Simulations were performed with intensities ranging over 5 orders of magnitude. At each time the photon-energy dependent opacity is calculated and used to give the transmission at that time for a given intensity. The opacity will vary as the XFEL beam traverses the sample. To account for this the sample was split into four laminae, with the transmitted intensity from one layer used as the input intensity for the next lamina. The results of each intensity were added together according to the spatial distribution derived from the ablative measurements.

For the temporal structure a flattop pulse with a duration equal to the length of the electron beam was used. As transmission is achieved when the total number of photons in the pulse exceeds the number to strip the sample of electrons to the relevant charge state, the results are largely insensitive to changes in pulse duration and shape.

4.4 Experimental results

The experimental results are shown in figure 4.5 along with simulation results and the cold transmission curve from CXRO. The general trend of the experimental results is shown by the red line, this neglects those which are far from the trend, with those above the trend posited to be due to the FEL beam passing through partial windows or small holes in the target, and those below being due to the FEL beam hitting, or partially hitting, the supporting nickel mesh of the target.

When crossing the K-edge it might be expected that there would be a large drop in the transmission, as the cold absorption length at this photon

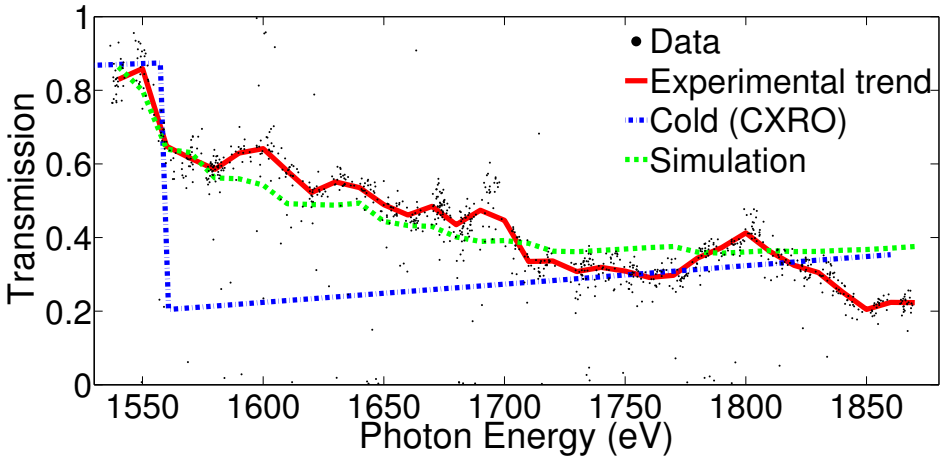

Figure 4.5: The transmission of a 1 µm thick aluminium sample oriented at 45°to the FEL beam. The red line shows the experimental trend, neglecting data points far from the majority. The green line is from the SCFLY simulations of the transmission, and the blue line shows the transmission as given by CXRO for the cold transmission.

energy shortens by about an order of magnitude. However, in the experiment the drop is not as severe as the cold case, a feature which is reflected in the simulations. This relatively high transmission occurs because although initially the absorption length will be short and a large number of photons will be absorbed, later in the pulse the population of those ionic species which can absorb a photon through K-shell photoionization will have diminished due to heating and ionization. This reduces the possible absorption mechanisms to primarily L-shell photoionization, which has a smaller cross section, giving a greater transmission.

In the cold case, above the edge, when the photon energy is increased the transmission gradually increases. However, the experiment and the simulations show the opposite trend with the transmission decreasing as the photon energy is increased. For an ion to become largely transparent to the FEL pulse, it will need to be ionized to such a degree that the K-edge energy

of the ion is greater than the photon energy of the incoming x-ray beam. As the photon energy is increased it is possible to ionize more and more charge states, so the ions will become transparent later in the pulse because they will need to undergo more ionization events before they become transparent. This leads to the transmission approaching the cold value at higher photon energies.

There is also some fine structure in the transmission in both the experiment and the simulations. When the K-edge energy of the next higher charge state is reached, a new absorption pathway is opened, which leads to the K-shell photoionization process continuing longer into the pulse, reducing the transmission. The position of the drops agrees roughly with the K-edges shown in the work of Ciricosta *et al.* [35]. However, due to the EXAFS effects that have been previously discussed, care should be taken in this interpretation especially above 1670 eV, where the aluminium filters were used. Although the EXAFS has been taken into account in the analysis, any inaccuracy in the amplitude as measured by Ref. [77], would result in some structure in the observed transmission.

4.5 Modelling results

Having seen that there is good agreement between the experimental and simulated results, it gives confidence that the simulations accurately reflect the physics of the experiment. Through the simulations the physical processes at work can be discerned. Figure 4.6 shows how the effective attenuation length changes for different fluences of the FEL radiation. As the attenuation length varies over the duration of the pulse, the effective attenuation length is calculated from the total amount transmitted during the pulse and assuming that the attenuation length was constant throughout the pulse.

From the figure a number of features can be seen. At low fluences the absorption length is that of cold aluminium, as would be expected due to the system being only lightly perturbed. Also at photon energies below the K-edge energy of cold aluminium the attenuation length is long for all the fluences simulated, due to the only absorption mechanism available being L-shell photoionization.

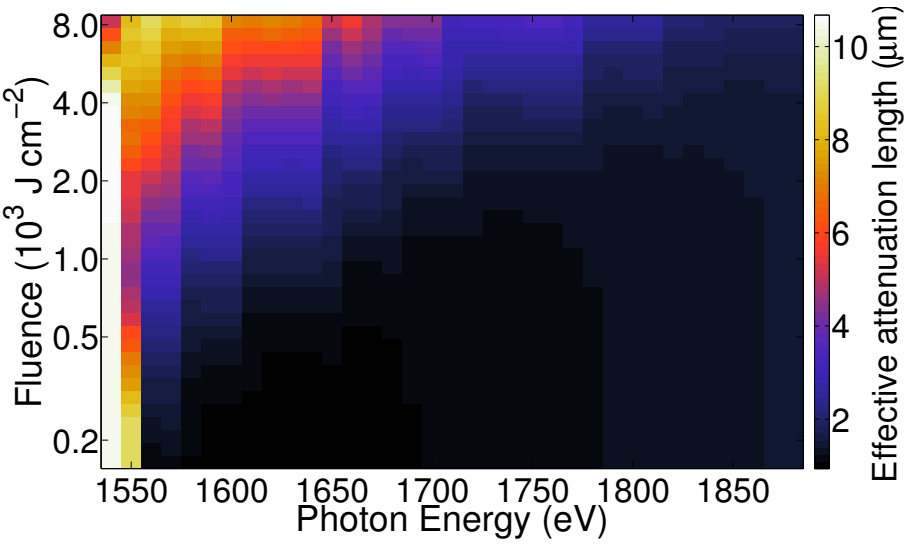

Figure 4.6: The effective attenuation length for an FEL pulse at a range of photon energies as a function of fluence. The actual attenuation length will vary over the duration of the pulse.

For a given photon energy, above the cold K-edge, there will be a fluence where the effective attenuation length will increase above the cold value. The fluence at which this induced transparency occurs increases with increasing photon energy, due to it being possible to K-shell photoionize more charge states at a higher photon energy. Also for the same reasons, at a given fluence the attenuation length (above the edge) decreases as the photon energy is increased.

Greater physical insight can be gained by examining the time dependent

behaviour of the system in the simulations. Figure 4.7 shows how the opacity of the sample changes in time when heated by the FEL tuned to a photon energy of 1670 eV. The contributions towards the total opacity by each of the charge states is shown as well as the charge state distribution itself. The simulations chosen for this figure have FEL intensities equal to the peak intensity and 20% of the peak intensity, as these show how the process is dependent on the intensity. As can be seen the opacity is dependent on which charge states are present, with the higher charge states being generated later in the pulse. The opacity due to each charge state tracks the proportion of ions in that charge state, due to the opacity being directly related to the population.

At an FEL photon energy of 1670 eV it is possible to ionize, through K-shell photoionization, all charge states up to and including 6+. At the start of the pulse the opacity is equal to the cold case, as would be expected as the sample is cold to start with. In the simulation with the intensity of 20% of the peak intensity the opacity remains approximately constant at the cold value for the first 30 fs, after which it starts to drop, whereas when pumping with the full intensity the drop in opacity is very rapid indeed. This delay in change of opacity is due to it taking time for the system to be ionized such that there are significant numbers of ions in charge states of 7+ and above. At lower photon energies the time for the opacity drop will decrease due to the charge state that needs to be achieved for transparency being lower and therefore populated earlier in the pulse. Equally, at higher photon energies the drop in opacity occurs later in the pulse as it is possible to ionize higher charge states, so it will be later in the pulse when the relevant (higher) charge states are populated.

In the two intensity cases shown in figure 4.7 the opacity asymptotes to

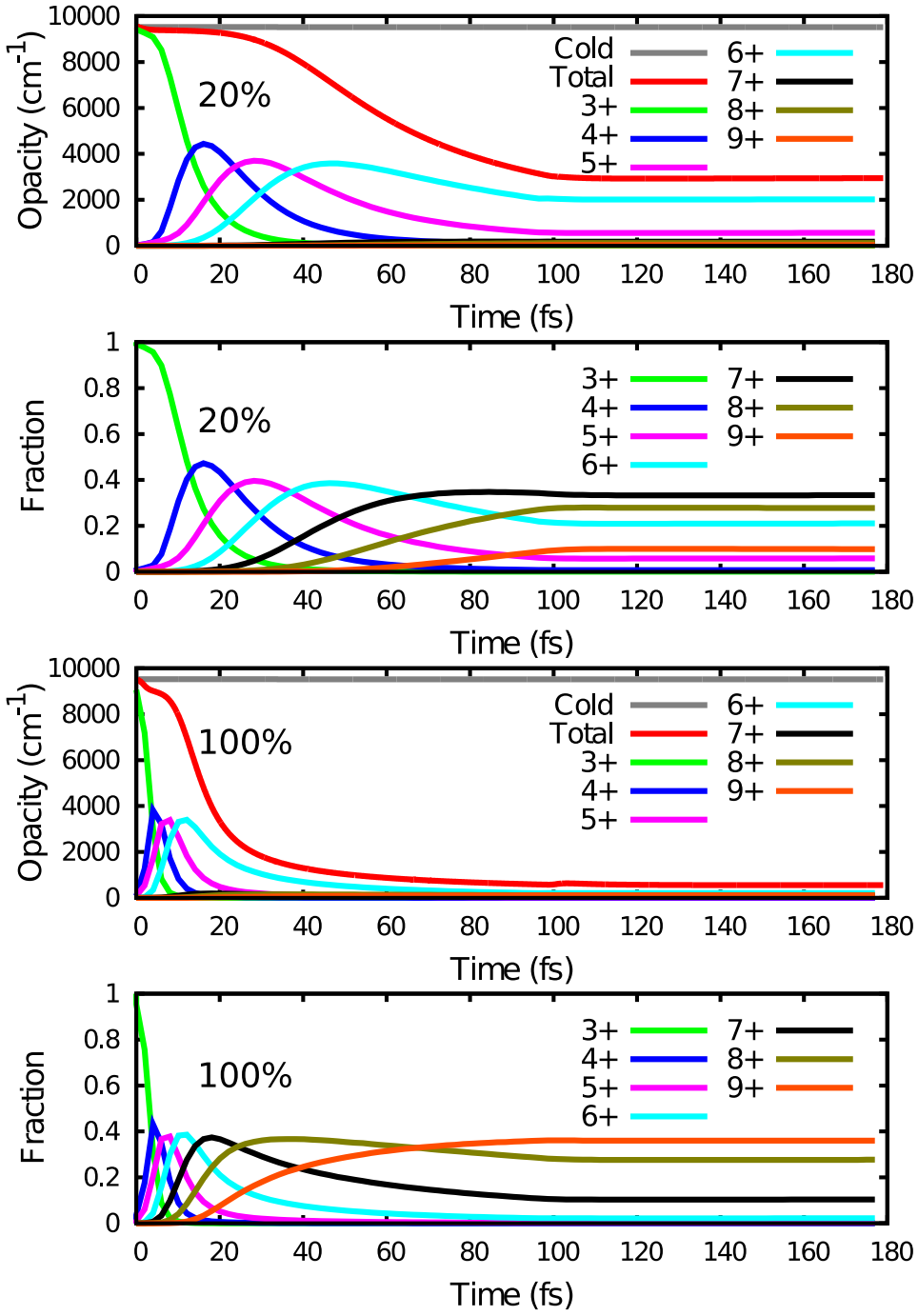

Figure 4.7: Time-dependent opacities, with contributions from individual charge states, and charge state distributions from simulations at a photon energy of 1670 eV at 20% of the peak intensity (top two panels) and the full peak intensity (bottom two panels). The FEL pulse is constant in intensity for the first 100 fs and is then turned off.

a value, though the reason is different in the two cases. In the peak intensity case after about 50 to 60 fs the opacity levels off due to the ions of charge state 6+ or below being burnt through in the early stages, meaning at the latter end of the pulse the only ions remaining are unable to absorb through K-shell photoionization. In contrast, in the 20% intensity case there are still significant numbers of 6+ ions in the sample at the end of the pulse and the opacity asymptotes due to the FEL being switched off at 100 fs. The value to which the opacity in the 20% case asymptotes is correspondingly higher than that of the peak intensity case.

4.6 Comparison with other experiments

The increase in transmission owing to a high incident x-ray fluence is an example of saturable absorption in the x-ray region of the spectrum. In this section comparisons will be drawn between the results of this experiment and the results of other experiments with similar phenomena observed.

Saturable absorption in aluminium has previously been observed in the XUV region with the FLASH FEL [79]. In this situation the FEL was tuned to just above the L-edge of aluminium so that it was only energetically possible to create single L-shell holes. When an electron was photoionized from the L-shell to the continuum, the L-shell hole has a lifetime of around 40 fs [80]. This rapid recombination process leaves the ion in its original state, which is in contrast to the situation described earlier in this chapter. Due to the recombination process, saturable absorption in the XUV case is achieved through the photoionization rate directly competing with the Auger recombination.

Previous experiments at the LCLS using atoms, molecules and clusters showed decreases in absorption with very short pulses [15, 19, 22]. In these

examples the number of highly charged ions was reduced for the shorter pulses. This reduced absorption was attributed to the lifetime of the inner shell vacancy generated by photoionization by the FEL radiation being of comparable duration to the pulse length of the FEL pulse.

These situations are different to the experiment described in this chapter, as in these other cases the reduction of absorption is due to having the absorbing processes competing with the recombinational processes. In the experiment of this chapter the K-shell hole lifetime is significantly less than the duration of the FEL pulse, and the saturation of absorption is due to the sample being heated such that the final ionization states have K-edges lying higher in energy than the FEL photon energy.

An experiment which is more comparable to the current work was performed on the Japanese FEL, SACLA [81]. In this experiment they tuned the FEL photon energy to 7.1 keV which is in the vicinity of the iron K-edge (7,113 eV). This was focussed to a $50 \times 50\,\mathrm{nm}^2$ spot using a two stage focussing system. The x-ray pulse had an energy of 20 µJ and a duration of 7 fs. This gave a maximum intensity of around $10^{20}\,\mathrm{W\,cm^{-2}}$. The beam was directed onto a 20 µm thick iron foil. A spectrometer placed behind the sample was used to measure the transmitted spectrum. By moving the sample along the beam axis they were able to change the spot size on target and thus change the intensity. In this manner they varied the intensity between $10^{15}\,\mathrm{W\,cm^{-2}}$ and the peak. By analysing the transmitted spectrum they found that at 7,130 eV the transmission of the peak intensity was 10 times that of the cold solid. They also found that at an intensity of $10^{19}\,\mathrm{W\,cm^{-2}}$ the transmission was 3 times that of the cold condition.

One of the main claims that they make is that from this change in transmission they can measure the lifetime of the K-shell hole, since the experi-

mental results do not match their simulations with the accepted value of the K-shell hole lifetime, but do fit simulations with a longer living K-shell hole. However, the change in transmission cannot be a measure of the lifetime due to the recombination process. When a K-shell hole is generated it will be filled through either Auger decay or radiative decay (the fluorescence yield of iron is 34% [64]). The K-shell hole lifetime according to ref. [82] is 500 as. If the ground state of iron were to replenish at this rate then the intensity at which the transmission starts to change from the cold value would be higher than the experimentally observed value. However, the decays do not leave the iron in its natural cold configuration. Instead the radiative decays would leave a hole in the L-shell, whilst the Auger decays would, typically, lead to two holes in the L-shell. Due to the reduced number of L-shell electrons, the K-shell electrons are more tightly bound, leading to an increased K-edge energy. Using the Los Alamos atomic codes [83] an estimate can be made as to the amount the K-edge energy will shift. For a single L-shell hole the K-edge energy will increase by 89 eV, whilst if there are two holes in the L-shell (owing to Auger decay) the K-edge energy is increased by 184 eV from the cold value. Given that the bandwidth of the FEL is around 40 eV it would not be possible to ionize an electron from the K-shell of atoms in these configurations. So the only way that this experiment could be a measure of the lifetime would be if these states with L-shell holes only existed for times much shorter than the K-shell holes. However, according to ref. [84] the L-shell holes have a lifetime of 2 fs so the experiment cannot measure the lifetime of the K-shell hole. To fully analyse the results would require self-consistent atomic-kinetics calculations to be performed, since they have very high intensities simply looking at the K-shell levels is not really enough.

In contrast, in the work presented in this chapter, self-consistent atomic-

kinetics simulations have been performed which do agree with the experimental results and the reason behind the onset of saturable absorption is observed and understood.

4.7 Ionization processes

Since the saturation in the experiment described in this chapter is achieved owing to ionization, it is important to understand which ionization processes are contributing and to what extent. While the primary interaction of the FEL with the sample is through the ejection of an electron from the K-shell to the continuum, the subsequent hole in the K-shell can be refilled. Most readily this is through Auger decay of L-shell electrons, where one L-shell electron will fill the K-shell hole, whilst another is promoted into the continuum with a large energy. The timescale of this Auger process is very fast when compared with the duration of the FEL pulse, in contrast to the XUV case. The energetic electrons promoted to the continuum through the photoionization and Auger processes will heat the free-electron gas. This thermal bath of electrons can itself cause ionization via electron-ion collisions.

As an example, figure 4.8 shows the rates of ionization of the 4+ ion by various processes, and how these rates change over the duration of the FEL pulse. The excited state population, i.e. those ions with a hole in the K-shell, is generated through the photoionization by the FEL of the charge state below, and thus its population peaks prior to the population of the ground state of the same charge state. Through the photoionization and subsequent Auger decay processes, the free electrons are heated as the x-ray pulse is absorbed. Consequently the collisional ionization rate increases such that, in this example, it is greater than the photoionization rate within the

first 10 fs and in about 30 fs exceeds the Auger decay rate of the excited state. It is interesting to note that these timescales are dependent on the intensity, and as such a shorter, more intense, pulse would lead to correspondingly reduced times. The dominance of the collisional ionization rate over the other ionization rates indicates that at these high intensities the final charge state distribution is determined by collisional processes. Since the collisional processes are determined by the temperature of the free electrons, the final charge state distribution and therefore whether saturable absorption occurs is ultimately determined by how much energy can be absorbed by the sample during the pulse.

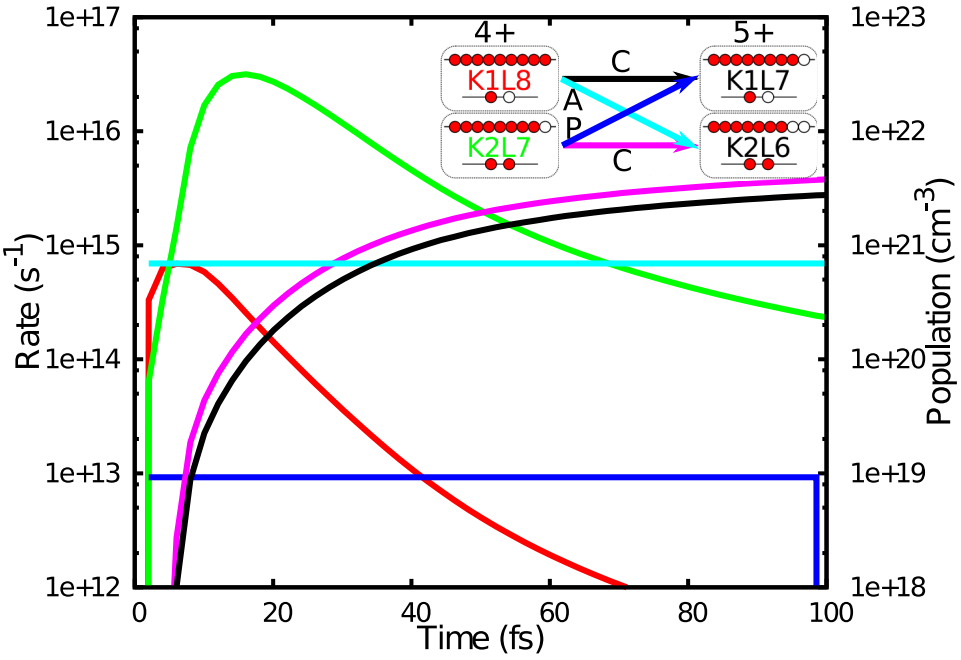

Figure 4.8: The rates of ionization of the 4+ charge state through photoionization (P), Auger (A) and collisional (C) processes. Also shown are the populations of the two super-configurations of the 4+ charge state.

4.8 Possible application to MAD

In the publication [2] it was posited that the photon energy dependent transmission as shown in figure 4.5 has possible application to the MAD method of phase determination, this statement will be further explored in this section.

MAD, or Multiwavelength Anomalous Diffraction, is a method for the solving the 'phase problem' in diffraction. Since diffraction patterns are formed from the intensity they will intrinsically lose the information held within the phase of the electric field, many possible solutions to the phase problem have been used over the years.

The MAD approach is based on the fact that in the vicinity of an atomic edge the atomic scattering factor is modified in a frequency dependent manner. As such, resonant elastic scattering causes the scattering factor to take the form $f(\mathbf{Q}, E) = f^0(\mathbf{Q}) + f'(E) + if''(E)$, where $\mathbf{Q}$ is the photon momentum transfer and E is the photon energy. The imaginary part of the scattering factor, $f''(E)$, is intrinsically linked to the absorption rate.

Given the transmission, T, (which is a function of photon energy, E), the density, $\rho(\mathrm{g\,cm^{-3}})$, and the thickness, $x(\mathrm{cm})$, the imaginary part of the scattering factor can be calculated.

$$T(E) = e^{-\mu(E)\rho x} \tag{4.1}$$

$$\mu(E) = -\frac{\ln(T(E))}{\rho x} \tag{4.2}$$

$$\mu_a(E) = \frac{m_a}{N_A}\left(-\frac{\ln(T(E))}{\rho x}\right) \tag{4.3}$$

where μ is the mass absorption coefficient, μ_a is the cross-section per atom, m_a is the atomic mass and N_A is Avogadro's number. From the paper

by Henke *et al.* [85], this quantity is related to the imaginary part of the scattering factor

$$f''(E) = \frac{\pi}{2} C E \mu_a(E) \tag{4.4}$$

Thus

$$f''(E) = \frac{\pi}{2} C E \frac{m_a}{N_A} \left(-\frac{\ln(T(E))}{\rho x} \right) \tag{4.5}$$

where $C = (\pi r_0 hc)^{-1} = 0.9111\,(\mathrm{eV\,\AA}^2)^{-1}$. In the case of aluminium, where $m_a = 26.98$ and $\rho = 2.69\,\mathrm{g\,cm}^{-3}$, this gives the relation,

$$f''(E) = (-2.375 \times 10^{-7}) \frac{E \ln(T)}{x} \tag{4.6}$$

where E is measured in eV and x is in cm. The real part of the anomalous scattering is related to the imaginary part by,

$$f'(E) = \frac{2}{\pi} \int_0^\infty \frac{\epsilon f''(\epsilon) \partial \epsilon}{E^2 - \epsilon^2} \tag{4.7}$$

Using these relations it is possible to derive f' and f'' from a transmission experiment, or through a similar relation with a fluorescence measurement.

If a sample is made of a species that anomalously diffracts and the rest of the system diffracts normally the resultant intensity diffracted, in the Karle-Hendrickson derivation, is given by

$$\begin{aligned} I(\mathbf{Q}) \propto |F(\mathbf{Q})|^2 = |F_T^0|^2 + a(E)|F_A^0|^2 \\ + b(E)|F_T^0||F_A^0| \cos(\phi_T^0 - \phi_A^0) \\ + c(E)|F_T^0||F_A^0| \sin(\phi_T^0 - \phi_A^0). \end{aligned} \tag{4.8}$$

In this form $F_T^0 = |F_T^0| \exp(i\phi_T^0)$ is the total scattering factor from all atoms considering only the normal term (f^0), and $F_A^0 = |F_A^0| \exp(i\phi_A^0)$ is the normal scattering component from the anomalous scatterers. So from the previous equation,

$$a(E) = \left(\frac{f'^2 + f''^2}{{f^0}^2} \right), \tag{4.9}$$

$$b(E) = 2 \left(\frac{f'}{f^0} \right), \tag{4.10}$$

$$c(E) = 2 \left(\frac{f''}{f^0} \right). \tag{4.11}$$

All the quantities on the right side of these equations are quantities that are either known, can be found experimentally or can be calculated. Thus, the only unknowns of equation 4.8 are $|F_T^0|, |F_A^0|, \text{and}(\phi_T^0 - \phi_A^0)$, so by measuring the diffraction from some reflections at a couple of frequencies the position of the anomalous scatterers can be deduced and then the full structure determined [86].

Whilst this kind of method has been used in the past with 3rd generation light sources [87, 88], it is not immediately obvious that the MAD method is applicable to the high intensities of XFELs, where multiple ionization events will modify the scattering factor in a time-dependent manner. However, work performed by Son and colleagues [89] has shown that there are analogous relations to the MAD coefficients that can be derived in the high intensity case. Since the anomalous scatterers (i.e. the heavy atoms) will undergo ionization events, which will alter their normal scattering as well as anomalous scattering, it is not appropriate to follow the previous treatment of separating the normal and anomalous scattering parts. Instead the scattered intensity is deduced by separating the contributions from those that have no anomalous scattering and the full contribution from those that do.

The molecular form factor for those atoms that scatter normally is $F_P^0(\mathbf{Q}) = |F_P^0(\mathbf{Q})|e^{i\phi_P^0(\mathbf{Q})}$. If we define the normal scattering of undamaged neutral heavy atoms as,

$$F_H^0(\mathbf{Q}) = |F_H^0(\mathbf{Q})|e^{i\phi_H^0(\mathbf{Q})} = f_H^0(\mathbf{Q})\sum_{j=1}^{N_H} e^{i\mathbf{Q}\cdot\mathbf{R}_j}, \tag{4.12}$$

where $f_H^0(\mathbf{Q})$ is the atomic scattering factor for a neutral atom in the ground state configuration and $\mathbf{R}_j$ is the position of the j-th heavy atom.

This leads to the scattered intensity being proportional to

$$\begin{aligned}|F(\mathbf{Q})|^2 = |F_P^0(\mathbf{Q})|^2 + \tilde{a}(\mathbf{Q},E))|F_H^0(\mathbf{Q})|^2 \\ +b(\mathbf{Q},E)\,|F_P^0(\mathbf{Q})||F_H^0(\mathbf{Q})|\cos(\phi_P^0(\mathbf{Q}) - \phi_H^0(\mathbf{Q})) \\ +c(\mathbf{Q},E)\,|F_P^0(\mathbf{Q})||F_H^0(\mathbf{Q})|\sin(\phi_P^0(\mathbf{Q}) - \phi_H^0(\mathbf{Q})) \\ +N_H|f_H^0(\mathbf{Q})|^2\left\{a(\mathbf{Q},E) - \tilde{a}(\mathbf{Q},E)\right\},\end{aligned} \tag{4.13}$$

where the quantities $a(\mathbf{Q},E)$, $b(\mathbf{Q},E)$, $c(\mathbf{Q},E)$ and $\tilde{a}(\mathbf{Q},E)$ are defined by

$$a(\mathbf{Q},E) = \frac{1}{\left\{f_H^0(\mathbf{Q})\right\}^2}\sum_{I_H}\bar{P}_{I_H}|f_{I_H}(\mathbf{Q},E)|^2, \tag{4.14}$$

$$b(\mathbf{Q},E) = \frac{2}{f_H^0(\mathbf{Q})}\sum_{I_H}\bar{P}_{I_H}\left\{f_{I_H}^0(\mathbf{Q}) + f'_{I_H}(E)\right\}, \tag{4.15}$$

$$c(\mathbf{Q},E) = \frac{2}{f_H^0(\mathbf{Q})}\sum_{I_H}\bar{P}_{I_H}f''_{I_H}(E), \tag{4.16}$$

$$\tilde{a}(\mathbf{Q},E) = \frac{1}{\left\{f_H^0(\mathbf{Q})\right\}^2}\int_{-\infty}^{\infty} dtg(t)|\tilde{f}_{I_H}(\mathbf{Q},E,t)|^2 \tag{4.17}$$

Here I_H denotes the electronic configurations of the heavy atom and P_{I_H} is the population of a given configuration with $g(t)$ the normalized pulse shape of the FEL pulse, hence $\bar{P}_{I_H} = \int_{-\infty}^{\infty} dtg(t)P_{I_H}$ is the pulse shape

weighted configuration population average. In the coefficient $\tilde{a}$, the quantity $\tilde{f}_{I_H}(\mathbf{Q}, E, t)$ is defined as $\tilde{f}_{I_H}(\mathbf{Q}, E, t) = \sum_{I_H} P_{I_H}(t) f_{I_H}(\mathbf{Q}, E)$, which is required due to the different heavy atoms being ionized to different extents at specific times.

Through measuring the transmission of the high intensity FEL pulse and using the relations derived earlier in this section the quantity $\sum_{I_H} \bar{P}_{I_H} f''_{I_H}(E)$ can be found, which is relevant to the c coefficient and is denoted $\tilde{c}(\mathbf{Q}, E)$ [90]. From this it is also possible to get the related quantity $\sum_{I_H} \bar{P}_{I_H} f'_{I_H}(E)$. These quantities for the cold and simulated hot cases of FEL heated aluminium are shown in figure 4.9, where the hot case has been extended using the cold values outside of the experimental range.

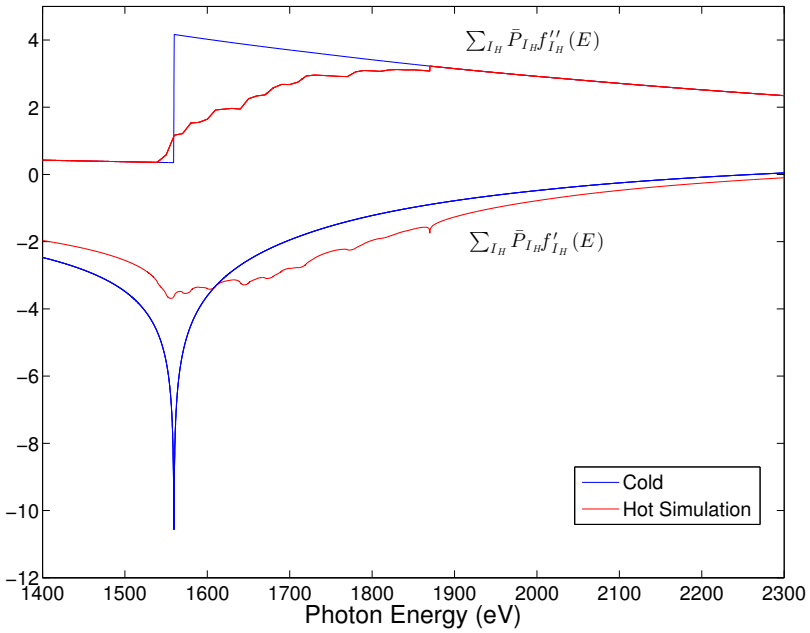

Figure 4.9: The pulse averaged anomalous scattering factors for cold aluminium (using CXRO website) and the FEL heated aluminium from the simulations of earlier in the chapter.

Though measuring these quantities for aluminium does not have imme-

diate implications for MAD (since heavier atoms are typically used), the fact that it is possible to well simulate the effects of the ionization on the absorption is encouraging.

CHAPTER 5

Split and delay transmission studies of Hot Dense Aluminium

In the previous chapter the transmission of an FEL-heated piece of aluminium was determined through looking at the signal from a diode positioned behind the target and comparing this value with the energy of the pulse prior to transmission through the sample. This method successfully determined how much of the initial pulse had been absorbed by the sample and was in good agreement with the simulated results. However, this method is fundamentally limited since it can only determine the time integrated transmission of the FEL pulse, and so the time-dependent evolution of the system cannot be determined experimentally, but assumed from the simulation work (which however, does give accurate results for the time-integrated data).

To measure time-dependent phenomena it is useful to set up some form of split and delay system. Within this some of the energy of the pulse is split off from the main pulse and delayed with respect to the main pulse so that evolutions in the behaviour can be observed with this delayed pulse. Through varying the delay of the probe with respect to the pump the full time evolution can be derived, however this is reliant on the process being reproducible, which with the random temporal structure of FEL pulses this may not be true.

5.1 Diffraction based split and delay

A method of generating a split and delay system at the high photon energies at LCLS has been developed by Christian David and team [91]. This method allows for many delays to be measured from the same FEL shot, potentially giving the time evolution on a shot by shot basis. The system is based on diffraction gratings, and shown in schematic form in figure 5.1. A beam splitter grating of different separations will diffract a small fraction of the pulse into a fan of beams. A second set of gratings halfway between the interaction point and the splitting gratings are used to redirect the fan of beams such that they will impinge on the target at the same position as the undiffracted beam.

Some of the beams will be diffracted by greater amounts, leading to the path length for these pulses being longer and so they will arrive at a later time. The probe beams are directed in different directions to one another and the pump beam, and so after the sample they will diverge from one another and be separately diagnosed.

In the experiment performed by David *et al.* [91], they used the split and delay system to examine how the diffraction intensity changed as a

function of time after a strong FEL pulse. The experiment was setup as in figure 5.1, with a Bismuth crystal as the sample. The sample was oriented such that the $< 111 >$ plane would satisfy the Bragg condition for all of the probe beams. The experiment involved exciting the sample with the main FEL pulse and through observing the diffraction from the probe beams the evolution of the diffraction intensity could be derived. When the pump pulse was greater than the damage threshold for Bismuth the diffraction signal from the probe beams died out with a decay time of about 50–70 fs, which is longer than the nominal pulse length that they used of 40 fs. The expected result was that the reflection would diminish with time after the initial FEL pulse, as the level of disorder in the system would increase, which was confirmed by the experiment.

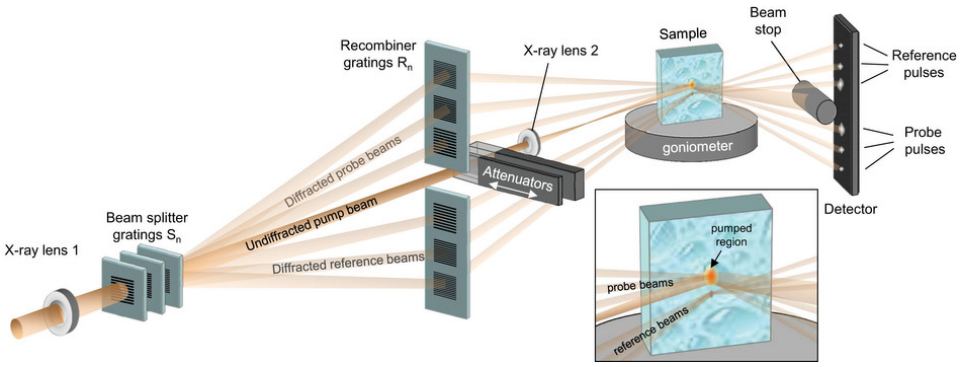

Figure 5.1: Split and delay setup used by C. David and team. The FEL beam has a small proportion of the energy in the pulse diffracted into a fan, the diffracted beams are recombined with the main pulse at the target. Image taken from C. David *et al.* Sci. Rep. **5**, 7644 [91]

5.2 Description of model

If this split-and-delay system is used in a transmission geometry, results akin to those discussed in the previous chapter might be achieved. To investigate what these results may look like, and what could potentially be learned from

them, a series of simulations were performed.

The system that was modelled was one of a 1 µm thick aluminium sample positioned such that the FEL beam was normal to the surface. For the simulations the sample was split into ten 100 nm layers with the radiation transmitted through each layer used as the input radiation for the next layer. Using the time dependent opacities generated by these simulations, probe beams are propagated through the FEL excited sample. Each of the probe beams have the same temporal and spectral profiles as the original exciting pulse. The probe beams are temporally displaced from one another by 10 fs.

The transmitted pulses are temporally and spectrally integrated to give a spatially dependent transmitted fluence. By dividing this fluence by the input fluence a spatially dependent transmission for each of the probe pulses can be derived.

5.3 Results

The simulation results shown in figure 5.2 are the transmissions through 20 µm by 20 µm square samples when pumped at different photon energies with probe beams at varying delay. These results use a flattop temporal shape with a duration of 100 fs, the pump beam has a total energy of 0.8 mJ. The spatial distribution of the pump beam is the same as the experimental distribution of the previous chapter (i.e. a 7 μm^2 spot). The probe beams are assumed to be sufficiently weak as to not effect the sample and so the calculation of the opacities using SCFLY is performed with only the pump pulse.

The transmission at the focal spot in all cases is the greatest, as might be expected from the results of the previous chapter. At the lowest intensities the transmission is roughly constant for all delays and increases as

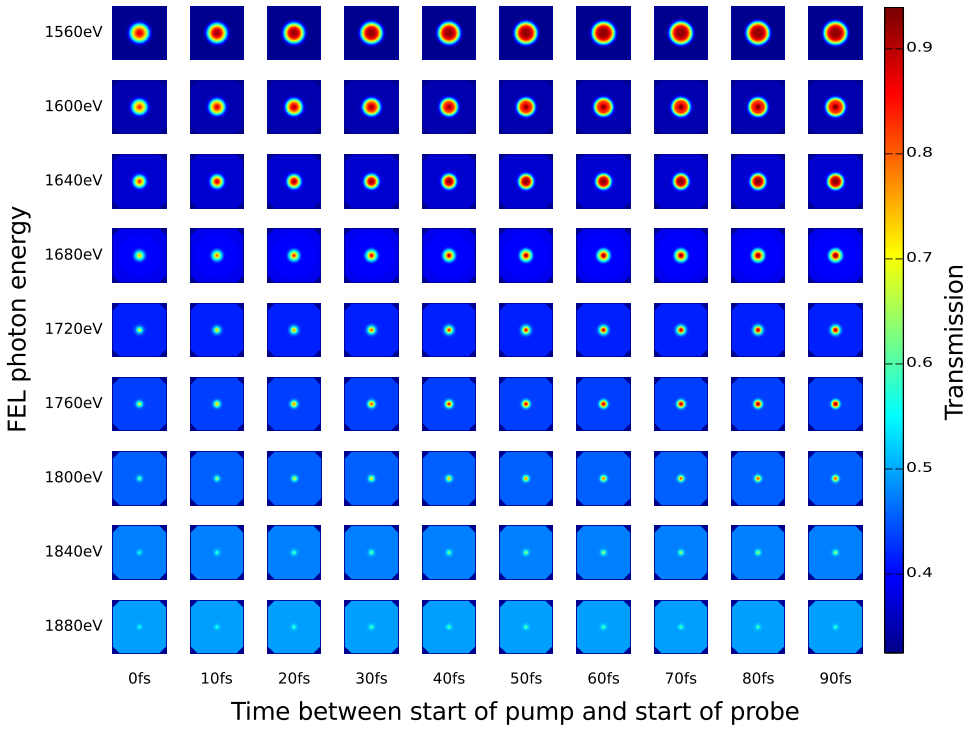

Figure 5.2: The transmission of 20 µm squares as diagnosed by probe beams at different delays relative to the pump pulse. The pump and probe beams are all temporally flattop pulse with a duration of 100 fs. The photon energy of the pump beam and probe beams are the same as each other.

the photon energy is increased, in line with the cold transmission curve. In general at later probe times more of the radiation is transmitted. The attenuation decreases over the duration of the pump pulse, and so consequently the later probe pulses will experience less of the relatively high attenuation of the early times.

More information can be gleaned by taking the difference between two sequential pulses, and so indicating how the transmission is changing in time, as shown in figure 5.3.

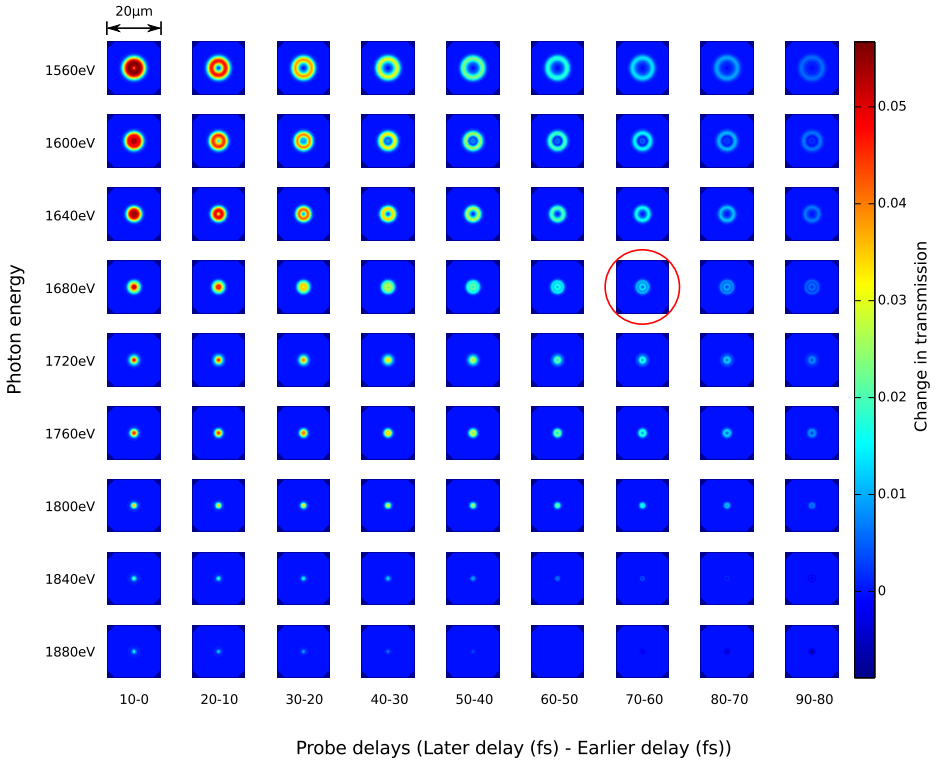

Figure 5.3: The difference in transmission of two sequential probe pulses. The circled example is shown in a larger form in figure 5.4.

At later times the difference between sequential pulses at the centre of the pulse is almost zero, implying that the transmission has reached a steady value at a reasonably early time. Further out from the centre the

transmission has not reached a steady value so is still changing.

By using a temporally flat pulse the results shown in figure 5.3 are the difference between the transmission of the first 10 fs of the earlier probe beam and the final 10 fs of the latter probe beam. This is due to the rest of the pulse being common between the two pulses and so cancels out when one is subtracted from the other.

One of the more interesting features of the transmission differences is that in some cases there appears to be two rings of larger changes in transmission. A closer examination of the difference map for pumping at a photon energy of 1680 eV with probes with delays of 60 fs and 70 fs shows essentially five regions (this is shown in larger form in figure 5.4). The central region has very little change, this is surrounded by a ring of large change in transmission, which is followed in turn by a ring of lesser change in transmission. Further out from this is another ring of large change in transmission, the regions furthest from the centre of the FEL show very little change in transmission.

The cases of the central region and the very outer region are the easiest to explain. In the centre of the FEL focus the transmission doesn't change as saturation of the absorption has occurred early in the pulse, and so the attenuation experienced by both of the probe beams is essentially the same. The far outer region experiences a pumping FEL intensity that is insufficient to induce saturable absorption, so there isn't a change in transmission over the duration of the pulse.

The other regions are experiencing an FEL intensity that will induce a change in opacity, however they have not absorbed sufficient energy for the absorption to be saturated. In essence the appearance of the rings is due to the absorption length changing between the start and the end of the probe pulses. The reason behind there being multiple rings is caused by the way

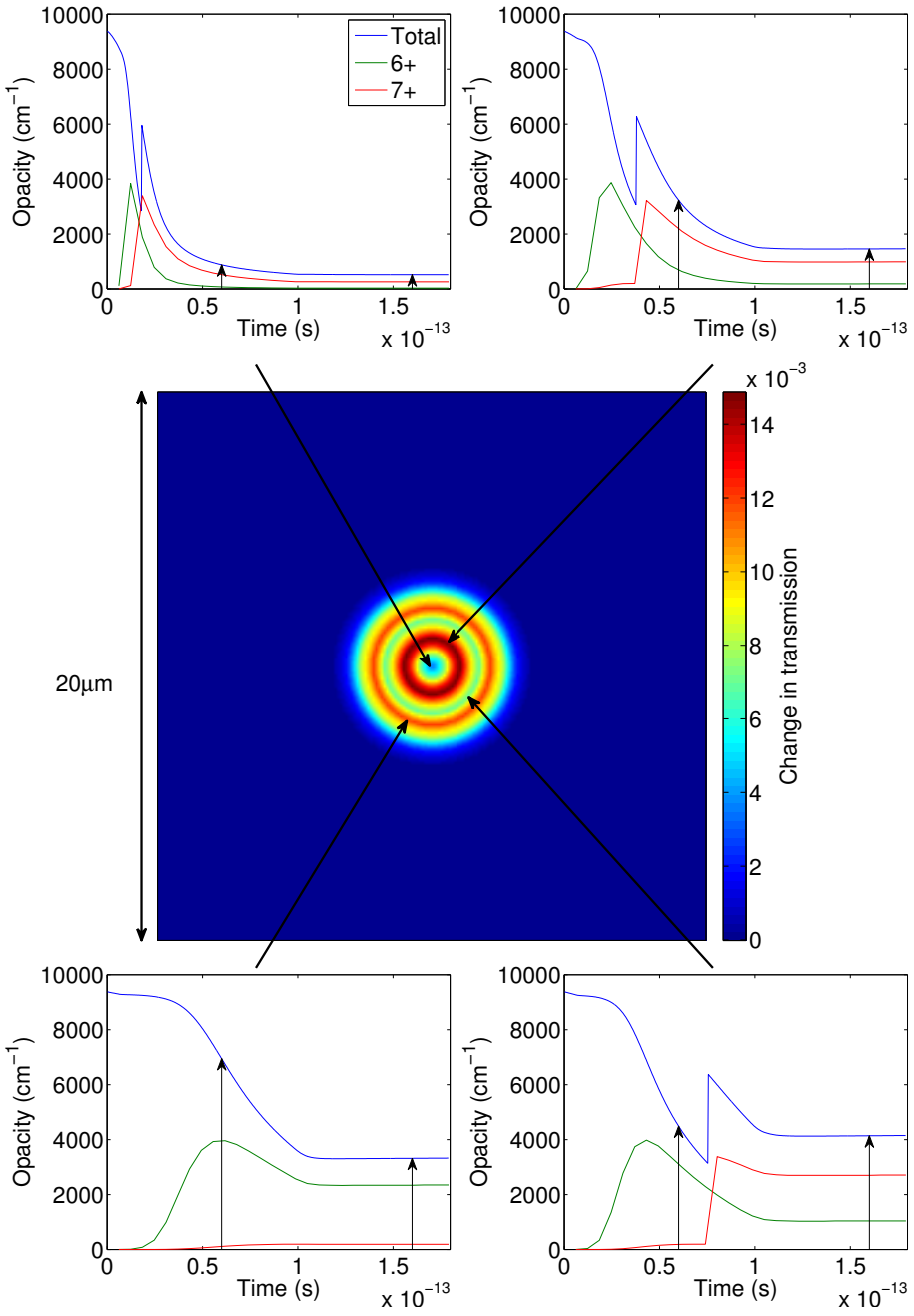

Figure 5.4: The time dependent opacities, with contributions from the 6+ and 7+ charge states, of the sample at different intensities. The intensities are chosen to reflect the different regions of change of transmission between probe delayed by 60 fs and 70 fs (shown in the centre). Clockwise from the top left the intensities are 100%, 37%, 20% and 14% of the peak intensity. The arrows indicate the opacity at the start and end of the first probe pulse.

that the ionization potential depression is treated in the code.

In the version of SCFLY used for these simulations the IPD model of Ecker and Kröll is used. As the sample absorbs more of the energy from the FEL the electron density increases, leading to an increase of the IPD. As such the K-edge energy will decrease, this is the origin of the multiple rings. In the example chosen for figure 5.4, the photon energy of 1680 eV is less than the initial K-edge for 7+ ions, however by the end of the pulse in the most intense regions the photon energy is greater than the K-edge energy for the 7+ ions.

The ring closest to the centre in figure 5.4 has experienced an intensity such that the 7+ can be ionized by the central photon energy of the FEL, however the intensity is still low enough that the absorption has not saturated by the time of the start of the probe pulse, leading to a change in the transmission over the duration of the probe pulse.

The outer ring of larger change is at a position where by the time of the end of the later probe pulse there has not been enough energy absorbed from the FEL for the K-edge energy of the 7+ ions to be less than the photon energy of the FEL. As such the change in transmission is due to the reduction of absorption due to the 6+ ions.

The ring of lesser change in transmission occurs at the intensity where the 7+ ions are starting to absorb throughout the depth of the sample. The total transmission of the sample at later stages of the pump pulse remains approximately constant. At the front the higher charge state can absorb quite strongly, leading to little transmission, whilst in the rear of the sample these ions are not able to absorb through K-shell photoionization, and so transmit more. At slightly later times there will be less of the higher charge state at the front, reducing the absorption, but the rear will be excited to

such a state that the higher charge state ions can absorb the FEL radiation strongly.

These kinds of results should allow for further information to be obtained about the IPD. For example, if the IPD is fixed for each charge state then rather than there being two rings, as in certain cases in figure 5.3 (e.g. the case shown in figure 5.4), there would only ever be one ring, because there would not be a transition between a certain charge state becoming strongly absorbing of the FEL radiation.

As mentioned earlier, when using a flattop pulse, the differences shown in figure 5.3 are due to the difference between the transmission for the time between the first probe pulse starting and the second probe pulse starting and the transmission between the first pulse ending and the second pulse ending. Using this and the assumption that the transmission will not change after the end of the pump pulse, it is possible to get the full temporal evolution of the transmission. The final probe pulse is delayed such that it has no overlap with the pump pulse, giving a final value for the transmission, and from this the rest of the time evolution can be derived by using the differences and iterating backwards in time.

The results of iterating backwards from the simulated probe beam transmissions are shown in figure 5.5 as circles, along with the transmission at each time from using each of the time dependent opacities of the various layers of the sample. The two results are in good agreement, and this suggests that it may be possible to derive the full time dependence of the transmission from the transmission of the probe pulses.

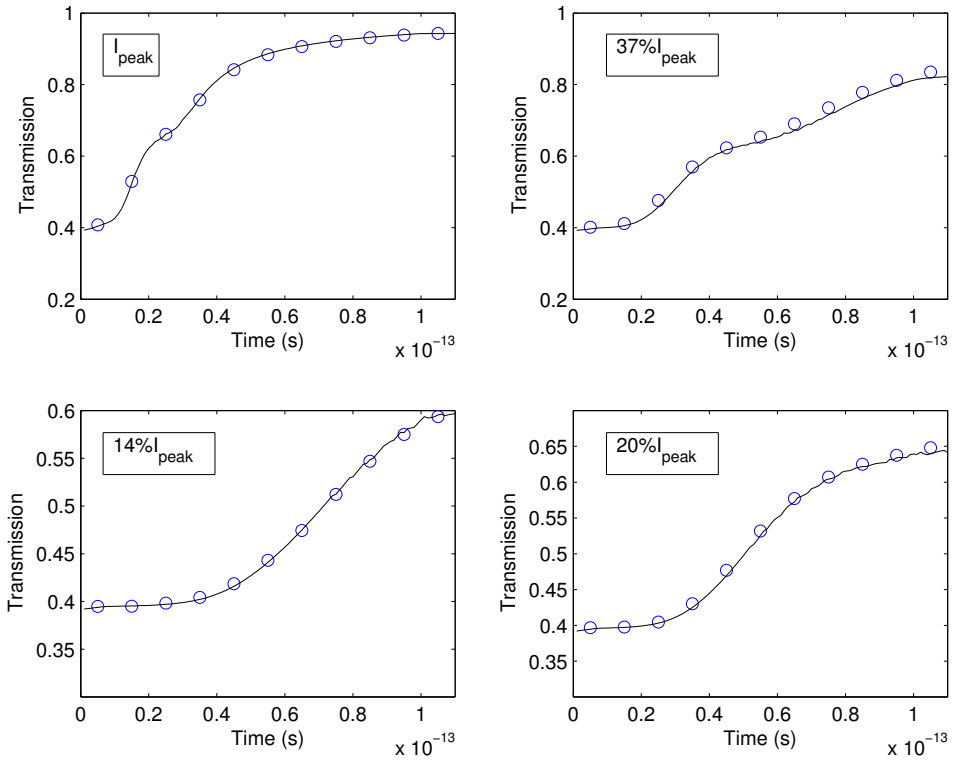

Figure 5.5: The simulated transmission as a function of time for various intensities (solid lines), along with those derived from the transmission of the probe pulses.

5.4 Importance of pulse shape

The work so far in this chapter has used a flattop temporal profile, which may not be the true temporal shape of the x-ray pulse. The flattop shape is particularly useful in these types of measurements, as taking the difference between two successive probe pulses leads to the majority of the transmission cancelling out. In addition the regions which don't cancel out are quite localized temporally and separated by almost the duration of the pulse. Due to the combination of these properties iterating backwards, as in figure 5.5, is effective.

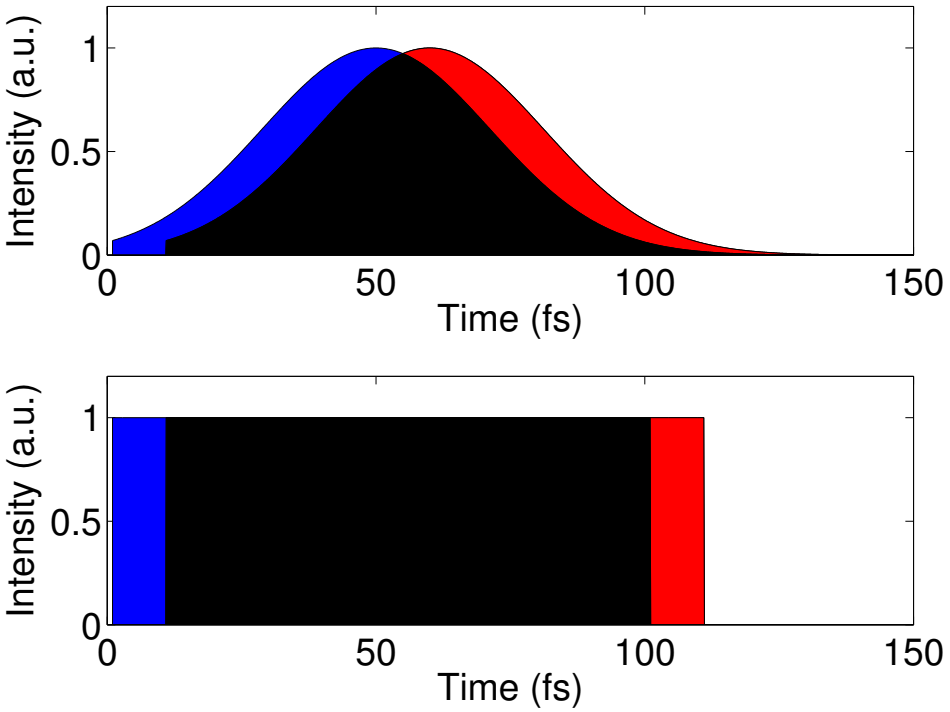

Figure 5.6: Comparison of flattop and Gaussian probe pulses. If the transmission of two probe pulses separated by 10 fs is subtracted from one another then the result is due to the contributions of the input fluences coloured in blue (from the earlier pulse) and red (from the later pulse). The black sections are those which would cancel out.

With a Gaussian shaped pulse the difference is not so simple. As can be

seen in figure 5.6, the difference between the transmission of two Gaussian shaped pulses extends over a long time and the two non-cancelling regions are in contact. In this example, with a FWHM of 50 fs and a separation of 10 fs, around 80% of the probe pulse transmission will cancel out, but the remaining 20% is spread across half of the pulse.

Given that the temporal structure of the pulse would appear to be significant in how much information can be gained from the transmission measurements, it is worth examining the current state of methods and measurements of the pulse shapes generated by FELs. A number of methods have been implemented to examine the temporal structure of x-ray FEL pulses [73, 72, 92].

The methods described in refs. [73] and [72] are broadly similar in setup albeit in different regimes. In these schemes an infrared laser pulse is approximately synchronized with the FEL pulse and both beams are spatially overlapped on a Ne gas target. The photoelectrons generated by the FEL are 'dressed' by the infrared laser field. In the case of ref. [72] the duration of the x-ray pulse is less than the period of the infrared laser. This is the so-called streaked regime, where the energy shift experienced by the photoelectrons generated depends on the vector potential of the infrared laser at that time and as this varies over the duration of the FEL pulse the distribution of energies of photoelectrons will be redistributed. Depending on the exact moment of ionization compared to the IR laser the photoelectron spectrum may be upshifted or downshifted from the undressed spectrum. If the x-ray pulse is equally distributed over the zero-crossing of the vector potential of the IR laser, the centre of the spectrum will not shift but the distribution will be broadened due to the range of vector potentials experienced. The temporal structure of the x-ray pulse is therefore mapped onto

the photoelectron spectra. This method is only valid with pulses shorter than a single cycle of the infrared laser (around 8 fs) so is not applicable to the pulses that have been discussed in the work of this thesis.

The regime where the duration of the x-ray pulse is longer than the period of the infrared laser is the 'sideband regime'. Here the electron spectrum is surrounded by distinct peaks symmetrically separated from the main peak by the photon energy of the infrared laser [73]. Observation of this, in the case of photoelectrons, is complicated by the bandwidth of the FEL being large when compared to the photon energy of the infrared laser, meaning the peaks would not be observable. To counter this the electrons which are analysed are those generated through Auger decay [73]. These have an initial energy which is determined by the properties of the Ne atom rather than by the incoming FEL beam. This gives a relatively narrow peak and so the effect of the infrared laser can be observed. Due to the resolution of their experiment the authors of ref. [73] were not able to directly observe the individual sidebands, but rather observed a broadening of the Auger electron spectrum. This spectrum agreed well with simulations giving x-ray pulse durations of 40 fs and 120 fs for electron bunch lengths of 75 fs and 175 fs respectively. To augment these results they simulated the FEL using the GENESIS code [93], which gave results with similar lengths to those derived from the experiment. However the shape of the simulated x-ray pulse with the 175 fs electron bunch was more triangular than Gaussian. This shape would give the same experimental result as a Gaussian shape.

The method used by Behrens *et al.* [92] uses the electron beam to deduce the x-ray pulse structure. The FEL process leads to the electron bunch losing energy and the spread of electron energies increasing. An RF deflector downstream of the undulators is used to induce a spatial-temporal corre-

lation in the electron bunch, such that those electrons which are earlier in the bunch are spatially separate from those at the end of the bunch. The 'streaked' electron beam is passed through a vertical bend dipole magnet. The beam density distribution is then passed onto a screen monitored by a camera. The resulting image is analysed to give the electron energy distribution as a function of time, and by comparing this with the profile when the lasing is turned off the full x-ray pulse temporal structure can be derived. An example of the single-shot images is shown in figure 5.7. This pulse, which has a length of around 100 fs, is not far from a flattop pulse. The two methods of recovering the pulse shape, by the average energy loses and the energy spread, give almost the same result. The method is also applicable to much shorter pulse lengths

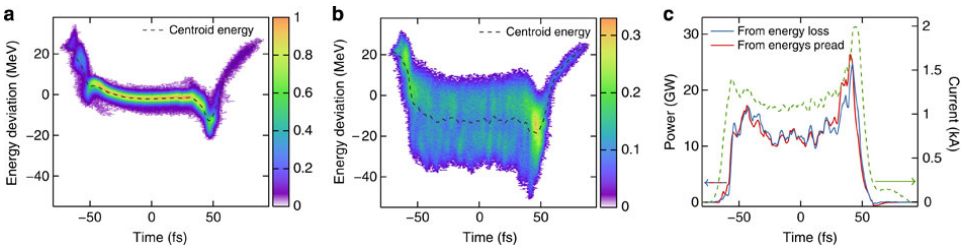

Figure 5.7: The results of phase space analysis on the electron beam with the FEL lasing turned off (**a**) and on (**b**). The position of the centroid energy and the spread of the energy provide two routes for determining the x-ray pulse structure. The reconstructed pulse shape is shown in **c** along with the electron beam current. Taken from Behrens *et al.* Nat. Comm. **5**, 3762[92]

Given the information on the pulse shape from these experiments, further simulation work could be performed to see how that will affect the results of the split and delay transmission scheme.

The work in the previous chapter showed that the increase of transmission is a fluence effect. This combined with the transmission of a probe pulse, temporally separated from the pump pulse, would allow for the time

evolution to be derived due to the spatial distribution of intensities, i.e. the transmission at the location which experiences 20% of the intensity corresponds to the transmission of the region that experiences the peak intensity 20% into the pulse. This method would not require detailed knowledge of the temporal structure, but does make an assumption on the evolution of the system.

CHAPTER 6

Conclusions and future work

Throughout this thesis the materials under investigation have been the exotic form of solid-density aluminium plasma generated by an x-ray FEL. These new light-sources with exceedingly high spectral brightness have allowed for the generation of very well characterised plasmas. Since the absorption of photons at x-ray wavelengths is dominated by atomic transitions and the duration of the interaction is less than the timescale of atomic motion, the modelling of these systems is both relatively simple and informative.

In chapter 3 the role of opacity in how the emergent radiation from the sample was altered was examined. Through this it was found that the width of the first Kα peak, when the FEL photon energy was tuned to above the K-edge energy, did not vary much with intensity in both experiment

and simulation. However, when the FEL was tuned to below the K-edge energy the width of the first Kα peak was found to have a dependence on the intensity of the FEL. The broadening of the peak was due to opacity broadening.

Further simulation work on the below K-edge pumping showed that the key quantity in determining the emission spectrum and the opacity broadening was the intensity rather than the fluence. Since the emission spectra, in this case, are reliant on a resonant process, that is only available for a short period within the FEL pulse, the number of photons that impinge on the target in that time is an important quantity. Hence intensity is the primary determining factor. Additional simulation work showed how the geometry of how the sample is observed will change the recorded spectra due to the regions which the emission will pass through, and thus be attenuated by, varying with viewing angle.

Chapter 4 was based on another experiment at LCLS, in which the transmission of the FEL used to generate the plasma was analysed. The resulting photon energy transmission curve was found to differ significantly from the transmission for cold aluminium. However the resulting curve did agree well with the simulation work.

Through the simulation work it was possible to find the mechanism through which the saturable absorption occurs. The sample will become largely transparent to the FEL radiation when it has been ionized to such an extent that the remaining ions have a K-edge energy greater than the photon energy of the FEL. The mechanisms by which the ionization occurs were further examined and it was found that the collisional ionization rate was the dominant means by which the sample was ionized.

The rapid change of ionization state has implications for the MAD

method of structure determination. As heavy ions are ionized the anomalous scattering factor will change, altering the MAD signal. To accurately use the MAD method this change in anomalous scattering must be known. In this manner being able to match simulations to experimental measurements of the transmission is useful. In a protein, where these methods would be useful, the number density of the heavy elements will be much less than in a solid of that element. A possible future direction to investigate would be to look at how much the plasma conditions would affect the MAD signal. In a protein many of the atoms are light elements such as hydrogen, carbon, oxygen, and nitrogen. These elements have a much lower chance of absorbing x-rays than heavy ions like iron, which are used in MAD measurements. Previous work with simulating iron in high intensity FEL fields have only considered isolated ions whereas the work described in section 4.8 considered aluminium ions in a dense plasma of aluminium ions. The real situation is likely somewhere between the two situations, although the exact results are something that will require further investigation.

In chapter 5 simulations of an x-ray pump x-ray probe system were presented. These showed how the transmission of the sample seen by probe pulses delayed by 10–100 fs changed as a function of delay.

By taking the difference between two successive probe pulses the regions which have the biggest change between the start and the end of the pulse are revealed. Regions which show less change have three possible causes. Firstly in high intensity regimes saturation of the absorption will occur early in the pulse, so probes which are reasonably delayed from the pump pulse will not see much change in transmission over their duration. Secondly in the positions that experience very little FEL intensity the FEL is not strong enough to induce the saturable absorption process and so there isn't any

change over the duration of the probe pulse. The final cause for a lesser change in transmission has its roots in the way IPD is dealt with in the code. Over the duration of the pulse it is possible for an ion that previously was not possible to photoionize from the K-shell to become accessible due to the increased IPD at later times. The difference between the opacity at the start of the probe pulse (when the pertinent charge state can't be photoionized) and the end of the pulse (when it can be photoionized) can be relatively small, leading to a small change in the transmission seen by two successive probe pulses.

From the work in section 5.4 it is evident that the accurate temporal profile of the x-ray beam is required to get the most information from the split and delay system. On the simulation side further work could be done in extending the work to other pulse shapes. The most likely candidates for further investigation would be Gaussian, triangular and two peaked (as in figure 5.7) pulse shapes.

Ultimately justification of the simulation work will come from experimental realization. With the increasing knowledge of the pulse shape these types of measurement will have increasing weight. Even without precious knowledge of the exact temporal pulse shape these measurements would allow for some understanding of how the transmission changes with FEL fluence.

In conclusion, the arrival of 4th generation light-sources has opened the opportunity to study novel, well characterised plasmas with exquisite temporal precision. The absorption properties of these dense plasmas are an important aspect when analysing how much energy is deposited within them. This in turn affects the response of the material to further x-rays. Throughout this thesis the way that the sample responds to this intense irradiation

and what could and is observed has been explored.

References

[1] D. Rackstraw, S. Vinko, et al. Opacity effects in a solid-density aluminium plasma created by photo-excitation with an X-ray laser. *High Energy Density Physics*, 11:59–69, June 2014.

[2] D. S. Rackstraw, O. Ciricosta, et al. Saturable Absorption of an X-Ray Free-Electron-Laser Heated Solid-Density Aluminum Plasma. *Physical Review Letters*, 114(1):015003, January 2015.

[3] C. Pellegrini. The history of X-ray free-electron lasers. *The European Physical Journal H*, 37(5):659–708, June 2012.

[4] G. Margaritondo and P. Rebernik Ribic. A simplified description of X-ray free-electron lasers. *Journal of synchrotron radiation*, 18(Pt 2): 101–8, March 2011.

[5] P. Emma, R. Akre, et al. First lasing and operation of an ångstrom-wavelength free-electron laser. *Nature Photonics*, 4(9):641–647, August 2010.

[6] A. M. Kondratenko and E. L. Saldin. Generating Of Coherent Radiation By A Relativistic Electron beam In An ondulator. *Particle Accelerators*, 10:207–216, 1980.

[7] R. Bonifacio, C. Pellegrini, et al. Collective instabilities and high-gain regime in a free electron laser. *Optics Communications*, 50(6):373–378, July 1984.

[8] J. Amann, W. Berg, et al. Demonstration of self-seeding in a hard-X-ray free-electron laser. *Nature Photonics*, 6:693–698, August 2012.

[9] W. Ackermann, G. Asova, et al. Operation of a free-electron laser from the extreme ultraviolet to the water window. *Nature Photonics*, 1(6): 336–342, June 2007.

[10] K. Tiedtke, A. Azima, et al. The soft x-ray free-electron laser FLASH at DESY: beamlines, diagnostics and end-stations. *New Journal of Physics*, 11(2):023029, February 2009.

[11] E. Allaria, C. Callegari, et al. The FERMI@Elettra free-electron-laser source for coherent x-ray physics: photon properties, beam transport system and applications. *New Journal of Physics*, 12(7):075002, July 2010.

[12] T. Ishikawa, H. Aoyagi, et al. A compact X-ray free-electron laser emitting in the sub-ångström region. *Nature Photonics*, 6(8):540–544, June 2012.

[13] European xfel website. `http://www.xfel.eu/`. Accessed: 2015-03-02.

[14] Swissfel website. `http://www.psi.ch/swissfel/`. Accessed: 2015-03-02.

[15] L. Young, E. P. Kanter, et al. Femtosecond electronic response of atoms to ultra-intense X-rays. *Nature*, 466(7302):56–61, July 2010.

[16] O. Ciricosta, H.-K. Chung, et al. Simulations of neon irradiated by intense X-ray laser radiation. *High Energy Density Physics*, 7(3):111–116, September 2011.

[17] G. Doumy, C. Roedig, et al. Nonlinear Atomic Response to Intense Ultrashort X Rays. *Physical Review Letters*, 106(8):083002, February 2011.

[18] B. Rudek, S.-K. Son, et al. Ultra-efficient ionization of heavy atoms by intense X-ray free-electron laser pulses. *Nature Photonics*, 6(12): 858–865, November 2012.

[19] M. Hoener, L. Fang, et al. Ultraintense X-Ray Induced Ionization, Dissociation, and Frustrated Absorption in Molecular Nitrogen. *Physical Review Letters*, 104(25):253002, June 2010.

[20] L. Fang, T. Osipov, et al. Multiphoton Ionization as a clock to Reveal Molecular Dynamics with Intense Short X-ray Free Electron Laser Pulses. *Physical Review Letters*, 109(26):263001, December 2012.

[21] N. Berrah, L. Fang, et al. Multiphoton ionization and fragmentation of molecules with the LCLS X-ray FEL. *Journal of Electron Spectroscopy and Related Phenomena*, 196:34–37, October 2014.

[22] S. Schorb, D. Rupp, et al. Size-Dependent Ultrafast Ionization Dynamics of Nanoscale Samples in Intense Femtosecond X-Ray Free-Electron-Laser Pulses. *Physical Review Letters*, 108(23):233401, June 2012.

[23] H. Thomas, A. Helal, et al. Explosions of Xenon Clusters in Ultraintense Femtosecond X-Ray Pulses from the LCLS Free Electron Laser. *Physical Review Letters*, 108(13):133401, March 2012.

[24] T. Gorkhover, M. Adolph, et al. Nanoplasma Dynamics of Single Large Xenon Clusters Irradiated with Superintense X-Ray Pulses from the Linac Coherent Light Source Free-Electron Laser. *Physical Review Letters*, 108(24):245005, June 2012.

[25] D. B. Guenther, P. Demarque, et al. Standard solar model. *The Astrophysical Journal*, 387:372, March 1992.

[26] J. Lindl. Development of the indirect-drive approach to inertial confinement fusion and the target physics basis for ignition and gain. *Physics of Plasmas*, 2(11):3933, November 1995.

[27] A. Saemann, K. Eidmann, et al. Isochoric Heating of Solid Aluminum by Ultrashort Laser Pulses Focused on a Tamped Target. *Physical Review Letters*, 82(24):4843–4846, June 1999.

[28] K. Eidmann, U. Andiel, et al. K-shell spectra from hot dense aluminum layers buried in carbon and heated by ultrashort laser pulses. *Journal of Quantitative Spectroscopy and Radiative Transfer*, 81(1-4):133–146, September 2003.

[29] F. Perez, L. Gremillet, et al. Enhanced Isochoric Heating from Fast Electrons Produced by High-Contrast, Relativistic-Intensity Laser Pulses. *Physical Review Letters*, 104(8):085001, February 2010.

[30] K. Eidmann, A. Saemann, et al. Generation of hot plasma at solid density by high-contrast ultra-short laser pulses. *Journal of Quantitative Spectroscopy and Radiative Transfer*, 65(1-3):173–184, April 2000.

[31] P. Audebert, R. Shepherd, et al. Heating of Thin Foils with a Relativistic-Intensity Short-Pulse Laser. *Physical Review Letters*, 89 (26):265001, December 2002.

[32] S. M. Vinko, O. Ciricosta, et al. Creation and diagnosis of a solid-density plasma with an X-ray free-electron laser. *Nature*, 482(7383): 59–62, February 2012.

[33] B. I. Cho, K. Engelhorn, et al. Resonant Kα Spectroscopy of Solid-Density Aluminum Plasmas. *Physical Review Letters*, 109(24):245003, December 2012.

[34] S. M. Vinko, O. Ciricosta, et al. Investigation of femtosecond collisional ionization rates in a solid-density aluminium plasma. *Nature Communications*, 6:6397, March 2015.

[35] O. Ciricosta, S. M. Vinko, et al. Direct Measurements of the Ionization Potential Depression in a Dense Plasma. *Physical Review Letters*, 109 (6):065002, August 2012.

[36] G. Ecker and W. Kröll. Lowering of the Ionization Energy for a Plasma in Thermodynamic Equilibrium. *Physics of Fluids*, 6(1):62, January 1963.

[37] J. C. Stewart and K. D. Pyatt. Lowering of Ionization Potentials in Plasmas. *The Astrophysical Journal*, 144:1203, June 1966.

[38] H. N. Chapman, P. Fromme, et al. Femtosecond X-ray protein nanocrystallography. *Nature*, 470(7332):73–7, February 2011.

[39] M. M. Seibert, T. Ekeberg, et al. Single mimivirus particles intercepted and imaged with an X-ray laser. *Nature*, 470(7332):78–81, February 2011.

[40] S. Boutet, L. Lomb, et al. High-Resolution Protein Structure Determination by Serial Femtosecond Crystallography. *Science*, 337(6092): 362–364, May 2012.

[41] L. C. Johansson, D. Arnlund, et al. Lipidic phase membrane protein serial femtosecond crystallography. *Nature methods*, 9(3):263–265, March 2012.

[42] J. Tenboer, S. Basu, et al. Time-resolved serial crystallography captures high-resolution intermediates of photoactive yellow protein. *Science*, 346(6214):1242–1246, December 2014.

[43] A. Barty, C. Caleman, et al. Self-terminating diffraction gates femtosecond X-ray nanocrystallography measurements. *Nature Photonics*, 6(1):35–40, December 2011.

[44] M. R. Sawaya, D. Cascio, et al. Protein crystal structure obtained at 2.9 Åresolution from injecting bacterial cells into an X-ray free-electron laser beam. *Proceedings of the National Academy of Sciences of the United States of America*, 111(35):12769–74, September 2014.

[45] J. Kern, R. Alonso-Mori, et al. Simultaneous Femtosecond X-ray Spectroscopy and Diffraction of Photosystem II at Room Temperature. *Science (New York, N.Y.)*, 340(6131):491–495, February 2013.

[46] J. Kern, R. Tran, et al. Taking snapshots of photosynthetic water oxidation using femtosecond X-ray diffraction and spectroscopy. *Nature communications*, 5:4371, January 2014.

[47] H. Ostrom, H. Oberg, et al. Probing the transition state region in catalytic CO oxidation on Ru. *Science*, 347(6225):978–982, February 2015.

[48] A. Bar-Shalom, J. Oreg, et al. Super-transition-arrays: A model for the spectral analysis of hot, dense plasma. *Physical Review A*, 40(6): 3183–3193, September 1989.

[49] H.-K. Chung, M. H. Chen, et al. FLYCHK: Generalized population kinetics and spectral model for rapid spectroscopic analysis for all elements. *High Energy Density Physics*, 1(1):3–12, December 2005.

[50] CXRO. `http://www.cxro.lbl.gov`. Accessed: 2014-03-17.

[51] I. Hubený and D. Mihalas. *Theory of stellar atmospheres : an introduction to astrophysical non-equilibrium quantitative spectroscopic analysis*. Princeton series in astrophysics Y. Princeton, New Jersey : Princeton University Press, 2014.

[52] O. Ciricosta. *Plasma Evolution and Continuum Lowering in Hot Dense Matter generated by X-ray Free Electron Lasers*. PhD thesis, University of Oxford, 2014.

[53] A. G. de la Varga, P. Velarde, et al. Non-Maxwellian electron distributions in time-dependent simulations of low-Z materials illuminated by a high-intensity X-ray laser. *High Energy Density Physics*, 9(3):542–547, September 2013.

[54] A. de la Varga, P. Velarde, et al. Radiative properties for warm and hot dense matter. *High Energy Density Physics*, 7(3):163–168, September 2011.

[55] S. Nayakshin and F. Melia. Self-consistent Fokker-Planck Treatment of Particle Distributions in Astrophysical Plasmas. *The Astrophysical Journal Supplement Series*, 114(2):269–288, February 1998.

[56] A. de la Varga and P. Velarde. Private communication.

[57] A. Burgess and M. C. Chidichimo. Electron impact ionization of complex ions. *Monthly Notices of the Royal Astronomical Society (ISSN 0035-8711)*, 203:1269–1280, 1983.

[58] S. M. Vinko, O. Ciricosta, et al. Density functional theory calculations of continuum lowering in strongly coupled plasmas. *Nature Communications*, 5:3533, March 2014.

[59] J. Apruzese. Direct solution of the equation of transfer using frequency- and angle-averaged photon-escape probabilities for spherical and cylindrical geometries. *Journal of Quantitative Spectroscopy and Radiative Transfer*, 25(5):419–425, May 1981.

[60] J. Apruzese. An analytic Voigt profile escape probability approximation. *Journal of Quantitative Spectroscopy and Radiative Transfer*, 34 (5):447–452, November 1985.

[61] J. Chalupský, J. Krzywinski, et al. Spot size characterization of focused non-Gaussian X-ray laser beams. *Optics Express*, 18(26):27836, December 2010.

[62] J. Chalupsky, P. Bohacek, et al. Comparing different approaches to characterization of focused X-ray laser beams. *Nuclear Instruments and Methods in Physics Research Section A: Accelerators, Spectrometers, Detectors and Associated Equipment*, 631(1):130–133, March 2011.

[63] J. Chalupský, T. Burian, et al. Fluence scan: an unexplored property of a laser beam. *Optics express*, 21(22):26363–75, November 2013.

[64] M. O. Krause. Atomic radiative and radiationless yields for K and L shells. *Journal of Physical and Chemical Reference Data*, 8(2):307, April 1979.

[65] H.-K. Chung, M. H. Chen, et al. Extension of atomic configuration sets of the Non-LTE model in the application to the Kα diagnostics of hot dense matter. *High Energy Density Physics*, 3(1-2):57–64, May 2007.

[66] T. Holstein. Imprisonment of Resonance Radiation. *Physical Review*, 72(12):1212–1233, December 1947.

[67] G. J. Phillips, J. S. Wark, et al. Escape factors in zero-dimensional radiation-transfer codes. *High Energy Density Physics*, 4(1-2):18–25, April 2008.

[68] B. Yaakobi, D. Steel, et al. Explosive-pusher-type laser compression experiments with neon-filled microballoons. *Physical Review A*, 19(3): 1247–1262, March 1979.

[69] J. Kilkenny, R. Lee, et al. X-ray spectroscopic diagnosis of laser-produced plasmas, with emphasis on line broadening. *Physical Review A*, 22(6):2746–2760, December 1980.

[70] N. Delamater, C. Hooper, et al. Opacity effects on hydrogenlike x-ray lines emitted from laser-driven implosions. *Physical Review A*, 31(4): 2460–2463, April 1985.

[71] S. Sorge, A. Wierling, et al. Diagnostics of a laser-induced dense plasma by hydrogen-like carbon spectra. *Journal of Physics B: Atomic, Molecular and Optical Physics*, 33(16):2983, August 2000.

[72] W. Helml, A. R. Maier, et al. Measuring the temporal structure of few-femtosecond free-electron laser X-ray pulses directly in the time domain. *Nature Photonics*, 8(12):950–957, November 2014.

[73] S. Düsterer, P. Radcliffe, et al. Femtosecond x-ray pulse length characterization at the Linac Coherent Light Source free-electron laser. *New Journal of Physics*, 13(9):093024, September 2011.

[74] Y. Ding, F.-J. Decker, et al. Femtosecond X-Ray Pulse Characterization in Free-Electron Lasers Using a Cross-Correlation Technique. *Physical Review Letters*, 109(25):254802, December 2012.

[75] N. Rohringer and R. Santra. X-ray nonlinear optical processes using a self-amplified spontaneous emission free-electron laser. *Physical Review A*, 76(3):033416, September 2007.

[76] K. Tiedtke, A. A. Sorokin, et al. Absolute pulse energy measurements of soft x-rays at the Linac Coherent Light Source. *Optics Express*, 22 (18):21214, August 2014.

[77] J. Barkyoumb and D. Smith. X-ray scattering factors of metallic aluminum calculated from a self-consistent x-ray attenuation data base. *Physical Review A*, 41(9):4863–4867, May 1990.

[78] D. Ratner, A. Brachmann, et al. Second and third harmonic measurements at the linac coherent light source. *Physical Review Special Topics - Accelerators and Beams*, 14(6):060701, June 2011.

[79] B. Nagler, U. Zastrau, et al. Turning solid aluminium transparent by intense soft X-ray photoionization. *Nature Physics*, 5(9):693–696, July 2009.

[80] C.-O. Almbladh, A. Morales, et al. Theory of Auger core-valence-valence processes in simple metals. I. Total yields and core-level lifetime widths. *Physical Review B*, 39(6):3489–3502, February 1989.

[81] H. Yoneda, Y. Inubushi, et al. Saturable absorption of intense hard X-rays in iron. *Nature Communications*, 5:5080, October 2014.

[82] E. McGuire. K-Shell Auger Transition Rates and Fluorescence Yields for Elements Ar-Xe. *Physical Review A*, 2(2):273–278, August 1970.

[83] http://aphysics2.lanl.gov/tempweb/lanl/. Accessed: 2015-05-15.

[84] E. McGuire. Atomic L-Shell Coster-Kronig, Auger, and Radiative Rates and Flourescence Yields for Na-Th. *Physical Review A*, 3(2):587–594, February 1971.

[85] B. Henke, E. Gullikson, et al. X-Ray Interactions: Photoabsorption, Scattering, Transmission, and Reflection at E = 50-30,000 eV, Z = 1-92. *Atomic Data and Nuclear Data Tables*, 54(2):181–342, July 1993.

[86] H. M. Krishna Murthy. Use of multiple-wavelength anomalous diffraction measurements in ab initio phase determination for macromolecular structures. *Methods in molecular biology (Clifton, N.J.)*, 56:127–51, January 1996.

[87] J. Guss, E. Merritt, et al. Phase determination by multiple-wavelength x-ray diffraction: crystal structure of a basic "blue" copper protein from cucumbers. *Science*, 241(4867):806–811, August 1988.

[88] W. A. Hendrickson. Determination of Macromolecular Structures from Anomalous Diffraction of Synchrotron Radiation on JSTOR. *Science*, 254(5028):51–58, October 1991.

[89] S.-K. Son, H. N. Chapman, et al. Multiwavelength Anomalous Diffraction at High X-Ray Intensity. *Physical Review Letters*, 107(21):218102, November 2011.

[90] S.-K. Son, H. N. Chapman, et al. Determination of multiwavelength anomalous diffraction coefficients at high x-ray intensity. *Journal of Physics B: Atomic, Molecular and Optical Physics*, 46(16):164015, August 2013.

[91] C. David, P. Karvinen, et al. Following the dynamics of matter with femtosecond precision using the X-ray streaking method. *Scientific reports*, 5:7644, January 2015.

[92] C. Behrens, F.-J. Decker, et al. Few-femtosecond time-resolved measurements of X-ray free-electron lasers. *Nature Communications*, 5: 3762, April 2014.

[93] S. Reiche. GENESIS 1.3: a fully 3D time-dependent FEL simulation code. *Nuclear Instruments and Methods in Physics Research Section A: Accelerators, Spectrometers, Detectors and Associated Equipment*, 429 (1-3):243–248, June 1999.

List of Acronyms

CXRO	Center for X-Ray Optics
EXAFS	X-ray Absorption Fine Structure
FEL	Free-Electron-Laser
FLASH	Free-electron-LASer in Hamburg
GMD	Gas Monitor Detector
IPD	Ionization Potential Depression
LCLS	Linac Coherent LightSource
LTE	Local Thermodynamic Equilibrium
MAD	Multiwavelength Anomalous Diffraction
SASE	Self-Amplified Spontaneous Emission
XUV	Extreme UltraViolet

List of Figures